

# Anatomy of a fumarole field; drone remote sensing and petrological approaches reveal the degassing and alteration structure at La Fossa cone, Vulcano Island, Italy

Daniel Müller<sup>1</sup>, Thomas R. Walter<sup>1</sup>, Valentin R. Troll<sup>2,3</sup>, Jessica Stammeier<sup>1</sup>, Andreas ~~Karlsson~~<sup>3</sup>Karlsson<sup>4</sup>, Erica de ~~Paolo~~<sup>4</sup>Paolo<sup>5</sup>, Antonino Fabio ~~Pisciotta~~<sup>5</sup>Pisciotta<sup>6</sup>, Martin Zimmer<sup>1</sup>, Benjamin De Jarnatt<sup>1</sup>

<sup>1</sup> GFZ German Research Centre for Geosciences, Telegrafenberg, 14473 Potsdam, Germany

<sup>2</sup> Dept. of Earth Sciences, Natural Resources and Sustainable Development, Uppsala University, Sweden

<sup>3,3</sup> Istituto Nazionale di Geofisica e Vulcanologia (INGV), Rome, Italy

<sup>4</sup> Department of Geosciences, Swedish Museum of Natural History, Box 50007, SE-104 05 Stockholm, Sweden

<sup>4,5</sup> University of Milano-Bicocca, Department of Earth and Environmental Sciences, Piazza della Scienza 4 – 20126 Milano, Italy

<sup>5,6</sup> Istituto Nazionale di Geofisica e Vulcanologia (INGV), Palermo, Italy

*Correspondence to:* Daniel Müller (dmueller@gfz-potsdam.de)



161 [detailed characterisation of alteration and activity patterns of volcanic degassing sites and has potential for application in](#)  
162 [alteration research and for monitoring of volcanic degassing systems.](#)

## 164 1 Introduction

### 165 1.1 Volcanic degassing and hydrothermal alteration

166 Volcanic degassing at the Earth's surface is typically expressed in the form of localized fumarole fields and diffuse ~~gas escape,~~  
167 ~~yet degassing.~~ [Yet](#), the association of localized and diffuse degassing is not well constrained. A fumarole is a vent or opening  
168 in the Earth's surface that releases steam and gas, including sulfur dioxide, carbon dioxide, and hydrogen sulfide, into the  
169 atmosphere (e.g. Giggenbach, 1996; Giammanco et al., 1998; Halldorsson et al., 2013). Fumaroles are typically found near  
170 volcanic areas or geothermal regions where there is intense heat beneath the surface. Fumaroles are of interest to scientists  
171 studying volcanoes and geothermal systems, as they provide information on the composition of underlying magmatic systems,  
172 the degassing processes of such magmatic systems, and the dynamic changes in the degassing passways exploited by such  
173 systems (e.g. Chiodini et al., 1993; Aiuppa et al., 2005; Paonita et al., 2013). The gas emissions by fumaroles, moreover,  
174 provide information on the possible interaction between underground water and hot rocks or magma and thus the state of a  
175 hydrothermal system through time (e.g. Chiodini et al., 1993; Capasso et al., 2000; Nuccio et al., 2001; Troll et al., 2012;  
176 Paonita et al., 2013).

177 The degassing of hot and acid volcanic gasses leads to versatile fluid-rock interactions at the surrounding volcanic rock,  
178 summarized as hydrothermal alteration (Pirajno, 2009; Chiodini et al., 2013; Fulignati, 2020). Alteration can affect the  
179 mineral assemblage by dissolution and remineralization up to complete destruction of the original mineral matrix and  
180 eventually influence essential rock parameters with potentially far-reaching consequences for the shallow hydrothermal system  
181 and the stability of a volcanic building (Reid & Brien, 2001; Heap & Violay, 2021). Mechanical strength tests of  
182 hydrothermally altered rocks showed considerable mechanical weakening (e.g. [Frolova et al., 2014](#); [Heap et al., 2019](#), [Julia et](#)  
183 [al., 2014](#), [2021a](#), [Darmawan et al., 2022](#)), which is usually accomplished by mineral dissolution and mineral re-precipitation  
184 that affect rock strength and permeability and can in cases even seal gas pathways. Hydrothermal alteration can thus lead to  
185 sealed rock masses and hence to pressure build-up in a shallow volcanic system and consequently influence volcanic activity  
186 (e.g. [Heap et al., 2019](#)) [and increase the likelihood of flank deformation and collapse \(Heap et al., 2021b\)](#). It is therefore  
187 important to better understand the degassing and alteration structures in active hydrothermal crater regions of hazardous  
188 volcanic systems.

189 In this study of the fumaroles of La Fossa Vulcano Island - Italy, we aim to detect and quantify alteration-related spatial and  
190 compositional parameters in order to provide improved insight into the dynamic changes of hydrothermal venting systems to  
191 help identify temporal and potentially critical developments and to better understand the associated features of diffuse and  
192 localized degassing.

225

## 226 1.2 Structure and extent of degassing sites

227 Recent advances in volcanic geothermal areas suggest that fumaroles are often only localized expressions of a much larger  
228 area of degassing (e.g. Toutain et al., 2009; Liuzzo et al., 2015). Indeed, fumaroles and hydrothermal degassing zones are  
229 often accompanied by broader fields of activity, characterized by diffuse degassing processes, associated mineral changes, and  
230 intense surface recoloration (e.g. Donoghue et al., 2008; Berg et al., 2018; Darmawan et al., 2022) and fumaroles activity can  
231 vary in time (Troll et al., 2012; Fischer et al., 2015) and in size (Lynch et al., 2013; Gertisser et al 2023). Previous works at  
232 Vulcano, for instance, have shown that fumaroles are surrounded by extensive areas of diffuse degassing (Carapezza et al.,  
233 2011; Chiodini et al., 2005; Manini et al., 2019). Our previous work showed that diffuse degassing leads to distinct zones  
234 ~~classified~~of activity that can be identified by temperatures and visual expression (Müller et al., 2021). Those diffuse zones are  
235 ~~at~~typically constrained based on CO<sub>2</sub> measurements but are also subject to the diffuse flow of acid gas driving diffuse  
236 alteration processes. However, these diffuse degassing and alteration processes are often difficult to recognize without  
237 specialized sampling strategies (Toutain et al., 2009), leading to a limited understanding of the anatomy and extent of degassing  
238 and alteration systems. Understanding the dynamic changes and internal architecture of hydrothermal activity of fumarole  
239 fields and the true dimensions of their field of activity is of relevance for the study of volcanic hazard~~activity~~ and  
240 ~~resource~~hazard potential.

241

## 242 1.3 Surface effects and remote sensing of alteration

243 Hydrothermal alteration can cause significant changes in the physical and chemical properties of volcanic rock, such as density,  
244 compressive strength, and permeability (e.g. Donoghue et al., 2008, 2010; Berg et al., 2018; Heap et al., 2019; Darmawan et  
245 al., 2022). The replacement of primary minerals by secondary minerals, element mobility of fluid-mobile components,  
246 enrichment of refractory elements, and physical and textural changes of rock properties are often accompanied by changes in  
247 the color or spectral reflectance characteristics and can be traced employing remote sensing techniques.

248 Several studies have investigated the relationship between coloration and hydrothermal alteration. The use of rock color or  
249 spectral reflectance particularities as an indicator of alteration has been explored since the 1970s and led to the development  
250 of a variety of remote sensing techniques using satellite imagery from ETRS multispectral imagery (Rowan et. al., 1976),  
251 Landsat Thematic mapper mission (Carranza et al., 2002), ETM+ (Mia et al., 2012) or ASTER data (Di Tommaso et al., 2007)  
252 or hyperspectral analysis (e.g. Van De Meer et al., 2012; Tayebi et al., 2015). These techniques can detect subtle changes in  
253 color that may not be visible to the naked eye, allowing for the identification of mineral deposits (Mielke et al., 2016),  
254 hydrothermal alteration, or volcano stability (Kereszturi et al., 2020).

255 However, for analyzing ~~details~~ of localized degassing and alteration systems, the resolution of satellite data often is a limiting  
256 factor. Some of the best available optical satellite data have a resolution of 0.5 m in the nadir acquisition position. The

For  
For  
For  
bor  
bor  
For

287 resolution of thermal satellite data is on the order of tens to hundreds of meters per pixel. That allows the general detection of  
288 degassing and alteration systems, but the imaging of details of such systems requires the use of very high-resolution data.  
289 Modern UAS (unmanned aerial systems) equipped with high-resolution sensors allow imaging of volcanic surfaces at cm  
290 scales and, therefore, permit the analysis of degassing and alteration systems in great detail. In combination with Structure  
291 from Motion (SfM) processing, they are efficient for first-site investigations and allow the creation of high-resolution structural  
292 maps to identify structures of degassing systems to assist first-order hazard analysis or guide further in-depth studies.

#### 293 **1.4 Aim of the study**

294 The aim of this work is to image and analyze the degassing and alteration structure of the La Fossa fumarole field and the  
295 wider field of activity and better understand the association of diffuse and localized degassing at a fumarole field and alteration  
296 at degassing sites. We advance previous results (Müller et al., 2021) by considering new data, and by integrating them with  
297 the mineralogical and chemical analysis of alteration distribution in collected rock samples. We show systematic changes in  
298 the effects of alteration on the surface coloration and how drone-derived RGB data (Red, Green, Blue, standard color coding  
299 of images) can be used for the efficient detection and classification of degassing and alteration features. Combining UAS-  
300 based optical and infrared remote sensing with mineralogical- and geochemical analysis, and diffuse surface degassing  
301 measurements, we can infer the detailed anatomy of degassing and alteration systems at the surface, highlight active degassing  
302 domains versus areas of surface sealing, and determine their importance for the system based on their contribution to the total  
303 thermal energy release.

#### 304 **2 Study area**

305 Vulcano is the southernmost of a group of 7 small volcanic islands forming the Aeolian Archipelago north of Sicily. They are  
306 located within the Aeolian Tindari Letojanni Fault System (ATLFS), an NNW-SSE striking local deformation belt connecting  
307 the central Aeolian Islands with the eastern section of Sicily (Barreca et al., 2014; Cultrera et al., 2017). The ATLFS is the  
308 interface between two larger tectonically active compartments, an extensive one in the northeast and a contractional one in the  
309 west (Cultrea et al., 2017). Frequent seismic activity and right lateral extensional displacements indicate ongoing tectonic  
310 activity (Billi et al., 2006) and the active shaping of the islands.

311 Vulcano is made up of volcanic edifices of which the northern section of the islands is the most recently active. The oldest  
312 volcanic activity at Vulcano is reported for 130 ka (De Astis et al., 2013). Six main stages of volcanic activity have been  
313 identified (De Astis et al. 1997), of which the geologically younger active parts, the La Fossa Cone and Vulcanello, have been  
314 active during historical times <8 ka, showing mainly vulcanian and strombolian activity (De Astis et al., 2013). The last  
315 eruptive period of the La Fossa Cone from 1888-1890 was characterized by strong phreatic eruptions and witnessed and  
316 documented by Giuseppe Mercalli who later coined the term Vulcanian eruptions (Clarke et al., 2015).

351 Vulcano since then ~~is~~has been in a quiescent period and volcanic activity mainly ~~expresses~~expressed in degassing. Gases are  
352 provided from a magmatic-hydrothermal system fed by a shallow magmatic reservoir beneath La Fossa volcano. The  
353 hydrothermal system is likely to have been partitioned into a hypersaline brine and a vapor phase (Henley and McNabb, 1978).  
354 The denser brine phase is confined at depth and contributes to the formation of metasomatic facies observed in deep-seated  
355 xenoliths (Adrian et al., 2007). The vapor phase, enriched with SO<sub>2</sub>, H<sub>2</sub>S, HCl, and HF, ascends to the surface and partly  
356 emerges directly from the high-temperature fumarolic field (Bolognesi and D'Amore, 1993; Chiodini et al., 2000; Capasso et  
357 al., 1997).

358 Volcanic degassing is present throughout the entire central and northern part of the island concentrating in degassing clusters  
359 at Baja Di Levante, within Vulcano Porto, and in clusters along the base and summit of La Fossa Cone (Chiodini et al., 1996;  
360 Carapezza et al., 2011; Diliberto et al., 2021; Inguaggiato et al., 2022 and many others) where frequently higher fluxes of  
361 CO<sub>2</sub> are observed. The most prominent degassing sites are the high-temperature fumaroles at the summit of Vulcano that occur  
362 in several clusters on the outer rims of La Fossa cone and are most prominent in the high-temperature fumarole field (Figure  
363 1). Degassing at the summit of La Fossa is persistent but subject to fluctuations. Gases of the high-temperature fumaroles  
364 (HTF) emerge with temperatures > 300-°C, but temperatures have been exceeded ~~in the past~~during previous volcanic crises  
365 (Harris et al., 2012; Diliberto, 2017). Temperatures of ~~>500 up to 690~~°C were reported (Harris et al., 2012, Diliberto, 2017)  
366 during previous volcanic crises ~~in May 1993 by Chiodini et al. (1995)~~.

367 ~~Several periods~~Periods of unrest ~~have been reported and~~ were accompanied by increasing fumarole temperatures (Harris et al.,  
368 2012; Diliberto, 2013; Madonia et al., 2013; Diliberto, 2017), increasing soil and groundwater temperatures (Capasso et al.,  
369 2014), changing gas compositions (Paonita et al., 2013), changes in gas flux (Inguaggiato et al., 2022), or a spatial growth of  
370 the fumarole field (Bukomirovic et al., 1997). The most recent crisis occurred in 2021 and led to increased thermal radiation  
371 (Coppola et al., 2022), deformation (INGV Bulletin reports), and localized structural changes like the formation of new major  
372 fumarole complexes. The rapid dynamics during volcanic crises and potentially negative effects of alteration on permeabilities,  
373 and therewith the potential to drain gases from the surface, highlight the importance of a better understanding of the structure  
374 and state of degassing systems.

375 Early studies about the structural setup of the Grand Cratere fumarole field of the La Fossa Cone were provided by  
376 Bukomirovic et al. (1997) and later modified (Madonia et al., 2016; Harris et al., 2009). Fulignati et al. (1999) analyzed  
377 alteration facies at Vulcano and constrained the central crater region to be a large silicic alteration complex characterized by  
378 the presence of chalcedony and amorphous silica. Outwardly to the central silicic alteration zone, advanced argillic (alunite ±  
379 gypsum) alteration develops, probably originating from the progressive neutralization of the acid fluids by weathering and  
380 dilution by meteoric waters (Fulignati et al., 1998). Müller et al. (2021) previously showed that degassing and alteration can  
381 be traced from remote sensing data far beyond the extent of the high-temperature fumarole locations. Based on surface color  
382 variability due to degassing and alteration processes they showed evidence for a more complex setup with alteration gradients  
383 within the silicic alteration complex and important structural units that will be complemented here. Examples ~~for~~of degassing  
384 and alteration-related surface color variability are shown in Figure 2.

417 To analyze the degassing and alteration structure at Vulcano, we used a combination of UAS-derived remote sensing data  
418 (optical and thermal infrared imagery), image analysis, and field-based ground-truthing by mineralogical and geochemical  
419 analysis of rock samples and surface degassing measurements. A simplified sketch of the workflow is shown in Figure 3.

420 1) An anomaly detection (~~chapter~~Chapter 3.2) based on UAS-derived data, employing image analysis techniques like Principal  
421 Component Analysis (PCA), and spectral and thermal classification (similar to Müller et al., 2021) provides the detailed optical  
422 and thermal anomaly pattern. Anomalies can be revealed based on slight color changes in the volcanic surface that occur due  
423 to degassing and hydrothermal alteration processes, or increased surface temperatures.

424 2) To verify observed anomalies, we carried out ground-truthing by mineralogical (XRD, - X-Ray ~~Diffraction~~diffraction) and  
425 geochemical (XRF - X-Ray ~~Fluorescence~~fluorescence) lab analyses of representative rock samples. Further, we performed  
426 surface degassing measurements to image the present-day degassing pattern and compared it to the observed anomaly pattern.  
427 Combining this information we can infer a detailed anatomy of the degassing and alteration structure at the surface and define  
428 and parameterize major structural units.

429 3) A temporal ~~Infrared~~-infrared monitoring carried out from 2018 to 2022, covering the volcanic crisis 2021 at Vulcano allows  
430 us to monitor the thermal evolution and response of the identified units to an event of increased gas flow with further  
431 implications of critical processes like localized surface sealing.

432 Details on the single analysis steps are provided below.

### 433 **3.1. Acquisition and processing of UAS-based optical and thermal infrared data**

435 The data acquisition was performed using a DJI Phantom 4 Pro quadcopter, equipped with a gimbal-stabilized 20 MP camera  
436 with a real shutter system, recording up to 0.5 HZ. Optical overflights were performed in the daytime at an altitude of 150 m  
437 above the fumarole field, ensuring a minimum overlap of 90 % for later photogrammetric processing. Thermal infrared image  
438 data was acquired by a Flir Tau 2 radiometric thermal infrared camera system attached to the DJI Phantom 4 Pro. The FLIR  
439 Tau 2 measures in the spectral range of thermal infrared between 7.5 and 13  $\mu\text{m}$ , has a resolution of 640 x 512 pixels, and is a  
440 fully radiometric sensor system. The infrared image data is recorded at 8 Hz by a Teax Thermal Capture 2 data logger. The  
441 camera was attached to the copter with a standard camera bracket on a self-made carrier frame and is powered by an external  
442 11.1 V lithium-polymer battery, supplying voltage to the camera system (transformed down to 5.2 V in) and to an external  
443 GPS antenna (>8V 8 V required) which provides coordinates for each infrared image. Infrared overflights were performed in  
444 the early morning hours, before the sun illuminates the crater area, to avoid disturbances of irregular surface heating due to  
445 solar radiation exposure (Stevenson and Varley, 2008). In this way, we ensure to map the thermal signal from the hydrothermal  
446 system exclusively.

478 All image data were processed using the Structure from Motion (SfM) approach in Agisoft Photoscan (Version 1.5.2.7838).  
479 The image data were inspected and images were preselected ensuring an overlap of 90%. Images of poor quality or out of  
480 focus were excluded and only images of a constant flight altitude were used for the processing. This is particularly important  
481 for the processing of infrared data, as varying altitudes might alter the radiation information due to changing pixel size to vent  
482 ratios. The infrared data was pre-inspected in Thermoviewer 3.0 and exported in a 16-bit tiff format in grayscale. We followed  
483 the typical workflow of sparse point cloud-, dense point cloud- and mesh generation, aiming to obtain a 3-dimensional model  
484 and eventually orthomosaic, digital elevation model (DEM), and infrared mosaic. The original images and processing results  
485 are roughly georeferenced, but their geolocation was optimized by manual co-registration using the ArcGIS georeferencing  
486 toolbox. An overview of the acquired and processed data sets can be found in Table 1. ▲

### 488 **3.2 Anomaly detection - Principal Component Analysis (PCA) and spectral classification for alteration mapping**

489 The alteration mapping was performed on an orthomosaic data set acquired in 2019 that, due to poor fumarole activity,  
490 provides an almost distortion-free image of the central crater region. Using an approach similar to Müller et al., (2021), the  
491 alteration structure was revealed-, similar to Müller et al. (2021), by applying a Principal Component Analysis and image  
492 classification allowing further constraints on the zonation of the fumarole area and expanding the interpretation by geochemical  
493 and mineralogical analyses of rock samples for ground truthing. PCA is a statistical tool that was invented by Pearson (1901),  
494 further developed and widely applied in remote sensing or image analysis (e.g. Loughlin, 1991; Fauvel et al., 2009; Alexandris  
495 et al., 2017). It can detect and highlight optical anomalies within an RGB data set by transforming the data values of the initial  
496 RGB channels onto their perpendicular axes of the highest data variance. The resulting Principal Components are variance  
497 representations (e.g. Abdi & Williams, 2010). This can be achieved in several ways. We used the PCA implemented in the  
498 ArcGIS image analysis toolbox (see ArcGIS online documentation for Principal Component Analysis), performing the  
499 following workflow. In the first step, an ellipse including all data points is calculated for each dimension (RGB). The main  
500 axes of these ellipses represent the Eigenvectors (direction of highest variance), and will be used as a new coordinate system  
501 for the data transformation. By transforming all data points onto this new coordinate system, we obtain Principal Components  
502 (PC) which are variance representations of the initial RGB image data and can be used to detect and highlight optical anomalies  
503 like color changes due to alteration processes- (Müller et al., 2021, Darmawan et al., 2022). PCA further promotes a  
504 decorrelation of the initial RGB bands, a dimensionality reduction, and associated better data separability so that color  
505 variations, before expressed by changes in the three RGB bands (3-dimensional problem), can now be accessed in single bands,  
506 the single Principal Components (PC). While Principal Component 1 (PC) resembles ~91.3 % (95) of the initial data variance,  
507 it mainly shows brightness changes within the image. PC 2 and 3 contain 7.4 (4.5) and 2.3 (0.5) % of the data variance,  
508 resemble color changes, and are suitable to resolve optical anomalies related to hydrothermal alteration. ▲

540 ~~Hydrothermally~~In our data, ~~hydrothermally~~ altered areas were defined based on the PC3, with pixel values > 85 representing  
541 hydrothermal alteration. We used this as a mask to crop the respective pixel locations ~~in~~from the original orthomosaic, ~~(RGB)~~,  
542 resulting in a 16 Mio pixel alteration raster subset, ~~(RGB)~~. This ~~alteration~~ raster subset allows for a more sensitive image  
543 analysis due to the reduced spectral range with respect to the original orthomosaic. ~~An~~Another iteration of PCA, now applied  
544 to the extracted alteration raster subset adjusts to the new reduced spectral range, as we are excluding all redundant data e.g.  
545 unaltered surface, and provide a variance representation of the altered surface exclusively. We classified the result in an  
546 unsupervised classification (implemented in ArcGIS, using a combination of Iso Cluster and Maximum Likelihood  
547 classification) with 32 classes ~~was applied to the PCA of the hydrothermal alteration raster subset and used to classify optical~~  
548 ~~units~~. We decided on unsupervised classification as this is a more data-explorative way of exploring the pixel information,  
549 rather than classifying based on a spectral range constrained by training areas defined on pre-assumptions in a supervised  
550 classification. The 32 classes are chosen to obtain a high class resolution, as this is the highest number of classes possible in  
551 the unsupervised classification tool. By combining these classes in a way that they resemble larger optical spatial units ~~best~~,  
552 we eventually defined 43 Types of alteration surface (Types 1-4) ~~and 3) and the unaltered surface (Type 4) and further~~ analyzed  
553 their spectral characteristics and spatial distribution. Boxplots of the distribution of RGB values in the 32 classes and the  
554 spectral range of Type 1-4 surfaces are shown in Appendix A. The optical structure of the fumarole field and alteration zone  
555 is similar to the thermal structure and will be discussed in Chapter 4.32.

### 557 3.3 Infrared analysis - thermal structure and time series analysis

558 The SfM-derived infrared mosaic represents the thermal radiation in a 16-bit tiff format, resembling values between 0 and  
559 65536. To obtain a temperature map from the IR mosaic we calculated the apparent pixel temperatures  $T_p$  by

$$560 T_p \text{ (in K)} = \text{grayvalue} * 0.04 \quad (1)$$

561  
562 where  $T_p$  is the apparent pixel Temperature in K, the gray value is the radiation value of the original infrared mosaic and 0.04  
563 is the scaling factor (radiometric resolution). The temperature map was used to define the thermal structure ~~was analyzed by~~  
564 ~~defining temperature thresholds above~~. We observed several distinct thermal spatial units with temperatures significantly  
565 above the background temperature, that highlight thermal spatial units ~~best~~. A temperature threshold of  $T > 40^\circ\text{C}$  was used to  
566 highlight ~~can be distinguished in~~ high-temperature fumarole/fumaroles (HTF in the following) locations ~~and a threshold of~~  
567  ~~$> 22^\circ\text{C}$   $40^\circ\text{C}$  (min.  $5^\circ\text{C}$  above background) highlights and~~ areas of a rather diffuse thermal surface heating (Figure 4 B/D). To  
568 constrain these units spatially for further comparison, we had to approximate spatial boundaries what was done after  
569 comparison to our optical data and based on knowledge of previous observations by defining the temperature thresholds of  $T$   
570  $= 22\text{-}40^\circ\text{C}$  for the diffuse heated areas and  $T > 40^\circ\text{C}$  for HTF. The  $40^\circ\text{C}$  threshold resembles well the known locations and

598 extent of HTF in the upper and lower fumarole field. To compare the thermal emissions of detected structural units, we  
599 calculate radiant flux and the radiant exitance values by applying the modified Boltzmann law.

$$600 \quad Q = e \cdot b \cdot A \cdot (T_p^4 - T_o^4) \quad (2)$$

601 The emissivity ( $e$ ) was assumed to be 0.95 (often used as an assumption for volcanic surfaces), the Boltzmann constant ( $b$ ) is  
602  $5.670737 \times 10^{-8} \text{ Wm}^{-2}\text{K}^{-4}$ , the area of a pixel ( $A$ ) is  $0.024 \text{ m}^2$ .  $T_p$  is the pixel temperature and  $T_o$  is the average background  
603 mean temperature, calculated based on 9 reference areas that are anomaly-free-free. To compare identified units quantitatively,  
604 we summarized the radiation per pixel for the respective units a-g to a cumulative thermal radiation (Rcum). The flight altitude  
605 of 150 m (above the fumarole field) in combination with the low resolution of infrared sensors results in a pixel resolution of  
606 0.38x0.38 x 0.38 m.

607 Note that remotely sensed Infrared data always represents apparent temperatures that might differ from the real object  
608 temperature due to the radiation properties of the measured object itself (emissivity), the distance of the sensor to the measured  
609 object, the pixel-to-object size ratio, but also due to atmospheric or hydro-meteorological effects (Ball and Pinkerton, 2006)  
610 influencing the detected radiation values. Therefore apparent temperatures typically are lower than in situ vent temperatures.  
611 Real fumarole vent temperatures can reach more than  $300^\circ\text{C}$  (Diliberto, 2013) while temperatures in our infrared mosaic range  
612 to max.  $163^\circ\text{C}$  only. With this data set, we do not aim to provide precise fumarole temperatures but to analyze the thermal  
613 structure of the fumarole field and the broader field of activity.

### 615 3.4 Ground-truthing by Mineralogical and geochemical analysis Geochemical Analysis

#### 616 3.4.1 Rock sampling

617 Rock samples were collected at predefined representative locations aiming to include all alteration end members, during field  
618 campaigns in 2019 and 2022. We sampled along 3 transects following the postulated hydrothermal alteration gradients and  
619 crosscutting major alteration units, of which transect A is located on the lower fumarole field, transect b along the upper crater  
620 rim, and transect c is located in the eastern crater crosscutting several alteration units (locations for samples in chapter  
621 4.2.2Figure 7). Samples were in the size of  $\sim 2000 \text{ cm}^3$  (hand-sized) retaining the undisturbed surface crust, but also subsurface  
622 material to a depth of  $\sim 10 \text{ cm}$ . The samples were mechanically crushed, ground to  $63 \mu\text{m}$ , and split for XRD and XRF analysis,  
623 respectively. In total 21 samples were collected of which 9 were prepared for the XRD and XRF analysis and 12 for XRF  
624 analysis exclusively.

### 654 3.4.2 X-ray diffraction (XRD)

655 Between 1 and 3 mg of whole rock powder was used to determine the mineral composition of each sample through powder X-  
656 ray diffraction (pXRD). The analysis was conducted using a PANalytical X'pert diffractometer equipped with an X'Celerator  
657 silicon-strip detector at the Department of Geoscience, Swedish Museum of Natural History, Stockholm. The instrument was  
658 operated at 45 kV and 40 mA using Cu-K $\alpha$  radiation ( $\lambda = 1.5406 \text{ \AA}$ ). Samples were analyzed between  $5^\circ$  and  $70^\circ$  ( $2\theta$ ) for 20  
659 min in step sizes of  $0.017^\circ$  in continuous scanning mode while rotating the sample. Data were collected with "divergent slit  
660 mode" and converted to "fixed slit mode" for Rietveld refinement. The collected data show several peaks of X-ray diffraction  
661 intensity which represent the characteristic of crystalline minerals, the proportions of mineral phases were then refined using  
662 the Rietveld refinement method in the High Score Plus 4.6e software. The XRD analytical procedure was performed twice for  
663 each sample to ensure optimal quality control. Some samples contained contents of amorphous material of more than 50%.  
664 Those will be marked with a \* in the following but we will consider the mineral composition normalized to 100 % non-  
665 amorphous material. ▲

### 666 3.4.3 X-ray fluorescence (XRF)

667 Bulk chemical composition was determined by X-ray fluorescence analysis (XRF) at the EIMiE Lab at the German Center for  
668 Geosciences (GFZ). Main and trace elements were measured on fused beads with an AXIOS spectrometer (Malvern  
669 Panalytical, UK). Loss of ignition (LOI) was determined by analysis of H<sub>2</sub>O/CO<sub>2</sub> using an Eltra element analyzer.  
670 Reproducibility was determined on three certified reference materials (CRM) and is within the analytical precision, which is  
671 better than 2% for main elements and better than 10% for trace elements. ▲

### 672 3.4.4 Surface degassing measurements (CO<sub>2</sub>, SO<sub>2</sub>, H<sub>2</sub>S)

673 The surface degassing was measured at ~ 200 points within the northern part of the La Fossa cone (Figure 6) in September  
674 2021 and November 2022 using a simplified multi-gas accumulation chamber approach (Appendix B). The measurement unit,  
675 a Dräger XAM 8000 handheld Multigas device, was equipped with 6 sensors measuring CO<sub>2</sub>, CH<sub>4</sub>, SO<sub>2</sub>, H<sub>2</sub>S, H<sub>2</sub>, and O<sub>2</sub>  
676 simultaneously of which CO<sub>2</sub>, SO<sub>2</sub>, and H<sub>2</sub>S are considered here. The simplified accumulation chamber approach was an  
677 adaption as a consequence of uncertainties encountered in previous multi-gas measurement campaigns. Due to different sensor  
678 reaction times for ascending and especially descending gas concentrations, the comparison of direct sensor readings might  
679 lead to odd gas ratios with an artificial shift towards magmatic components. For that reason, we use the slope of the ascending  
680 gas concentration within a defined volume as quantification for a relative surface flow. More detailed information about the  
681 gas measurement approach is provided in the supplementary materials. Note that the aim of the gas measurements was not to  
682 provide accurate flux estimates but to highlight the spatial variability of the gas flow of certain gas species from the surface.

## 4 Results

### 4.1 Thermal- and optical anomaly ~~pattern~~patterns reveal the degassing and hydrothermal alteration structures

Degassing and hydrothermal alteration at La Fossa as seen in drone imagery can be traced by mainly two effects.

1) The transition from unaltered to hydrothermally altered surface can be traced by a general color shift in the drone images from reddish to grayish (~~Figure~~Figures 2A and 4A). This allowed us to constrain a distinct ~~~770~~70,000 m<sup>2</sup> sized area surrounding the fumarole field in a circumferential manner. This area is hereafter referred to as the Alteration Zone (ALTZ in Figure 4A/B), and represents the maximum extent of ~~at-~~surface observable alteration effects that can be associated with the fumarole field. It includes effects ranging from weak surface alteration to strong alteration with intense surface bleaching and remineralization, to complete destruction of the host material. The extent of the ALTZ exceeds the area covered by the high-temperature fumarole (HTF) site by ~50 times (Figure 4A/B), indicating the widespread influence of diffuse degassing and alteration processes.

2) Within the ALTZ we observe a segmentation characterized by brightness and color variability expressed in different shades of gray (Figure 4A), the second optical effect, indicating local alteration gradients. Analyzing the ALTZ for this spectral variability by PCA and image classification we can constrain pixels of low-, increased-, or intense surface bleaching and alteration (light blue, dark blue, and red pixels in Figure 4B) and define an alteration index represented by 4 surface Types (1-4), of which Type 1 is the most altered and Type 4 the least altered surface.

Type 1 surfaces are bright grayish intensely bleached surfaces or sulfuric deposits and represent the strongest alteration end members that we can detect optically from our data. Type 1 mainly resembles the fumarole sites and surrounding areas (Figure 4 A/B) but also larger isolated regions that can not be associated with major vent systems. With increasing distance to the degassing centers, we observe a shift towards darker grey (Type 2) and brownish (Type 3) surface colors. **Type 2** is characterized by a gray but comparatively less bright coloring. It typically occurs at the boundaries between Type 1 and Type 3 regions and largely surrounds Type 1 areas, but it also forms several isolated clusters typically embedded in Type 3 areas (units b,d,g in Figure 4). Type 3 is generally darker and more reddish in color, similar to the unaltered parts of the crater surface, but can be well distinguished from the unaltered surfaces by PCA. It makes up ~50% of the ALTZ and dominates in the central northern and the ~~south-eastern~~southeastern parts. Type 4 is a reddish, apparently oxidized surface that dominates the La Fossa cone surrounding the ALTZ.

The surfaces within the ALTZ are generally mixed and composed of more than one type. The ALTZ is characterized by a generally high density of Type 3 pixels, with locally high densities of Type 1 and Type 2 pixels, which then become the dominant surface Type and form larger spatial units, indicating locally higher alteration gradients or larger structural units (units a-g in Figure 4 and details in Appendix C). The largest of these units cover several thousand square meters each. The thermally active surface (Figure 4C) can be divided into high-temperature fumaroles (HTF in Figure 4D) and diffuse thermally active surface (green pixels in Figure 4D). HTFs are the visible part of the activity that can be constrained by the

naked eye in the field, while the diffuse thermally active surface is largely imperceptible. The thermally active surface largely mirrors the alteration pattern observed in the optical data. An analysis of the temperatures obtained at all pixels of Type 1 to 4 surface ~~shows~~ shows a general increase of mean pixel temperatures from Type 4 to Type 1 surface by an average of 2 degrees (Figure 5). In particular, areas dominated by Type 1 and 2 surfaces reflect the thermal structure well while areas of Type 3 dominance largely coincide with low-temperature surfaces (Figure 4 B/D). An additional Spearman correlation test, applied to the classified surface (32 classes unsupervised, for comparison see Appendix A) and the thermal data (in °C) shows a moderate positive correlation between optical and thermal anomalies (Appendix D). This shows that the detected optical anomalies are meaningful and that degassing and alteration variability occurs even at local scales and can be traced in our close-range drone remote sensing data.

The spatial coincidence of both optical and thermal anomalies highlights the relationship between variations in the surface coloration, caused by alteration processes, and the ongoing influence of diffuse gas flow. A general coincidence of increasing brightness (simultaneously increasing the RGB values) with increasing surface temperature of an area can be constrained (Figure 5).

#### 4.2 Anomaly structure ~~revealed~~ identified from optical and thermal data

The optical and thermal anomalies form distinct spatial units of alteration and elevated surface temperature (units a-g in Figure 4D), which now allow us to infer the following surface structure of the fumarole field and its wider field of activity.

The centers of degassing activity are high-temperature fumaroles (HTF). These are the “visible” ~~part~~ parts of the activity that can be perceived in the field (red pixels in Figure 4D). We spatially constrain the HTFs based on apparent temperature values with  $T \geq 40$  °C in our 150 m overflight data. Using this as a threshold we find that the HTFs cover an area of 1223 m<sup>2</sup>, and occur exclusively in the Type 1 surface. However, HTFs represent only a fraction of the active surface.

The total extent of the surface that has to be considered active is much larger. The surface with elevated temperature covers ~30000 m<sup>2</sup> (green pixels in Figure 4D,  $T \geq 22$  °C or 5 °C above the background), exceeding the area covered by HTF by a factor of 25. The surface that is considered hydrothermally altered (ALTZ ~70,000 m<sup>2</sup>) exceeds the area covered by HTF by a factor of ~60, highlighting the widespread influence of diffuse degassing and alteration processes.

Besides the HTF we have constrained larger units of elevated surface bleaching and surface temperatures that can be considered structurally important and centers of diffuse degassing activity.

Units a and b are diffuse features of increased surface bleaching (Type 1 and 2) and surface temperature, embedded in the Type 3 surface and surrounding the eastern fumarole field in the form of an aureole shape. Neither can be associated with major vents. The observed maximum surface temperature for unit a is 43.7°C (0.43 m resolution) and the average temperature is 25°C, ~8-°C above the background. It is located at a distance of 25 to 50 m downslope from the eastern rim fumarole complexes, separated by a low-temperature zone (LTZ). Unit b, the southern part of the aureole is a 120 m long and 20 - 35 m wide anomaly located subparallel on the inner side of the crater. It extends over ~2100 m<sup>2</sup> and has a maximum surface temperature of 46°C and an average temperature of 26°C (9-°C above the background). The temperature range and spatial extent of units a and b are comparable. In the field, both are difficult to identify as there is little or no evidence of degassing

849 (Appendix E). Like unit a, unit b is also separated from the main fumarole vents by the LTZ. Its northern boundary corresponds  
850 exactly to the positions and curvature of the fumarole alignments at a relatively constant distance of 30 meters. In unit b, we  
851 observe a temperature gradient with higher temperatures at greater distances from the fumarole vents and an apparently more  
852 active center in the ~~south-eastern~~southeastern corner. Another thermal anomaly with a similar shape and orientation is located  
853 further south inside the crater. ▲

854 Units d and f are similar aureole-like features in the western fumarole field, associated with fumarole complex F0. They  
855 circumferentially surround fumarole complex F0 at a distance of 5 to 15 m, also separated from the HTF by a Low-Temperature  
856 Zone (LTZ), but to a lesser extent than that observed for units a and b of the eastern fumarole field. The southwestern section  
857 of this aureole, unit d, appears as a larger heated complex with stronger surface bleaching (Type 1) and higher temperature  
858 (mean  $T=27^{\circ}\text{C}$ ), and a temperature gradient with higher temperatures further away from the major fumarole complex. The  
859 boundary to the low-temperature zone is sharp with a sudden drop in temperature of 10 to  $20^{\circ}\text{C}$  and a strong associated color  
860 shift (Appendix C). The aureoles of F0 and F11 have in common that they are encircled by a network of polygonal net-shaped  
861 thermal anomalies in the far field. ▲

862 Low-temperature zones (LTZs) dominate the central parts of the fumarole field. The LTZ have only slightly elevated  
863 temperatures relative to the background ( $18\text{-}21^{\circ}\text{C}$  or  $1\text{-}4^{\circ}\text{C}$  above background) and can be optically constrained by a darker  
864 Type 3 surface coloration. From field observations, we have ~~constrained~~concluded that these LTZ form a strong, apparently  
865 sealed surface complex. Therefore LTZ might indicate largely sealed sections of the fumarole field which inhibit gas flow at  
866 the surface. The 3 central LTZ1-3 (Figure 4D) cover an area of  $\sim 12,000\text{ m}^2$ . ▲

867 Unit c is a broad complex of highly altered material (Type 1) and significantly high surface temperatures. It is potentially the  
868 most altered member in the central crater region. It covers an area of  $\sim 8000\text{ m}^2$  and the maximum and average apparent  
869 temperatures observed are  $87^{\circ}\text{C}$  and  $29^{\circ}\text{C}$ . It is associated with the HTF FA and F58. Considering the thermal structure of  
870 unit ec, it is a heterogeneous unit formed by a network of higher temperature anomalies embedded in lower but, with respect  
871 to the background, significantly increased tempered surface. This area is associated with the northwestern crater unit, which is  
872 the most recent explosion crater. ▲

873 Unit d is an area of diffuse activity associated with the inner crater part of fumarole complex F0, showing a significant shift in  
874 surface colorization and temperature, some 20 m away from the fumarole complex. The boundary is distinct and visible to the  
875 naked eye (Type 3 to Type 1). The temperature shift is on the order  $> 20^{\circ}\text{C}$ .

876 Unit e is a large branching thermal and optical anomaly of the upper fumarole field. It can be constrained by its gray coloration  
877 embedded in the reddish unaltered surface and also by its increased surface temperature. It is a 120 to 150-m-long branch-  
878 shaped network of anomalies on the inner crater wall. The central feature is oriented E-W and located  $\sim 20\text{ m}$  south and below  
879 the helicopter platform and the crater rim. We constrained its size to  $\sim 2500\text{ m}^2$  (only the western branch, without intersection  
880 to hunit d) and the recorded maximum and average apparent temperatures are  $45.0^{\circ}\text{C}$  and  $25.9^{\circ}\text{C}$  respectively. Some smaller  
881 clusters of localized degassing, alteration, and increased surface temperature, visible at the surface by its bright coloration, are  
882 observed in the northern section of the fumarole field (unit g) towards La Forgia. ▲

916

## 917 **4.23 Ground truthing - verification of observed anomalies**

918 We have carried out mineralogical (X-ray diffraction) and geochemical (X-ray fluorescence) analyses of bulk rock samples  
919 collected at representative locations and surface degassing measurements. The aim is to verify the observed anomaly pattern  
920 of alteration gradients and distinct active units; and to investigate the relationship between the optical and thermal anomaly  
921 pattern and modern degassing and hydrothermal alteration processes. In this way, we provide ground truthing and demonstrate  
922 that the anomalies observed are significant.

923

### 924 **4.23.1 Present-day surface degassing pattern**

925 The measurements of diffuse degassing from the surface allow us to compare the present-day surface degassing pattern to the  
926 observed optical and thermal anomalies (Figure 6 A/B). We performed surface degassing measurements of CO<sub>2</sub>, H<sub>2</sub>S, and SO<sub>2</sub>  
927 simultaneously in the diffuse degassing regime at 200 measurement points (~100 points within and outside the ALTZ)  
928 throughout the whole northern crater section (details of gas measurements in Appendix B).

929 The observed relative flux values for CO<sub>2</sub> range from 0 to ~9000 ppmv/s with an average of ~900 ppmv/s. They are  
930 considerably higher ( $\times 10^3$ ) than the SO<sub>2</sub> and H<sub>2</sub>S flux at the respective locations. For both, SO<sub>2</sub> and H<sub>2</sub>S a maximum gas flux  
931 of < 10 ppmv/s was measured and the average is below 0.5 ppmv/s.

932 Looking at the spatial distribution of the measured ~~gasgasses~~ we observed generally higher gas levels within the alteration  
933 zone ALTZ and at the ALTZ boundary, for each of the measured gas (Figure 6 C/D). The average CO<sub>2</sub> flux is 660 ppmv/s  
934 outside the ALTZ and 923 ppmv/s within the ALTZ. Thus, the averaged CO<sub>2</sub> flux inside the ALTZ is about 1.4 times higher  
935 than outside; but is particularly high in some of the constrained units a-g. However, the CO<sub>2</sub> flux has a wide spatial distribution  
936 and high flux values of above 2000 ppmv/s can also be observed outside the ALTZ and at a distance to the ALTZ boundary  
937 (Figure 6 A/C).

938 SO<sub>2</sub> and H<sub>2</sub>S in contrast appear spatially ~~stronger~~more strongly confined, and significant flux values can be exclusively  
939 observed within the ALTZ (Figure 6 B/D). Values for SO<sub>2</sub> and H<sub>2</sub>S inside the ALTZ exceed the outside-ALTZ values by 13  
940 and 15 times. This higher diffuse flux, although at average low concentrations, might promote a surficial process of chemical  
941 weathering and surface bleaching, potentially causing the observed color shift from a reddish-oxidized surface toward gray  
942 and will be discussed further based on analyses of the geochemical composition of rock samples in Chapter 5.2.

943 Comparing the surface degassing to the observed optical and thermal anomaly pattern (Figure 6 E-G), we see that high values  
944 were observed especially in units a or b on the eastern side of the fumarole field, coincident with increased alteration (Type 1  
945 and 2) and thermally active surface, followed by other constrained units c-g. However, the strongly bleached and apparently  
946 highly altered unit c shows, other than expected, rather small ~~values~~gas fluxes, although its surface temperature is significantly  
947 increased with respect to other identified units. This might indicate reduced surface permeability and surface sealing processes  
948 and will be discussed in ~~chapter~~Chapter 5.3.

981 While SO<sub>2</sub> or H<sub>2</sub>S flux values for Type 1 and 2 surfaces are increased, only low fluxes were constrained for the Type 3 surface  
982 and no flux for the unaltered surface (un in Figure 6 E-G). Note that the central sections of the fumarole field were not sampled  
983 due to the close vicinity to HTF and expected high flux values. The data shown here is only representative for the diffuse  
984 degassing domain. ▲

#### 986 4.23.2 Mineralogical composition of the alteration gradients

987 XRD Analysis was performed along two transects A and B, and XRF analysis was performed on samples taken along three  
988 transects A-C (Figure 7), crossing postulated alteration gradients. ▲

989 Transect A crosses from the unaltered surface over Type 3 into the Type 1 surface (T3-T1 boundary in Figure 7) of the highly  
990 altered unit c. Transect B is oriented along the HTF on the crater rim in an east-west orientation from Type 1 surface into the  
991 LTZ (Type 3). Transect C crosses the eastern fumarole field from the unaltered surface, through the Type 1 and 2  
992 surfacesurfaces in unit B, the LTZ (Type 3) on both sides of the HTF, to Type 1 and 2 surfacesurfaces, and eventually the  
993 unaltered material outside the ALTZ. This transect represents the variability in the rather diffuse degassing regime as no  
994 samples close to the HTF were used for the analysis. ▲

995 Results of all samples support local alteration gradients within the ALTZ and show significant changes in the mineralogical  
996 and geochemical compositions (Table of XRD results in Appendix F). The dominant mineral phases observed in samples of  
997 transects A and B are sanidine, cristobalite, and elemental sulfur (Figure 7). Additionally, most samples contain amorphous  
998 material, representing glassy phases typical for volcanic sequences. For comparability, mineralogical concentrations refer to  
999 the crystalline phase, while amorphous contents are stated with respect to the total. Note, however, that bulk rock geochemistry  
1000 refers to both phases and cannot analytically distinguish between amorphous and crystalline. ▲

1001 Considering compositional changes along transect A we observe a high proportion of sanidine feldspar and lesser cristobalite  
1002 in the relatively unaltered samples (Type 4). With an increasing degree of alteration, we observe a general loss of cristobalite  
1003 and sanidine while sulfur contents increase (Figure 7). Samples from the unaltered reddish Type 4 surface (A1) outside the  
1004 ALTZ and Type 3 surface (A2/3) inside the ALTZ are similar in composition and show high sanidine and cristobalite contents  
1005 of 86-87 % and 13-14 % in the crystalline part, respectively, yet low to no sulfur contents. These samples were taken in areas  
1006 of no or only slightly increased surface temperatures of < 22 °C (i.e. < 5 °C above the background). Samples A4-6 are taken  
1007 in unit c, a complex of high alteration and increased mean surface temperatures of 28 °C (~10 °C above background). In this  
1008 strongly altered unit, cristobalite is absent, along with a decrease in sanidine to 60-70 % relative to the least altered samples  
1009 and an increase in sulfur contents of up to 20-40 % in the crystalline portion of the rock sample. However, the amorphous  
1010 components constitute a high proportion of these sample(s), showing ca. 50 % in samples A6 and B1. ▲

1011 Samples taken on the upper rim along transect B in the high-temperature fumarole regime (V-AHT) contain total sulfur  
1012 contents of 50 to 100 %, while cristobalite is absent in these samples. Sample B3, a piece of grayish crust is taken from LTZ3

1046 (~21°C, 4°C above background) in between the high-temperature fumaroles F0 and F5 and contains 100% sulfur, highlighting  
1047 the precipitation and sealing potential of degassing activity at the surface.

1048 Comparing the changes of surface coloration with changes in the mineralogical composition we can constrain no significant  
1049 effect at the ALTZ boundary, i.e., the transition from unaltered to altered surface (A1-A2/3), although the optical effect is  
1050 major. However, significant compositional changes, e.g. the complete loss of cristobalite and increasing sulfur content are  
1051 observed at the ALT - AMT boundary (blue mark in Fig. 6), coincident with the shift from Type 3 to Type 1 surface into unit  
1052 c.

### 1053 **4.23.3 Bulk geochemical composition of the alteration gradients**

1054  
1055 For samples without amorphous fraction, bulk geochemical composition correlates reasonably well with mineralogy  
1056 determined by XRD, assuming ideal stoichiometry. The difference between theoretical bulk composition and true composition  
1057 is within 10% of the respective element, which we consider a good estimate given sample heterogeneity. Only for sample A5,  
1058 the high Mn content remains unmatched by XRD analysis. Subtracting the theoretical bulk composition of the crystalline  
1059 fraction from the true bulk composition, we can thus estimate the chemical composition of the amorphous fraction. The  
1060 amorphous fraction is similar to the crystalline counterpart mainly composed of SiO<sub>2</sub> and some minor (< 5 wt%) phases, as  
1061 well as elevated Mn contents. The high Mn contents were only observed in samples with medium alteration and elevated  
1062 temperatures, both in samples with and without a significant contribution portion of amorphous material. It is thus likely that  
1063 Mn is contained in the crystalline phase, yet could not be detected due to the high SiO<sub>2</sub> signals derived from sanidine and  
1064 amorphous material.

1065 The bulk geochemical composition (Figure 7 and data table in Appendix G) agrees with the mineralogical composition. All  
1066 samples are high in SiO<sub>2</sub> content and, therefore, can be considered to belong to the large silicic-alteration complex earlier  
1067 described by Fulignati et al. (1999). The samples show a slight variability of SiO<sub>2</sub> between 67-82 wt. % and plot on the rhyolite  
1068 field within the TAS diagram (Middlemost, 1994; not shown here). The amorphous component, typical for rhyolite, consists  
1069 of mainly SiO<sub>2</sub>, with minor amounts of Fe and Al, based on the difference between the theoretical and actual geochemical  
1070 composition calculated from stoichiometric mineralogy. Three samples also have significant MnO, possibly caused by  
1071 hydrothermal leaching and precipitation as amorphous crusts. However, the variability of MnO will not be detailed further in  
1072 this study.

1073 Dominant in transect A is the loss of Al<sub>2</sub>O<sub>3</sub> from the unaltered Type 4 surface (> 10 wt.%) outside ALTZ to the Type 1 surface  
1074 of the highly altered unit c (< 0.4 wt.%). Similarly, Fe<sub>2</sub>O<sub>3</sub> is decreasing from an average of 1.6 to 0.3 wt.%. The loss of Al<sub>2</sub>O<sub>3</sub>;  
1075 and Fe<sub>2</sub>O<sub>3</sub> is likely related to the alteration of sanidine and the elution of iron- and aluminum-sulfates formed due to the contact  
1076 with sulfuric gas. The most significant changes occur, similar as observed in the mineralogy, not at the transition from unaltered  
1077 to altered (ALTZ-boundary) but at the ALT-AMT3-T1 boundary (blue line in Figure 7) at the transition from Type 3  
1078 to Type 1 surface.

1110 Transect C crosses from the unaltered surface through unit a, the northern LTZ, the southern LTZ, unit b, Type 3 surface, and  
1111 eventually the unaltered surface. Compositional changes from unaltered (Type 4) to altered (Type 1 and 2) surface of units a  
1112 and b, here, are minor with relatively stable values for  $\text{Al}_2\text{O}_3$  (6-12%),  $\text{Fe}_2\text{O}_3$  (1-3%),  $\text{TiO}_2$  (<0.5) and Mn (~0). At the  
1113 transition from active units a and b (Type 1 and 2 surface) to the LTZ (Type 3), we observe a significant increase of sulfur  
1114 content from <2% to 12-40%. However, this increasing sulfur content here is not coincident with the systematically brighter  
1115 surface color observed for other altered units. LTZ show the same rather dark surface observed for Type 3 surface elsewhere,  
1116 which is a discrepancy to the effects observed in the western fumarole field and indicates that LTZ have to be considered  
1117 subject to different surficial processes. This will be discussed in ~~chapter~~Chapter 5.3.

## 1119 5 Discussion

1120  
1121 ~~In this study, combining close range remote sensing, image analysis, mineralogical and geochemical analyses of rock samples,~~  
1122 ~~and the investigation of the present day surface degassing, we investigate the degassing and alteration structures of the~~  
1123 ~~fumarole field and the broader field of activity at La Fossa cone on Vulcano. Based on image analysis (similar to Müller et al.,~~  
1124 ~~2021) of new better quality drone derived high resolution image data, we resolve the general pattern of degassing and alteration~~  
1125 ~~effects at the surface, spatially constrain them and complement our previous work with more detail and extensive ground~~  
1126 ~~truthing. In our previous work parts of the central fumarole field could not be analyzed in detail due to stronger gas plume~~  
1127 ~~distortion in our image data. Also, some parts of the results presented here are results of additional and intense fieldwork and~~  
1128 ~~lead to an adapted interpretation of observed effects especially considering the diffuse activity pattern in the eastern fumarole~~  
1129 ~~field.~~

1130 ~~From UAS derived RGB imagery, we identified a ~70,000 m<sup>2</sup> sized zone that is outlining the maximum extent of observable~~  
1131 ~~alteration effects. We showed variability within the ALTZ that represents local alteration gradients or structural units. We~~  
1132 ~~show that effects of diffuse degassing and alteration can be traced far beyond the activity of high temperature fumaroles.~~  
1133 ~~Alteration effects can be observed in an area (ALTZ) that is actually ~50 times larger, and a thermally active surface that is~~  
1134 ~~~25 times larger than the area covered by high temperature fumarole complexes.~~

1135 ~~Analyses of mineralogical and bulk- Various studies have previously explored the geochemistry (e.g. Fulignati et al., 1999),~~  
1136 ~~petrology (e.g. De Astis et al., 1997), geophysics (e.g. Revil et al., 2008) and remote sensing signal (e.g. Mannini et al., 2019;~~  
1137 ~~Coppola et al., 2022) of the La Fossa crater, Vulcano island. In this study, we combine close-range remote sensing, image~~  
1138 ~~analysis, mineralogical and geochemical analyses of rock samples, and the study of the present-day surface degassing of the~~  
1139 ~~La Fossa crater and analyse the surface expression of hydrothermal activity. Through this combination of ultra high resolution~~  
1140 ~~(< 10 cm) drone image analysis with mineralogical/geochemical analysis, we are able to provide a holistic picture of the surface~~

1173 degassing and hydrothermal alteration pattern, highlighting an aureole-like organisation of the alteration field that distinguishes  
1174 distinct units that grade from inner high-temperature fumaroles to sealed surfaces (LTZ) and to diffuse degassing areas at a  
1175 greater distance. An area of approximately 70,000 m<sup>2</sup>, which we have termed the Alteration Zone (ALTZ), outlines the  
1176 maximum extent of observable alteration effects and highlights that degassing and alteration can be traced well beyond the  
1177 central high-temperature fumarole activity sites (HTF). The ALTZ is similar to the diffuse flux zone previously identified by  
1178 Mannini et al. (2019), and is in fact ~50 times larger than the area covered by the high-temperature fumarole domain. However,  
1179 from the optical data, we observe further variability within this zone expressed in active units a-g, which also coincide with  
1180 the diffuse thermal activity and cover 25 times the extent of HTF. Here we can further detail the surface structures and activity  
1181 patterns identified in previous works, (e.g. Harris et al., 2009; Mannini et al., 2019) which divide the active region into a vent  
1182 flux zone and a diffuse flux zone. In particular, we can further detail the vent flux zone by outlining high-temperature fumarole  
1183 locations based on high-temperature pixels. We further show that thermal radiation and gas flux of the ALTZ or diffuse flux  
1184 zone are not uniform but show strong local variability, with high fluxes in identified active units a-g and low fluxes in larger  
1185 parts of the central fumarole field associated with LTZ (Low-Temperature Zones) or the unaltered regime.

1186 Although the structural study is based solely on drone-derived imagery and thermal infrared data, our detailed observations of  
1187 local activity and alteration gradients are supported by variations in mineralogical and bulk geochemical compositions of  
1188 representative rock samples support our observations of local strong alteration gradients and allow to constrain relations  
1189 between remotely sensed surface coloration and degassing and alteration processes. A. Although we have performed a  
1190 classification of the image data in this work, already visual observations can show a general shift from reddish to gray surface  
1191 coloration allows us to infer color, which coincides with areas of increased diffuse gas flow. Variability Such color anomalies  
1192 can therefore be used as guide in the field. A variability in surface brightness and gray hues allows for the detection of coincides  
1193 with alteration gradients and major active units. A largely coincident, and the congruent optical and thermal anomaly pattern  
1194 highlights indicate the relation link between surface temperature and surface color and allows to constrain major structural units.  
1195 Some of these units represent large complexes of diffuse activity and are apparently important structural features for the  
1196 degassing system as will be discussed in chapter 5.3.

1197 The coloration and degassing-induced alteration processes. This relationship underlines the potential of the presented  
1198 combination of methods provides as an efficient tool for first-order site investigation of tool for volcanic degassing and  
1199 alteration systems and that can be applied to volcanoes elsewhere. Structural findings and implications for the degassing and  
1200 alteration system provide information for further and more detailed alteration research.

### 1202 5.1 Alteration Zone (ALTZ) controlled by sulfuric gassesgases and elution processes

1203 The ALTZ, is characterized by a surface color shift from reddish to gray, is coincident and coincides with the area of higher  
1204 SO<sub>2</sub>/H<sub>2</sub>S flux and apparently represents the appears to represent a zone of diffuse acid gas flow (Figure 4). All measurements

1237 with a significant flow of sulfuric gas species ~~were measured are from~~ inside the ALTZ, while the flux of CO<sub>2</sub> was ~~also high~~  
1238 ~~outsidewell beyond~~ the ALTZ.

1239 We, therefore, suggest the general color shift from reddish to gray to be related to ~~this a~~ higher flux of sulfuric ~~gassesgases,~~  
1240 promoting ~~a process of surficial~~ chemical leaching of iron oxides, via the reduction of the initially contained iron oxides to  
1241 iron sulfates, which are ~~easilystrongly~~ soluble in rain or ~~in~~ condensing water vapor and ~~are thus~~ prone to rapid elution. Iron  
1242 oxide content in our analyzed samples ranges from 1.5% ~~( sample A1)~~ in the unaltered regime, to 1.1-1.4 % for A2/3  
1243 samples, ~~and~~ to 0.3 for samples of the highly altered unit c (~~sample~~ A4-6). There is a gradual reduction following the postulated  
1244 alteration gradient, with the strongest changes ~~occurring onalong~~ the ~~ALT AMFT3-T1~~ boundary (blue line in Figure 7). The  
1245 1.5 % Fe<sub>2</sub>O<sub>3</sub> for our rock sample of the unaltered regime is a rather low value and might be related to the fact that the sample  
1246 was taken very close to the ALTZ boundary ~~and. It~~ consists of ~~> 50 %~~ amorphous material. Fulignati et al. (1999), who provide  
1247 a broader sampling database estimated Fe<sub>2</sub>O<sub>3</sub> contents of unaltered ~~1988-19901888-1890~~-eruptive products with 2.465-6.657  
1248 %, which reduces to an average value ~~of~~ below 1 % in the ~~siliesilicic~~-alteration regime (Fulignati et al., 1998; Fulignati et al.,  
1249 1999; Boyce et al., 2007).

1250 ~~Evidence~~Further evidence for chemical leaching ~~can also beis~~ found on the crater floor, where deposits form a colored layer  
1251 ~~resembling~~ the color spectra widely observed on La Fossa, with bright reddish deposits close to the fumarole field resembling  
1252 ~~elassie~~-fluvial patterns. We believe that the optically anomalous gray surface at Vulcano can generally be used to infer areas  
1253 of present higher ~~acid~~ gas flux or former discharge of acid ~~gasses at even low flux rates-gases~~. Analyzing the broader area of  
1254 the central crater region, we can infer multiple other areas where we observe similar ~~(changes of colorization that indicate~~  
1255 ~~similar argillic or strong silicic alteration effects at the surface. These are located on the southern inner crater, the outer crater~~  
1256 ~~rims, the 1988 landslide area (Madonia et al. 2019) and the northern flank towards Vulcano Porto. These zones of strong~~  
1257 ~~alteration are indicated in red in Figure 1B or Müller et al., (2021).~~

## 1259 5.2 Alteration gradients on local scales

1260 With average high SiO<sub>2</sub> contents of ~~> 70 %~~, the sampled areas correspond to the large silicic alteration complex suggested by  
1261 Fulignati et al. (1999), Azzarini et al. (2001), Boyce et al. (2007), and others. In our study, we show evidence for strong local  
1262 alteration gradients and structurally important units, ~~and~~ spatially constrain them, ~~and thus we complement-detail to~~ earlier  
1263 studies.

1264 Color shifts observed within the ALTZ ~~associated with units a-g~~ (brightness effects, hues of gray) are likely controlled by the  
1265 degree of hydrothermal alteration, secondary mineral formation, and especially sulfur content in the respective surface samples.  
1266 Coincident with characteristic changes in the surface coloration from Type 4 towards stronger bleached surfaces of Type 1,  
1267 we observe a relative decrease of the initial mineral and element composition ~~by simultaneously increasing-and a simultaneous~~  
1268 ~~increase in~~ sulfur content (~~Figure 7~~) for most of the obtained samples. (~~Figure 7~~). While sulfur content in Type 1 surface ranges

1301 from 6 to 31 %, for Type 2 it is already below 2 %, and for the unaltered fraction, it is below 0.2 %. We can, therefore, confirm  
1302 a general link between alteration gradients, sulfur contents, and surface brightness (or surface Types) in our remote  
1303 sensing data (Figure 8). ▲

1304 An exception from this systematic trend are sulfur contents of the Type 3 surface. Here we observe two distinct clusters; (Figure  
1305 8), one with values below 0.5 % and one with extraordinarily high sulfur contents of 12 to >60 %, both showing a similar  
1306 surface coloration. All Type 3 samples with high sulfur contents are exclusively taken from LTZ. This strong discrepancy of  
1307 sulfur content and surface coloration within the low-temperature zones suggests next to alteration gradients also surficial or  
1308 shallow processes of mineral deposition and formation of sulfur-rich encrustations that form sealed surfaces, especially in the  
1309 near field of fumaroles. The low temperatures observed within LTZ and the limited surface degassing highlight the efficiency  
1310 of such sealing processes. So far we can not distinguish LTZ from Type 3 surfaces in our optical data (Figure 8). A distinction,  
1311 however, would be beneficial as it would provide a method allowing for the precise spatial constraint of sealed surfaces from  
1312 simple UAS-derived RGB imagery. ▲

1313 The intensity of optical and thermal effects and associated changes in mineralogical, ~~or~~ and chemical composition ~~or~~, and  
1314 degassing are not always equally significant. Although the general shift from unaltered surface to altered surface (ALTZ-  
1315 boundary, shift reddish to gray) is a major criterion for the identification of degassing and alteration extent in our data, the  
1316 associated changes in compositions are minor (Figure 9). The larger changes are observed within the ALTZ at the ALT-  
1317 AMFT3-T1 boundary; (Figure 7). Here we observe a sudden decrease in the initial mineral and bulk geochemical composition  
1318 and equally an increasing sulfur content. We interpret the rather low changes at the transition from unaltered to altered at the  
1319 ALTZ boundary to be related to rather weak or surficial alteration effects. The size of obtained samples was on the order of  
1320 ~2000 cm<sup>2</sup>, including the surficial part, but also material up extends down to ca. 10 cm depth. This way, it was not possible to  
1321 trace mineralogical or geochemical changes at the surface only. The samples obtained at the ALT-AMFT3-T1 boundary, on  
1322 the other hand, show strong changes and reveal the general systematics of alteration effects, especially those samples taken in  
1323 unit c, which might be considered one of the strongest alteration end members of the central crater region. ▲

1324 The identified surface patterns with respect to alteration gradients and structural units result from long-term evolution.  
1325 However, some features may be subject to rapid changes. During the volcanic crisis in 2021, we observed, for instance, the  
1326 formation of a new fumarole complex, which will locally change the composition, sulfur content, and surface type considered  
1327 (cf. Figure 11), as is the case with sulfur deposits at the surface that can change quickly due to rainfall.

### 1329 5.3 Heat budget - evidence for diffuse activity and surface sealing

1330 Based Heat budgets, on the gained information we Vulcano have been studied earlier by e.g. ground-based surveys or satellite  
1331 data (Chiodini et al., 2005; Harris et al., 2009), providing a range of estimates of thermal emissions (Mannini et al., 2019;  
1332 Silvestri et al., 2019; Coppola et al., 2022). We compare our results to those using a remote sensing approach. Mannini et al.

(2019) outlined a diffuse flux zone, which is comparable to the ALTZ defined by us. Further, they divided this zone into a diffuse flux zone and a vent flux zone and estimated the thermal radiation.

We outlined the surface structure of the degassing and alteration system of Vulcano (simplified in Figure 10 and detailed views of the different alteration and thermal units in Appendix C) and based on the detection and classification of optical and thermal anomalies supported by additional mineralogical, geochemical, and degassing information, and spatially constrained high-temperature fumaroles (HTF), major diffuse active units besides the HTF. To quantify a-g, and Low-Temperature Zones (LTZ). We quantified their importance for the degassing and alteration system, we weigh them based on a comparison of by calculating their thermal energy release (according to the Boltzmann Law (Eq2 and Figure 10) for both, the contribution of anomalies with  $T > 22^{\circ}\text{C}$ , and identified units based on a spatial constraint, also including values  $< 22^{\circ}\text{C}$ . Therefore our identified structure differs from the vent flux and diffuse flux zone shown by Mannini et al. (2019).

High-temperature fumaroles of the upper fumarole field in our study have high average radiant exitance values of  $82 \text{ W/m}^2$  but can only account for 28 % of the total emitted thermal energy (calculations based on pixels with  $T > 22^{\circ}\text{C}$  and a corrected background of  $T = 16.71^{\circ}\text{C}$ ). The rest of the thermal energy is released by the diffuse features described above. ( $= 16.71^{\circ}\text{C}$ ). Note that when considering pixels with  $T > 40^{\circ}\text{C}$  (as outlined by red patches in Figure 4D) the cumulative radiation of HTF would decrease to 0.2 MW only and the radiant exitance would increase to  $242 \text{ W/m}^2$ . The rest is released by the diffuse degassing part of the system. Although a direct comparison may be difficult, due to different outlines chosen for the respective flux zones, different sensor systems, and different background correction values, our cumulative radiation ( $R_{\text{cum}}$  in Figure 10) for the HTF is comparable to those of Mannini et al. (2019). These authors suggested a vent zone heat flux of 0.35-0.96 MW. Our estimate was  $\sim 1 \text{ MW}$ , of which 0.5 MW are contributed by the high-temperature fumarole vents and 0.52 MW by unit c. This is also in accordance with the findings of Coppola et al. (2022), who estimate a similar vent zone flux from VIIRS imaging bands.

Next However, the contribution of the diffuse thermal regime approximated by us is lower compared to the HTF estimates in other studies (e.g Mannini et al., 2019), which place the contribution of the diffuse flux zone (comparable to our ALTZ) on the order of 90 % of the total flux. This is likely related to the fact that we did not estimate the flux of the ALTZ in total, but of multiple larger anomaly units within the ALTZ that have apparent structural importance for the degassing system. This becomes evident when analyzing the and contribute  $\sim 50 \%$  to the total flux. For future studies, a distinction into 3 different thermal regimes, a vent flux / high-temperature fumarole zone, a diffuse active units for their (like a-g shown in this study), and a broader low-temperature anomaly field (diffuse flux zone/ ALTZ) may be recommended to better resolve close range thermal-infrared remote sensing information with data from satellite-based studies.

Regarding the heat budget estimated by us, the most dominant diffuse unit in terms of thermal energy release (Figure 10).

The second important unit is unit c. It has the second-highest average radiant exitance of  $76 \text{ W/m}^2$  but and exceeds the cumulative radiant flux of HTF with a contribution to the total thermal radiation of with 29 %. Although it is % of the total thermal radiation, the cumulative radiation of the HTF. Unit c is not only a highly altered complex with a strongly the strongest

bleached surface and increased surface temperatures, there is also a discrepancy to the current degassing activity. Relative gas flux values measured within unit c are lower than observed for units a and b, for instance. This phenomenon might be a consequence of the dynamics of hydrothermal alteration and indicate permeability reduction or sealing processes due to the more advanced state of hydrothermal alteration like proposed by (cf. Heap et al., 2019-). This would be proposition is supported by a strong variability the strongest changes in mineralogical and bulk geochemical composition and associated remineralization or observed in our samples, implying mineral (re-)precipitation observed in is a major process in this particular unit e-.

Diffuse aureoles (unit a/b) on the eastern side of the fumarole field cover several thousand m<sup>2</sup> each, more than the area covered by HTF, and. The diffuse aureoles contribute with 6 to 7 %, or about 25 % of the energy emitted by the HTF % each, to the total thermal energy release. Additionally, the, equivalent to 25 % of the energy emitted in the high-temperature zone (HTF + unit c). Their bleached surface, increased surface temperatures (Figure 4), and higher gas flow flux values (Figure 6 E-G) highlight their importance for the surficial surface gas-drainage capability. However, mineralogical and bulk-chemical data suggests that the degree of alteration is less in these units, compared to unit c. This observation suggests that these sections are younger and therefore less altered and highlights their importance for the present-day degassing system.

Unit Units d and e are large diffuse features degassing domains of the western fumarole field of which unit d is a part of the thermal aureole surrounding F0 and unit e is a ~200m 200 m long branched anomaly, located rim parallel west of F0. Both have a similar contribution to the total thermal energy release than as units a and b. Unit d is separated from by F0 by a low-temperature zone (LTZ3). The transition from LTZ 3 LTZ3 to unit d is sudden and accompanied by a temperature jump of ~20°C. The difference in the average temperature between unit d and LTZ3 is on the order of 5-°C. Also here we observe apparent surface sealing for the whole central fumarole field. Unit f, the northern section of the F0 aureole, and anomalies in the area north of the fumarole field (unit g) have a minor contribution.

LTZ1 The Low-Temperature Zones (LTZ) 1-3 separating, which separate diffuse aureoles from the HTF, have a Type 3 surface coloration, significantly lower temperatures, and radiant flux and exitance values than the neighboring aureole regions, which what indicates processes of surface sealing. Indeed, no gas flux could not be constrained for the LTZ of the eastern fumarole field. From field observations and lab analyses (Figure 7), we constrained the LTZ as strong, sulfur-rich surface complexes which are apparently that effectively sealing seal the surface and inhibiting inhibit gas flow escape. The depth of these sealed complexes can not be constrained by our data, but we can roughly constrain approximate the spatial extent. Considering only the 3 LTZ LTZs of the central and eastern fumarole field, they together cover at least ana total area of ~12000m<sup>2</sup>, which is a significant fraction of the ALTZ. In other words, ~20 % of the surface of the ALTZ is apparently sealed and, which forces lateral gas flow to the aureole regions. This was proven by observations during the 2021 volcanic crisis at La Fossa. While at fumarole sites and diffuse active units like units a and b showed increasing an increase in mean temperatures and thermal energy release, the radiation within LTZ remained stable and low, highlighting the efficiency of sealing processes the proposed seal. This was observed for all central LTZ LTZs, and is exemplarily demonstrated by exemplified in a cross-section through the eastern fumarole field section (Figure 11D).

1490 **6 Conclusion**

1491 Our investigation of the fumarole field of the La Fossa cone allowed us to constrain the degassing and alteration structure,  
1492 define major, so far undescribed units of activity, and quantify their importance for the degassing system, highlighting in  
1493 particular large diffuse degassing areas and localized surface sealing. Our experience from the study of the degassing and  
1494 alteration system at Vulcano demonstrates that close range remote sensing. Such high-resolution studies can greatly contribute  
1495 to the understanding of structural architecture or and add to our understanding of the intrinsic complexities of fumarole fields.  
1496 Such This realisation has implications for hydrothermal alteration studies, particularly for the identification of local variability,  
1497 since local variations are frequently associated with mechanical, chemical, and permeability contrasts. The recognition of such  
1498 contrasts is of use for an improved assessment of volcanic and degassing activity, but also possibly for other hazard aspects,  
1499 such as e.g. stability assessments. We anticipate that combined remote sensing and petrological studies will prove beneficial  
1500 for pre-site reconnaissance surveys for hydrothermal energy exploration, the detection of sampling locations for alteration-  
1501 related studies and sampling grid design, and, importantly, for regular routine hazard monitoring of hazardous volcanic crater  
1502 areas and associated risk assessment.

1503  
1504 **7 Tables**

1505 **Table 1:** Overview of the processed data sets that were used for the following analyses. From The optical data, an  
1506 orthomosaic and DEM were generated covering 3.74 km<sup>2</sup> with pixel resolutions of 8.6 ~~x~~ 8.6 to 17.3 x 17.3 cm. From the  
1507 high altitude infrared overflight, an infrared mosaic was acquired covering 3.23 km<sup>2</sup> with 41.238 x 41.238 cm resolution. All  
1508 data sets cover the complete central section of the La Fossa cone.

Data set	Acquisition date	Pixel resolution in cm	Coverage in km <sup>2</sup>	Point density in p/m <sup>2</sup>
2019 orthomosaic	14.11.2019	8.6 x 8.6	3.74	135.20
2019 DEM	14.11.2019	17.3 x 17.3	3.74	33.41
2018 IR mosaic	15.11.2018	<del>41.2</del> <u>41.238 x 38</u>	3.23	5.64

1520  
1521  
1522  
1523  
1524

1525 **8 Figures**

1526

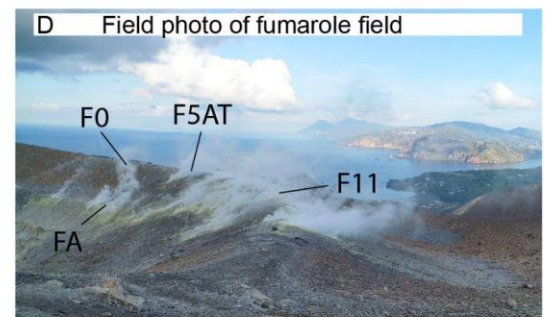
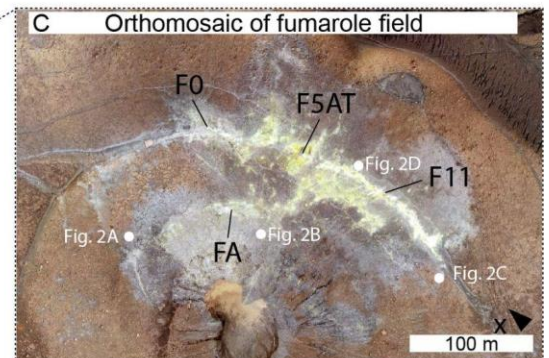
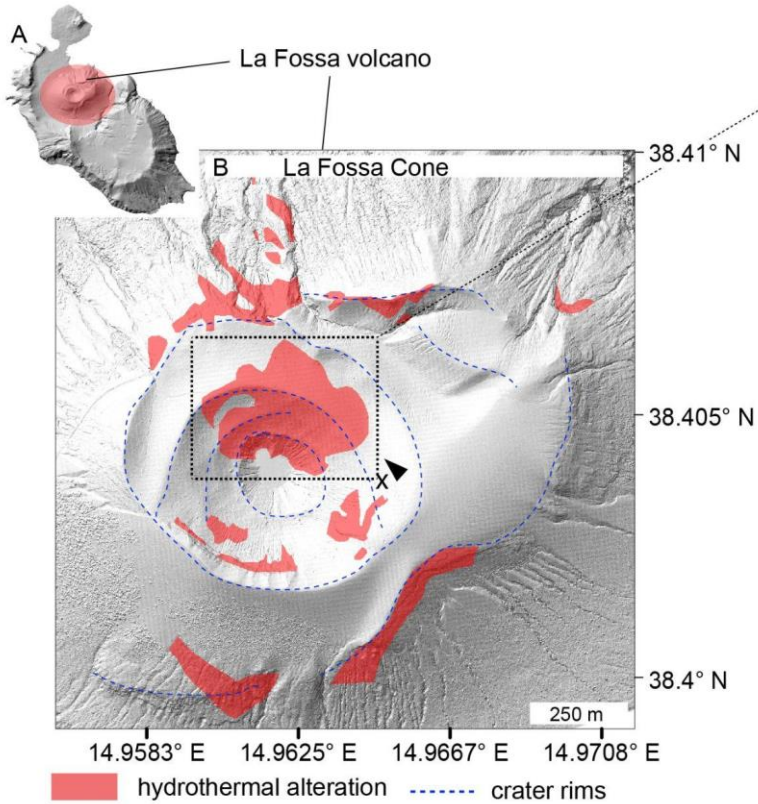
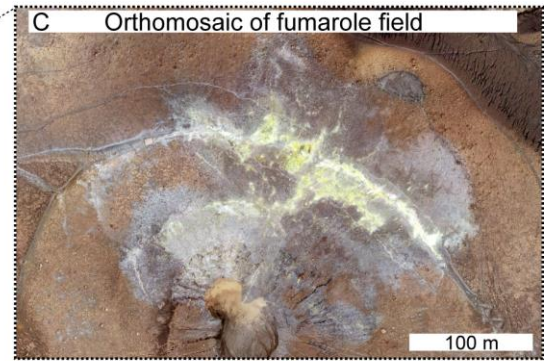
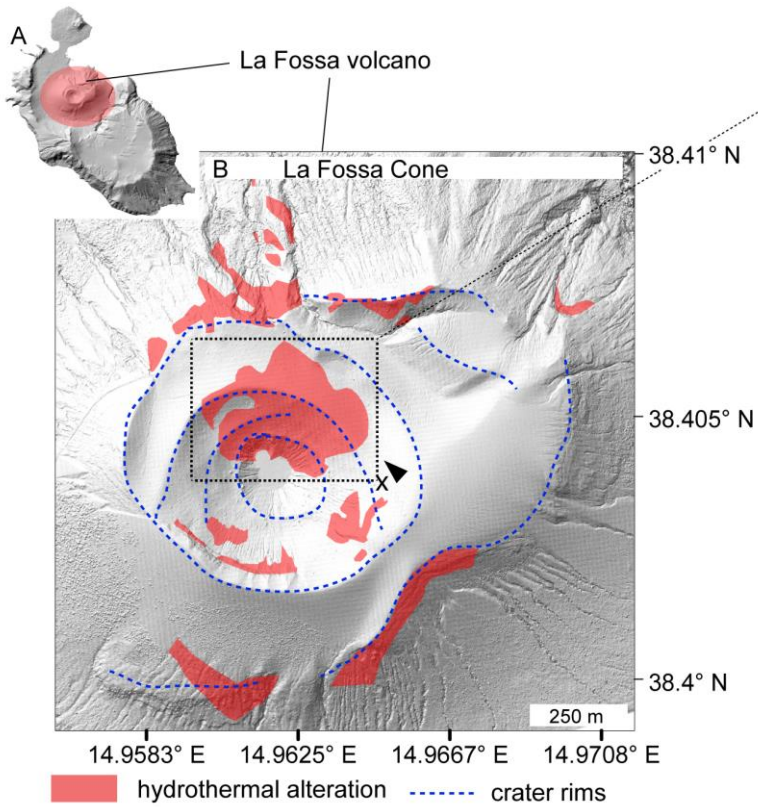


**For**  
**For**  
**For**  
**For**

25

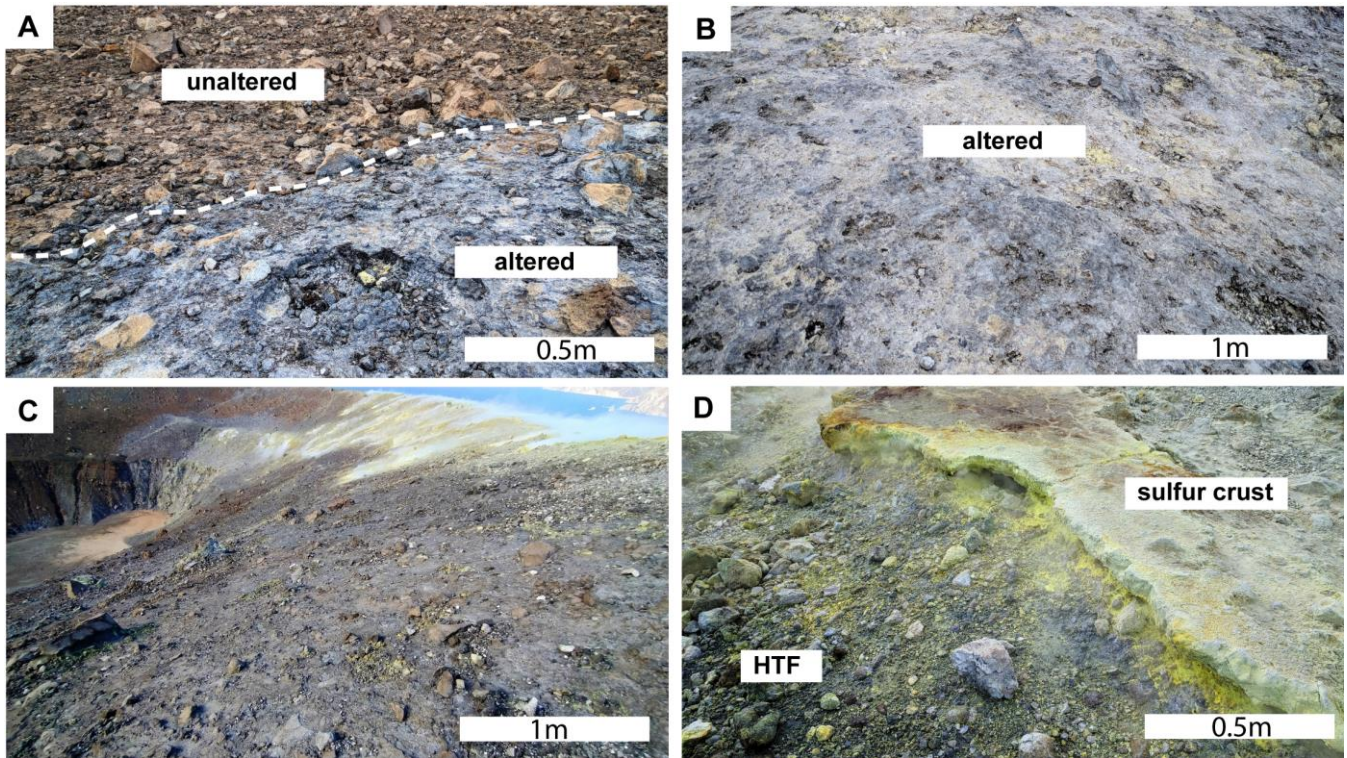


**For**  
**For**  
**For**  
**For**



For  
bor  
bor  
For  
For

1539 Figure 1: Overview of the degassing sites at La Fossa cone, Vulcano Island (Italy). A) Vulcano Island as a shaded relief map.  
 1540 The red circle indicates the location of the La Fossa cone. B) Central summit region of the La Fossa Cone. Blue dashed  
 1541 lines depict craters and rims from different eruptive episodes. Areas of degassing and hydrothermal alteration are  
 1542 highlighted by red patches after following Müller et al. (2021). The dashed box outlines the most prominent center of  
 1543 degassing and alteration, the high-temperature fumarole field. C) The birds-eye view of the high-temperature fumarole field  
 1544 from a birds-eye view with prominent fumaroles F0, F5AT, F11 and FA marked. The locations of field photographs of Figure  
 1545 2 are indicated by white dots. D) Field photograph overphoto of the fumarole field. Location and viewing direction are  
 1546 indicated by an x and an arrow (B/C).  
 1547



1548

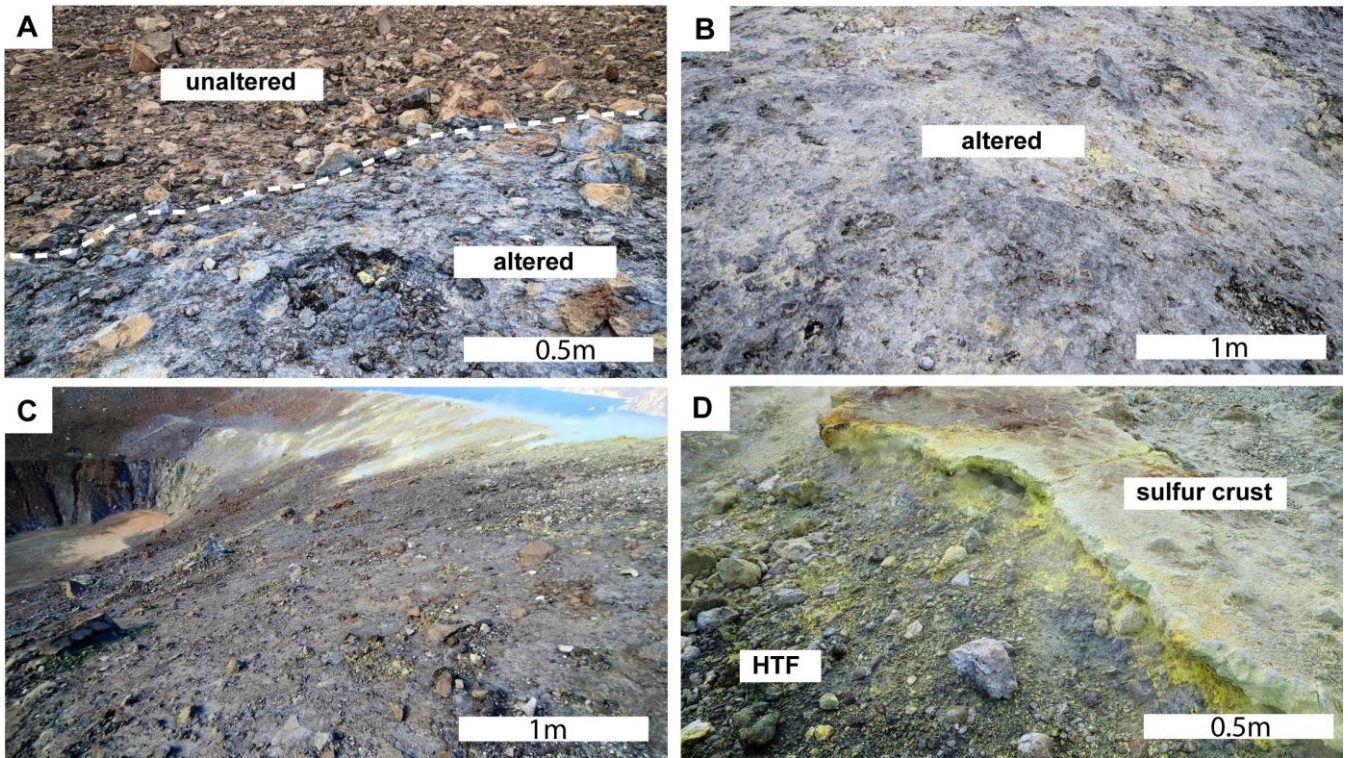


Figure 2. Different surface types and colorations in the La Fossa cone. A) Transition from unaltered to altered bleached surface. B) Intensely altered and bleached surface. C) View from the east onto sealed surfaces D) High-temperature fumarole (HTF) and deposited sulfur crust.

1556  
 1557  
 1558  
 1559  
 1560  
 1561  
 1562

For  
 bor  
 bor  
 For  
 For

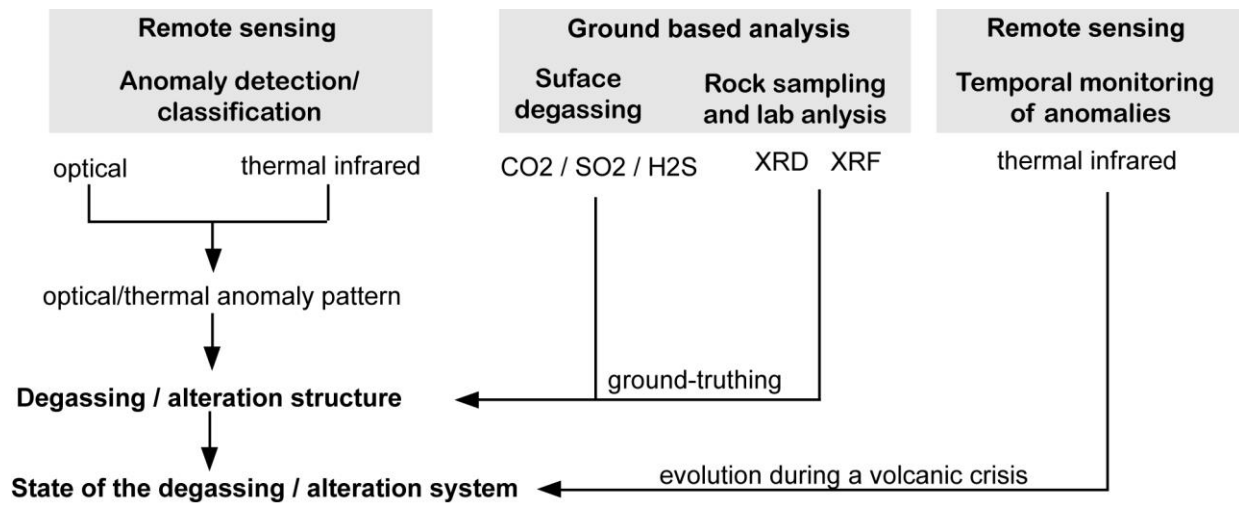
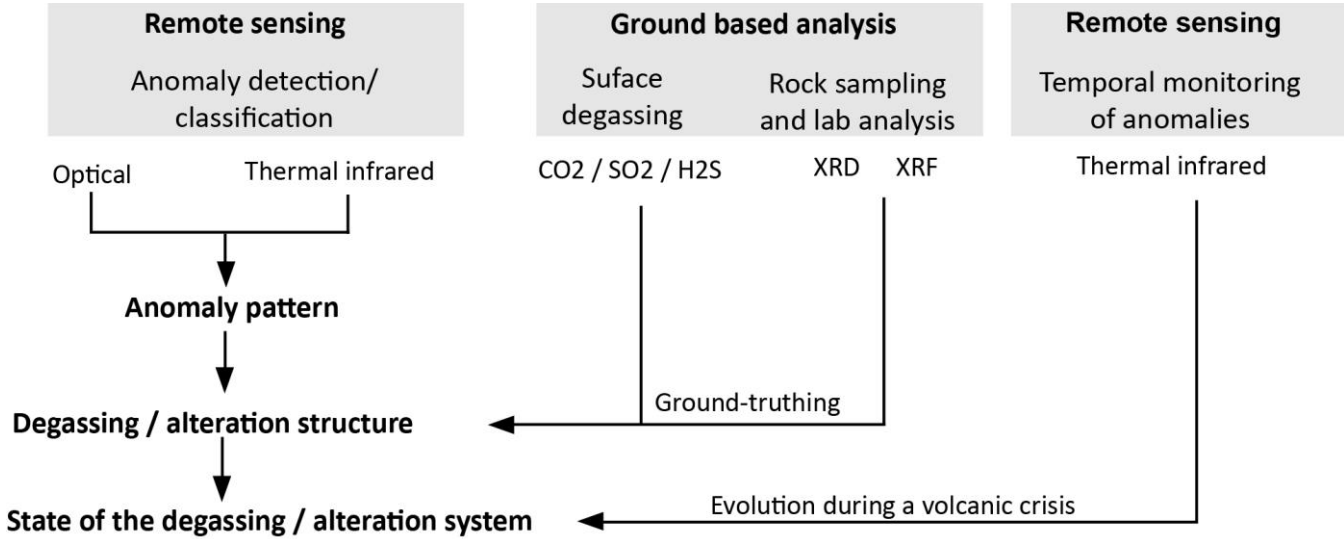
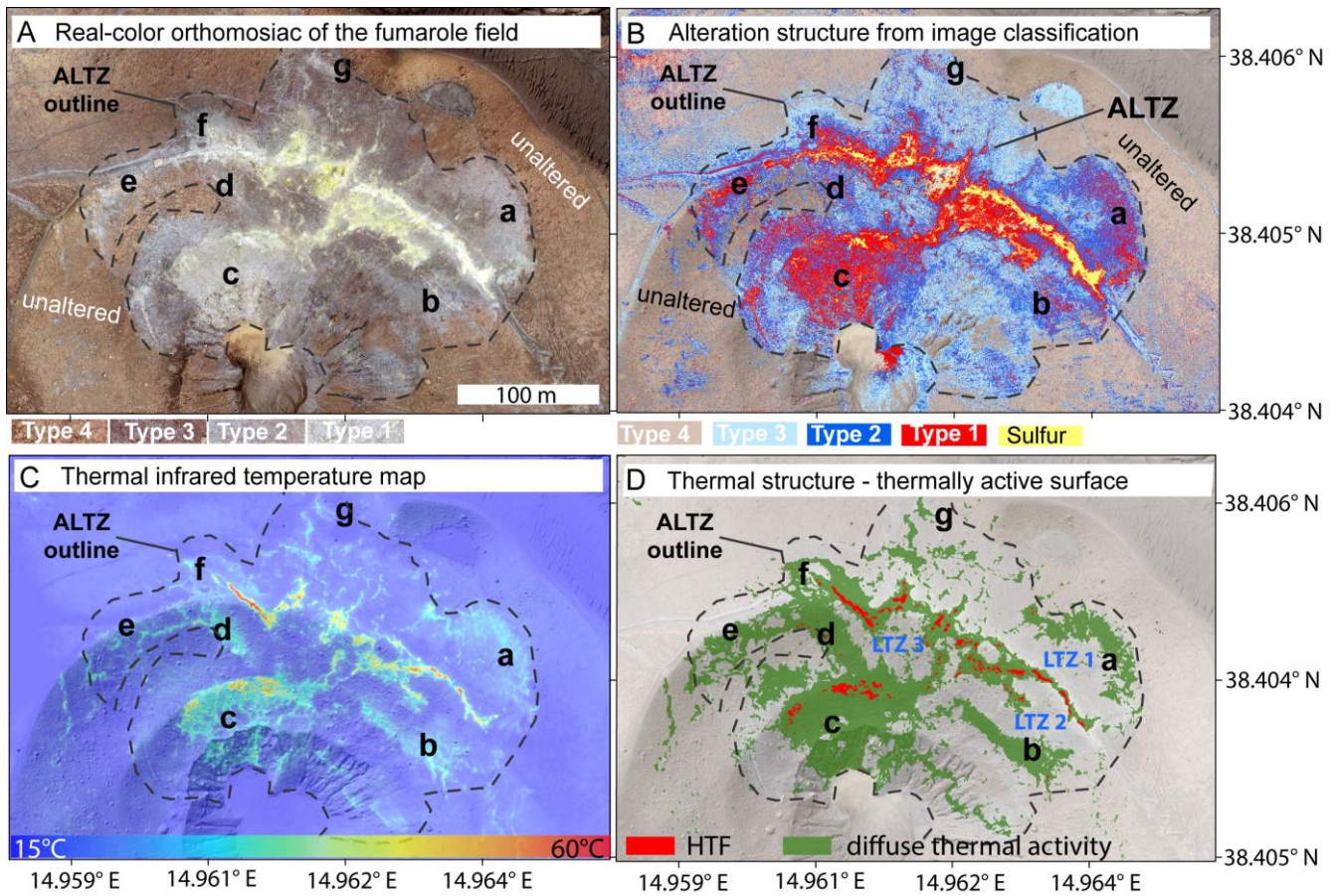


Figure 3: General workflow from anomaly detection from remote sensing data to ground truthing by mineralogical and geochemical investigation.

1590  
1591  
1592  
1593  
1594

For  
bor  
bor  
For  
For



1597

1598

Figure 3: Overview of the general workflow used for this study. An anomaly detection from optical and thermal infrared

For  
bor  
bor  
For  
For

remote sensing data allows us to reveal the anomaly pattern and infer the surface structure of the degassing and alteration system. To validate the observed structure, the remote sensing study was complemented by surface degassing measurements revealing the present-day degassing pattern, and by X-ray diffraction (XRD) and X-ray fluorescence (XRF) analysis of selected rock samples to prove different alteration units based on changes in mineralogical and bulk-chemical composition. Continuous monitoring by high-resolution thermal remote sensing data allows to record dynamics within the system and to draw conclusions about the general condition of the degassing/alteration units, e.g. with regard to alteration-related processes like surface sealing.

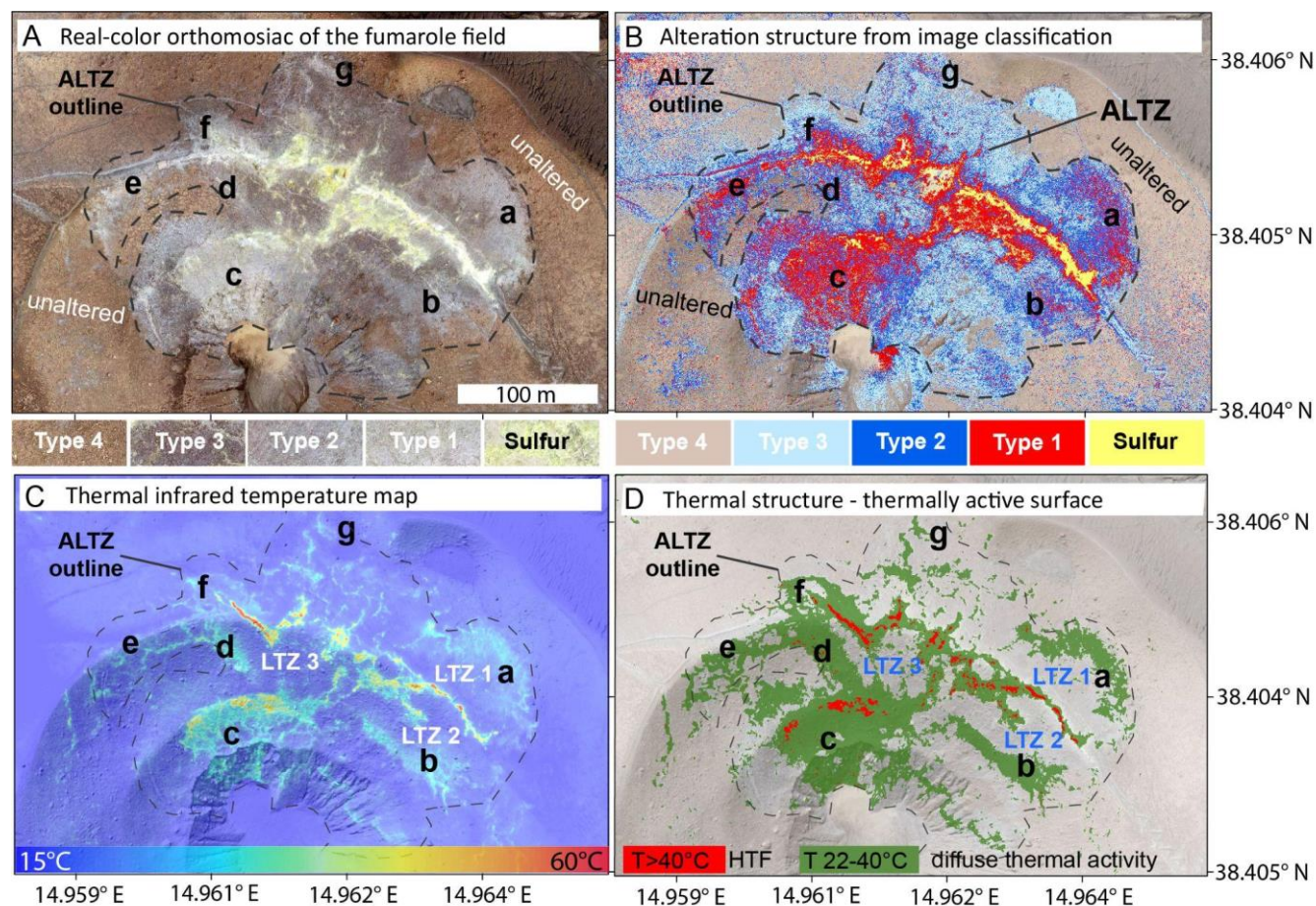


Figure 4: Alteration structure of the La Fossa fumarole field. A) True color image of the high-temperature fumarole field with color samples of the surface types 1-4 and sulfur at the bottom of Fig. A. B) Alteration structure of the fumarole field as revealed by PCA and image classification, represented by the classified surface types 1-4 and sulfur at the bottom of Fig. B. C) Thermal infrared image temperature map of the fumarole field. D) Simplified thermal structure of the fumarole field

1634 highlighting high-temperature fumarole location in red ( $T > 40\text{ }^{\circ}\text{C}$ ) and diffuse thermal activity in green. ~~Labels ( $T = 22\text{-}40$~~   
1635  ~~$^{\circ}\text{C}$ ). The dashed line labeled ALTZ outline demarks the boundary of visible optical effects at the surface and is referred to by~~  
1636 ~~us as ALTZ (Alteration Zone). The labels a-g~~ ~~represent~~ ~~demark~~ notable large-scale anomaly units that can be observed in both,  
1637 the ~~alteration~~ ~~optical~~ data and ~~the~~ thermal data. ~~L TZ 1-3 demark low-temperature zones that separate the high-temperature~~  
1638 ~~fumaroles and diffuse active units and cover significant parts of the central fumarole field.~~ Note that the contrast of the  
1639 background image has been reduced for highlighting in Subfigures B and D.

1640

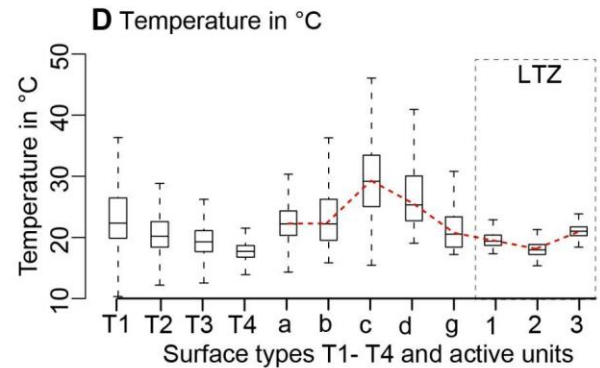
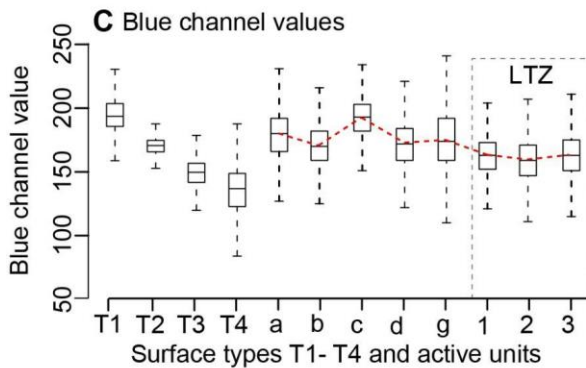
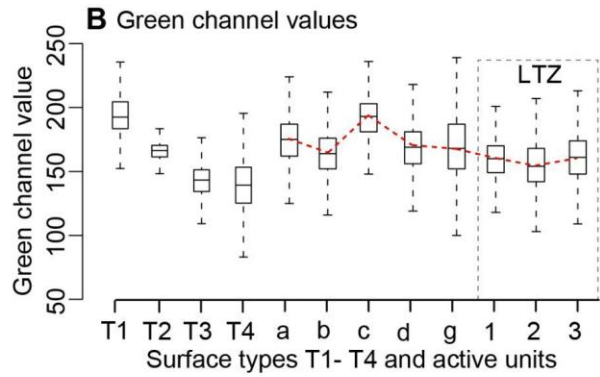
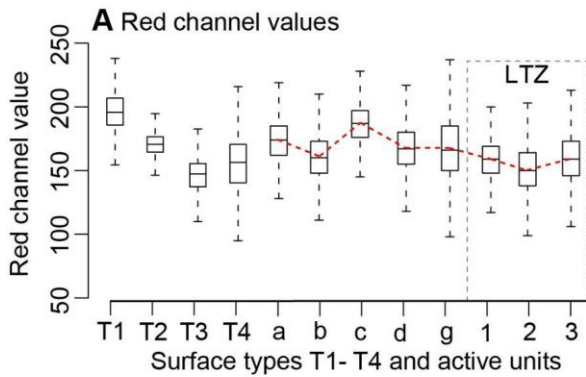
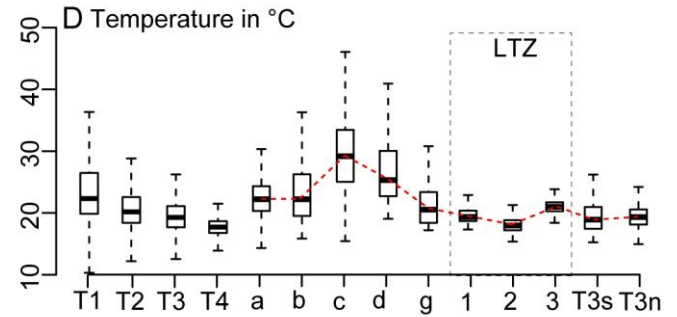
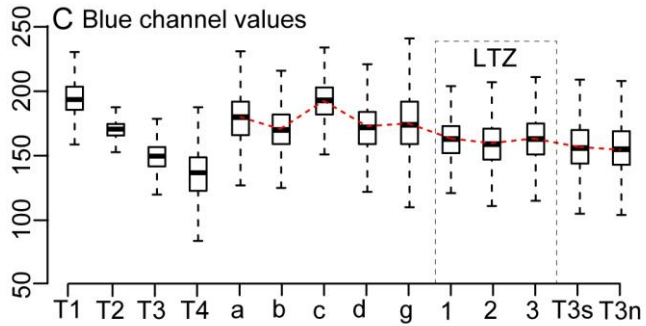
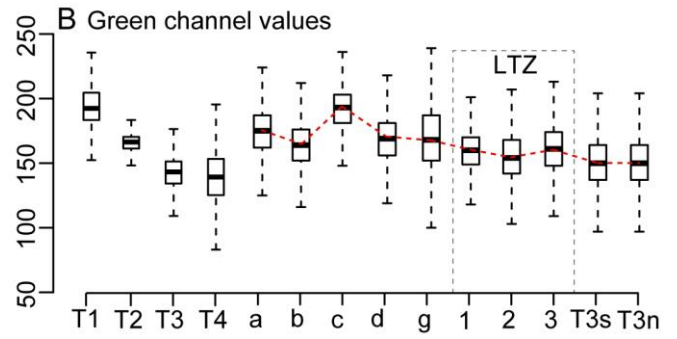
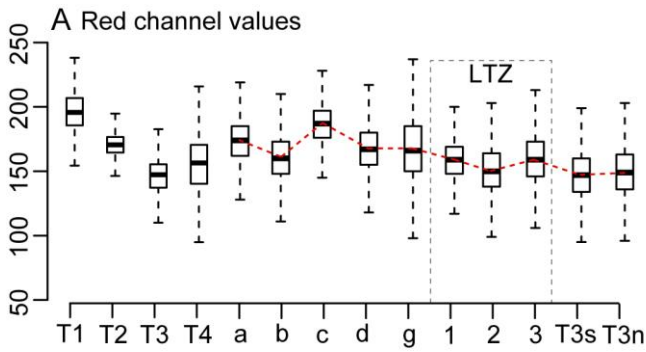
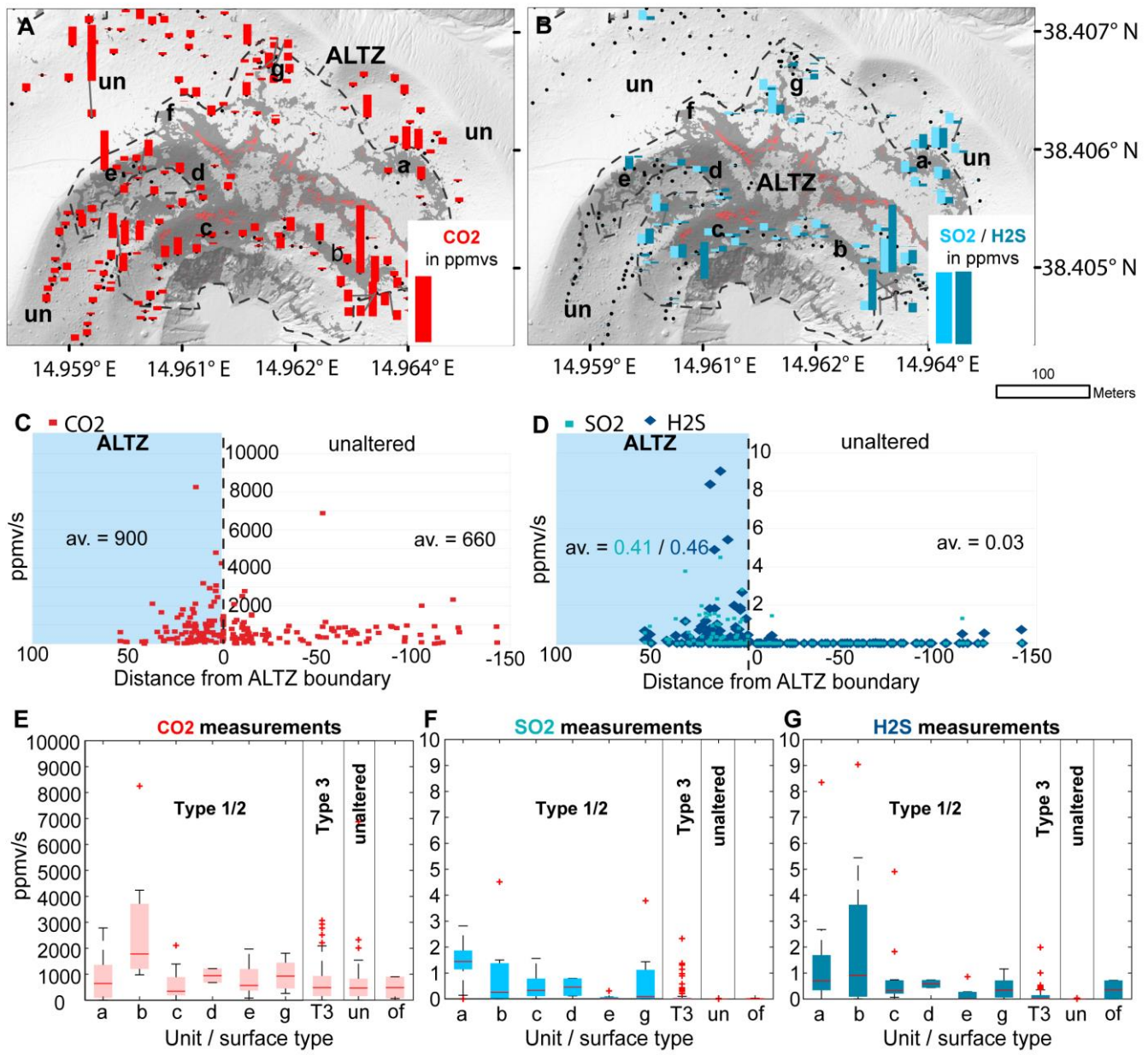


Figure 5: ~~Color~~Boxplots of RGB color value- and temperature distributions observed for the different surface Types 1-4 (T1-

For  
bor  
bor  
For  
For

1652  
1653  
1654  
1655  
1656  
1657

T4), selected areas identified active units a-g, and associated low-temperature zones LTZ1-3 (location see, Surface types and locations of identified units are depicted in Figure 4B/D). A) Red color channel value distribution. B) Green color channel value distribution. C) Blue color channel value distribution. D) Temperature value distribution. Values are based on an analysis of 6.8 million pixels within the ALTZ. Both, the optical (Figure A-C) and thermal (Figure D) value distributions show similarities with generally decreasing values from the T1-T4 surface, a peak in unit c, and low values for LTZ1-3.



1658

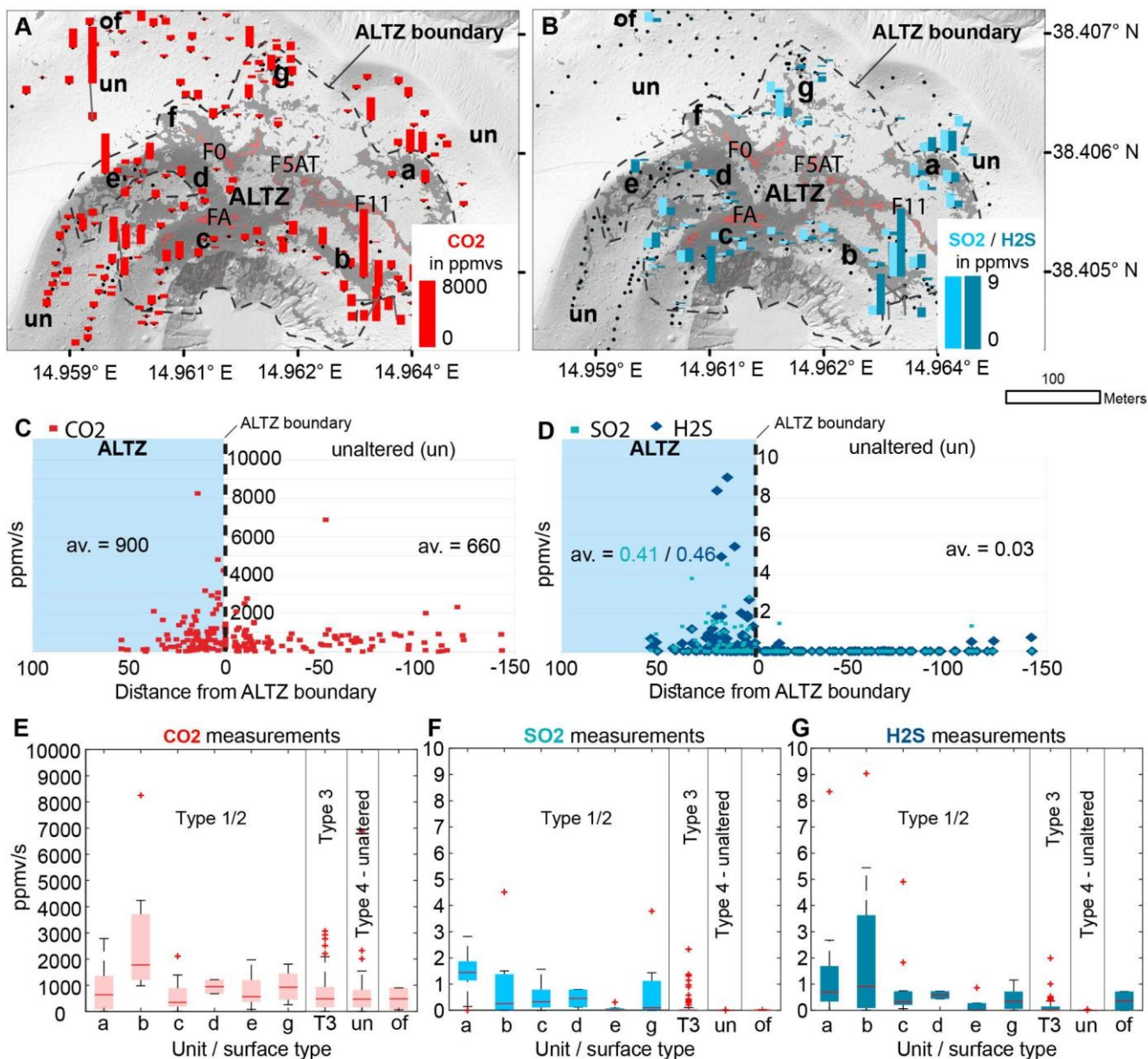
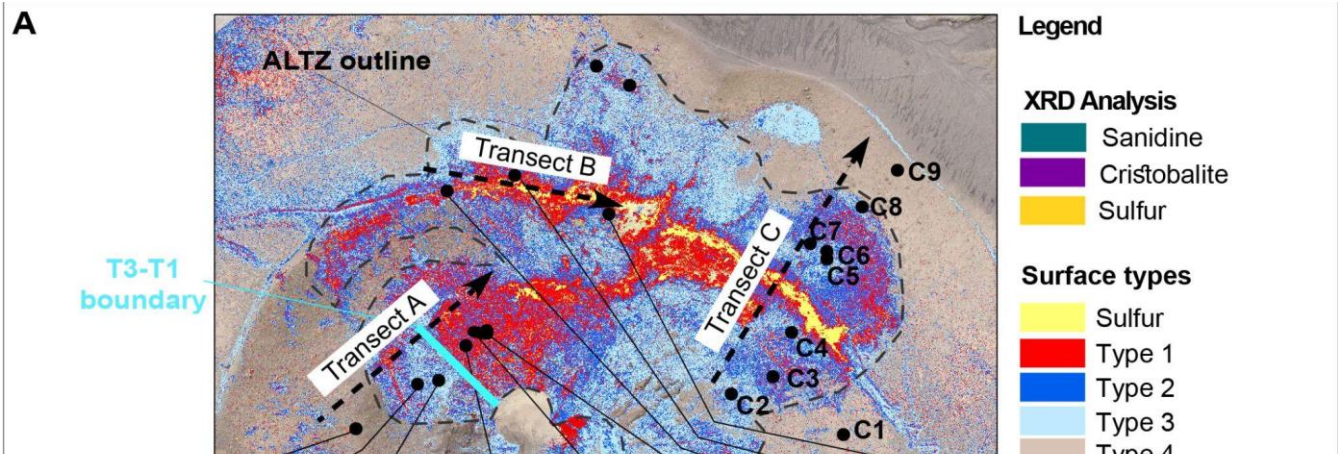
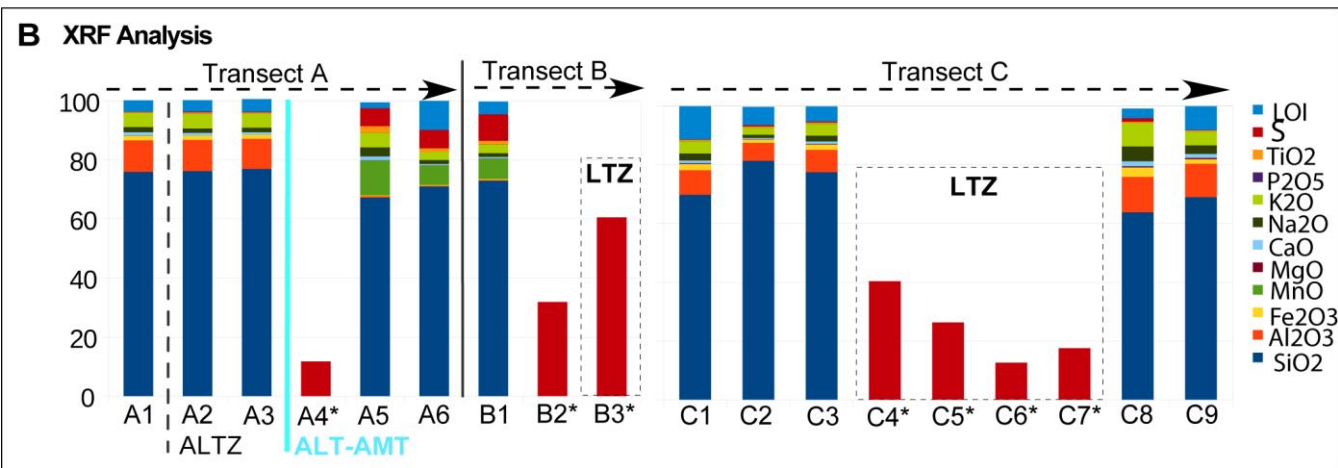
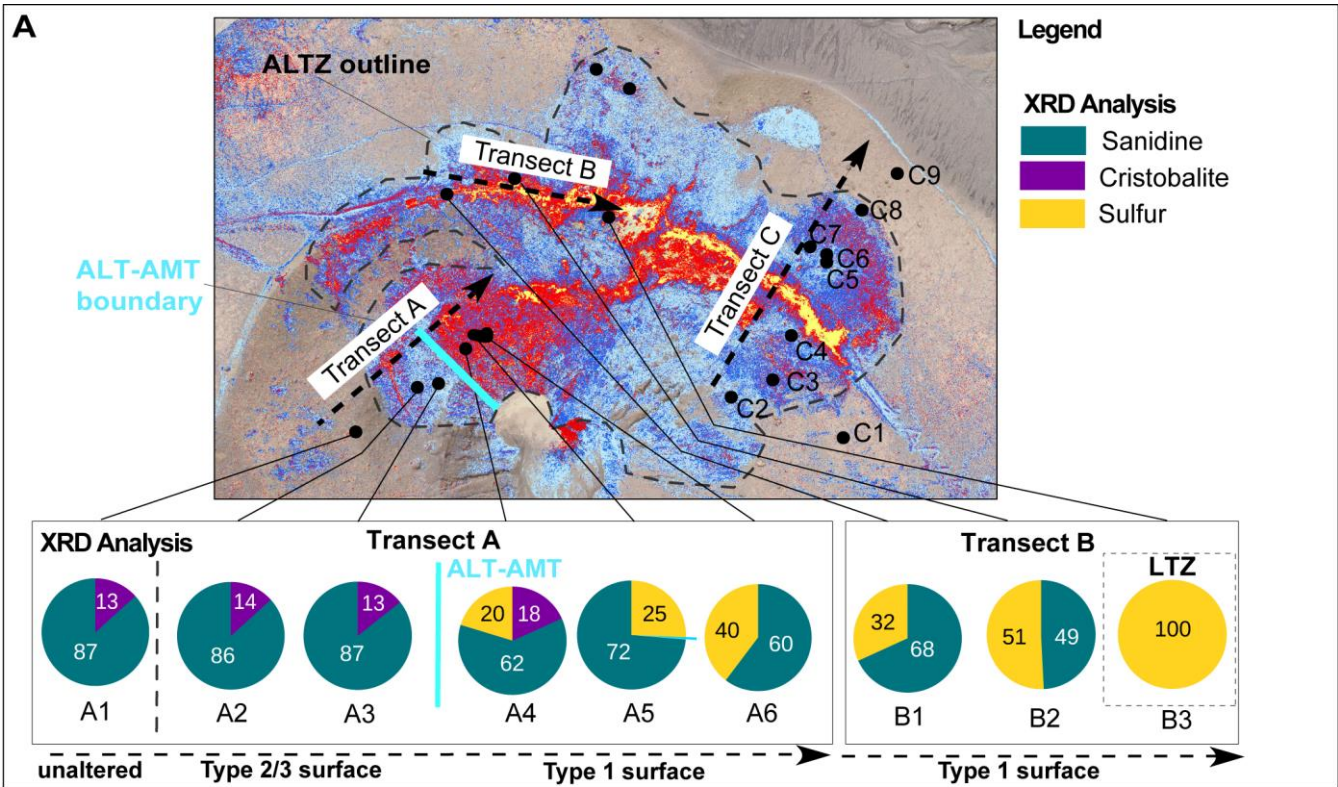


Figure 6: A/B) Spatial distribution and flux values for  $\text{CO}_2$  (red bars in A),  $\text{SO}_2$  (light blue bars in B), and  $\text{SO}_2/\text{H}_2\text{S}$  (turquoise bars in B) in a map view- for 200 measurement points. Each bar represents a relative flux value at a measurement location. In case no flux was detectable, the respective location is marked with a black dot only. The dashed line highlights the ALTZ (Alteration Zone) boundary. Dark grey features in the background highlight the thermally active surface (compare Figure 2D). Labels F0, F5AT, F11, and FA mark prominent high-temperature fumaroles. The labels a-g mark notable large-scale anomaly units. C/D) Flux values within or outside the ALTZ are plotted by distance to the ALTZ boundary- (dashed line). Measurement

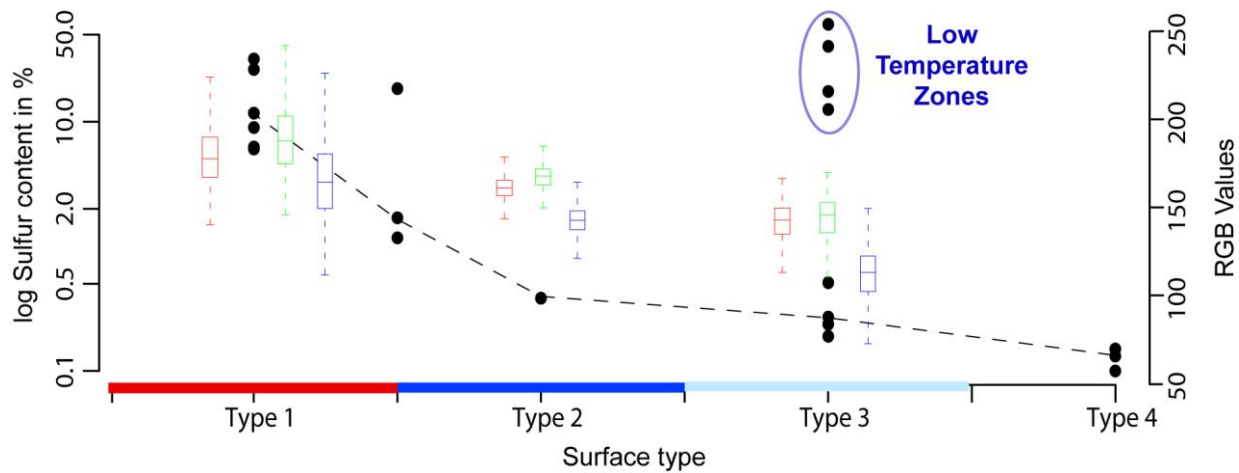




For  
bor  
bor  
For  
For

1717 Figure 7: Mineral and bulk chemical composition of rock samples along 3 transects A-C<sub>2</sub> crosscutting alteration gradients, and  
 1718 structural units. A) Overview map with defined surface types 1-4, highlighting the area with visible optical changes at the  
 1719 surface, referred to as ALTZ (Alteration Zone, marked by a dashed line). The three transects A-C were placed so that they  
 1720 crosscut prominent units. Mineralogical compositions from XRD (X-ray diffraction) are depicted by circular plots at the  
 1721 bottom of Fig. A. B) Bulk chemical composition from XRF (X-ray fluorescence) analysis of transects A-C. Transect A/B)  
 1722 With increasing alteration intensity we observe a relative decrease of the initial mineral phases sanidine and cristobalite  
 1723 whereas the sulfur content increases. Note that the mineral composition in this figure is normalized to 100 % non-amorphous  
 1724 minerals. In the chemical composition, we observe a significant decrease of Al<sub>2</sub>O<sub>3</sub> and Fe<sub>2</sub>O<sub>3</sub> but an increase of MnO, TiO<sub>2</sub>,  
 1725 and S with increasing alteration, especially at the ALT-AMFTType3-Type1 (T3-T1) boundary. At marked in light blue. For  
 1726 transect C we observe a dominant increase of S (17- - 40% %) for samples taken within the LTZ. Else than observed for the  
 1727 (low-temperature zone). Compared to other transects, changes in Al<sub>2</sub>O<sub>3</sub>, Fe<sub>2</sub>O<sub>3</sub>, TiO<sub>2</sub>, and MnO are less significant, even in  
 1728 the active units a and b. For samples marked with an asterisk (\*) ~~XRF~~ XRF results are not available. No XRD results are available  
 1729 for transect C.

1730



1731

1732

1733

1734

1735

1736

1737

1738

1739

1740

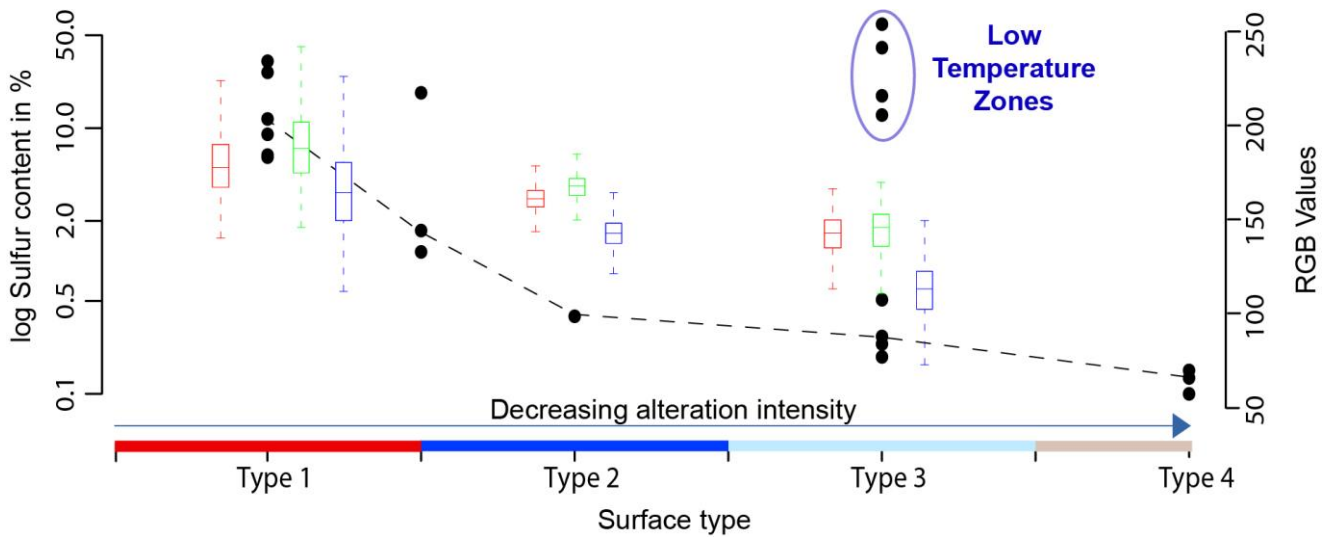
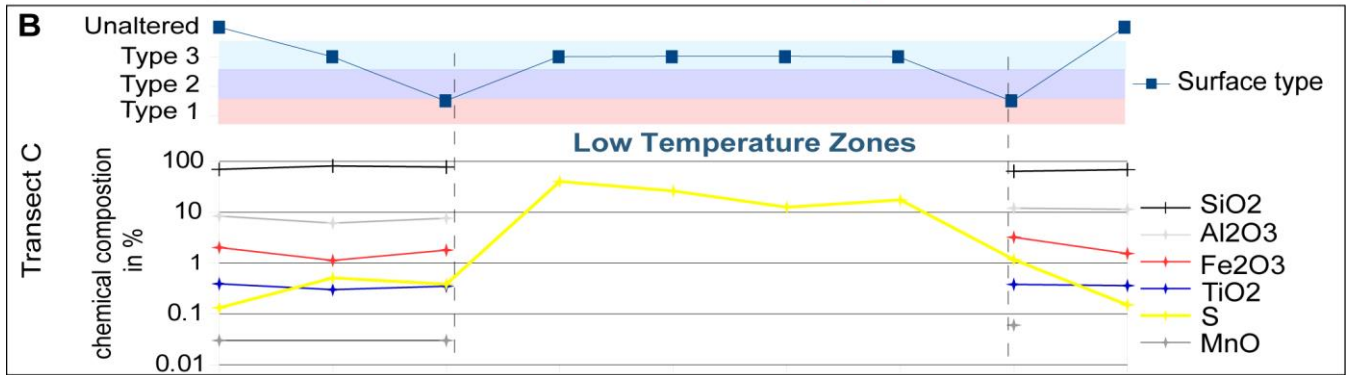
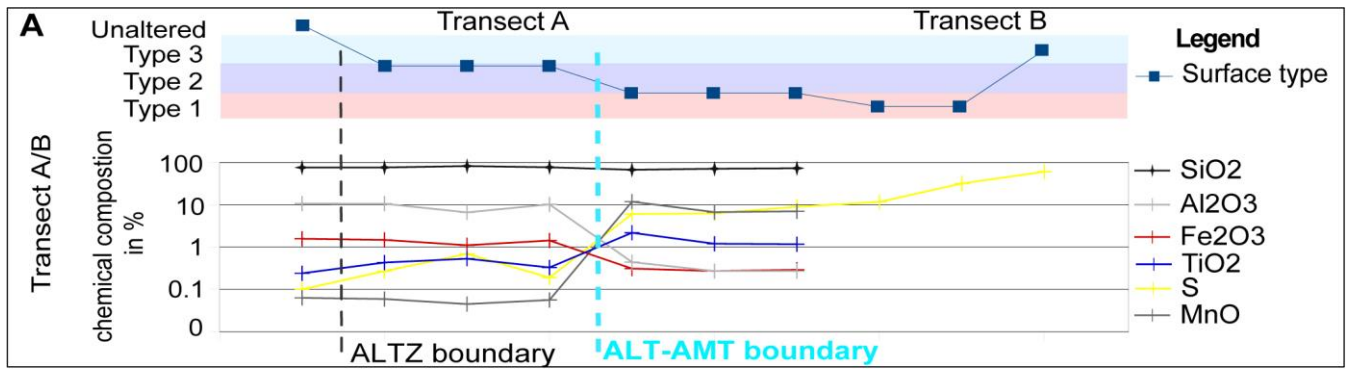
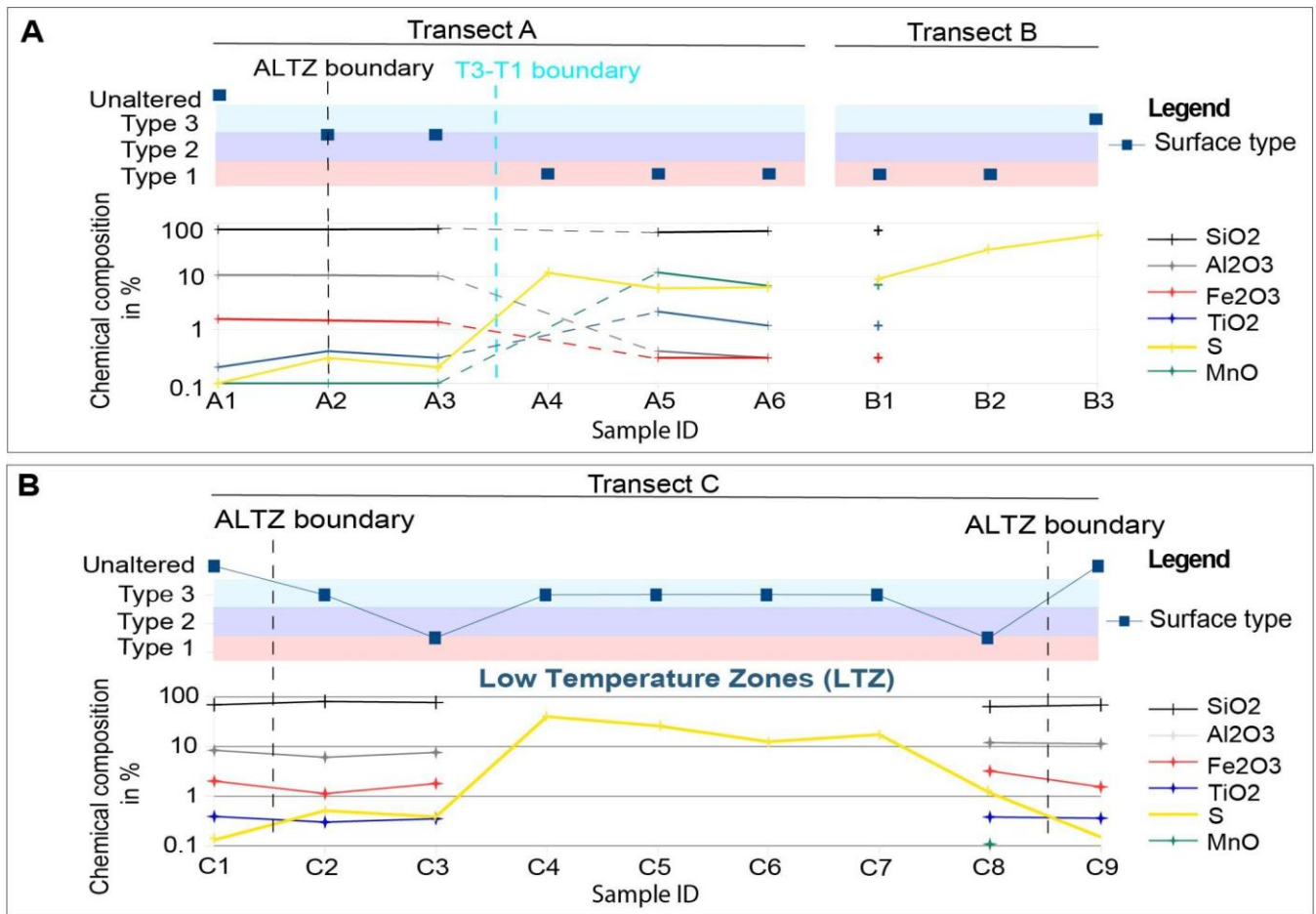


Figure 8: OverviewRelation of the relation of inferred surface type (T1-4) and sulfur content of rock samples and brightness or inferred taken in the respective surface Type T1-4. Black dots mark the sulfur contents of rock samples, and are shown on a log scale versus the color-coded box-plots the respective value range in the RGB-values. surface type from which the sample was taken, labeled by Type 1-4 on the x-axis and demarked with boxes using the same color code as throughout the manuscript. With decreasing alteration from Type 1, surface Type from highest altered (to Type 1) to unaltered (Type 4), the measured sulfur contents 4 surface we see a significant decrease of sulfur content from up to 100 % for Type 1 to < 1 % for Type 4 surface. The black dashed line illustrates this. An exemption is the Type 3 surface, where we observe two distinct clusters, one with low S-sulfur values and one with extraordinarily high S-values. These high sulfur values belong to samples taken in the LTZ (low-temperature zones), which separate fumaroles from the larger diffuse active units a and b (compare Figure 4) for instance. These samples indicate that LTZ represent sulfur-rich crusts that block heat and gas flux from the surface. The colored boxplots show the distribution of RGB values for the respective surface Type 1-4, showing a similar trend of decreasing values. Red boxplots represent the red value, blue and green the respective blue and green channel values of the image. The coincidence between both indicates a direct relation or control of sulfur onto the surface colorization.



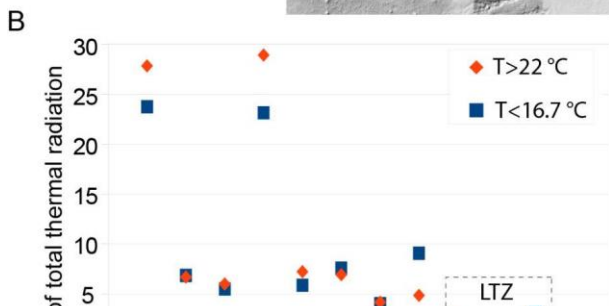
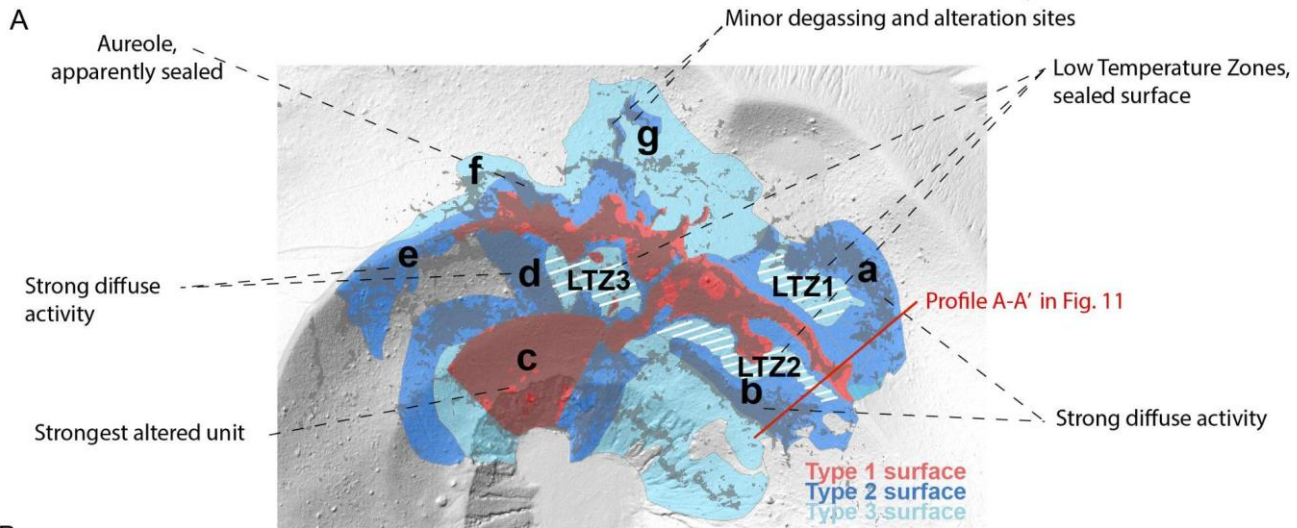
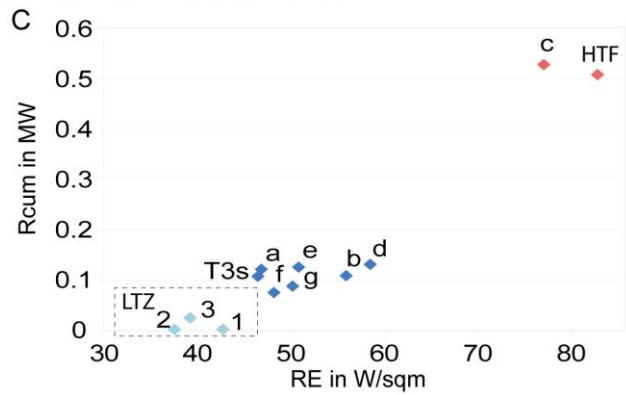
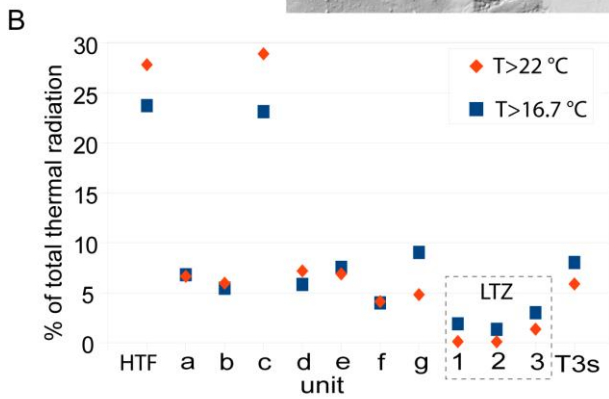
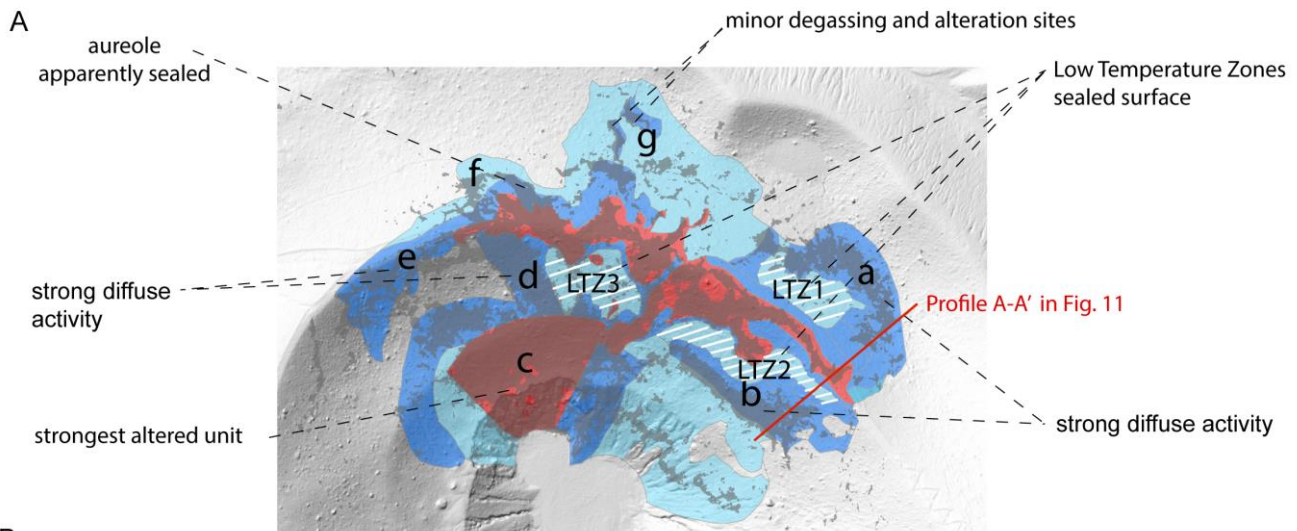
1774

For  
bor  
bor  
For  
For



1784

1785 Figure 9: ~~Geochemical changes~~Changes of surface type and bulk-chemical composition observed along ~~transect~~transects A-,  
 1786 B, and C. Locations for the transects and sample ID are shown in Figure 7. A) With increasing alteration from Type 4 to Type  
 1787 1 surface we observe a reduction of  $\text{Fe}_2\text{O}_3$  and  $\text{Al}_2\text{O}_3$  and an increase in S. ~~Strongest~~Sulfur. While changes observed at the  
 1788 ALTZ boundary (black dashed line) are only minor, strong changes are observed at the ~~ALT-AMT boundary~~-Type 3-Type 1  
 1789 boundary (T3-T1, blue dashed line). Sulfur contents in transect B were so high that XRF results were only available for sample  
 1790 B1. B) Changes observed in the eastern fumarole field along transect C are less significant, with the exception of  
 1791 ~~extraordinary~~extraordinarily high sulfur content for Type 3 samples, ~~which represent~~ collected in the LTZ.  
 1792

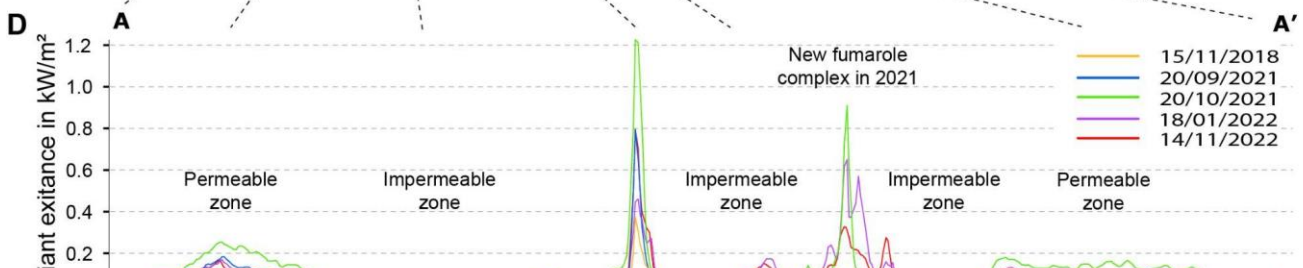
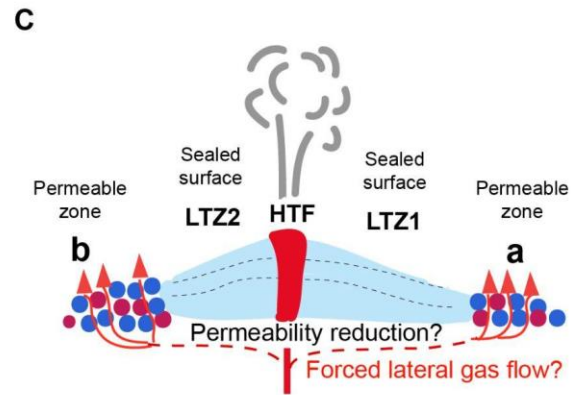
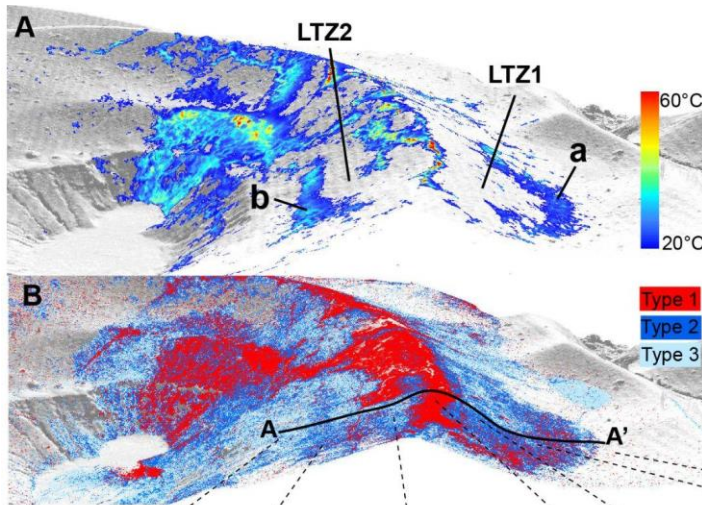
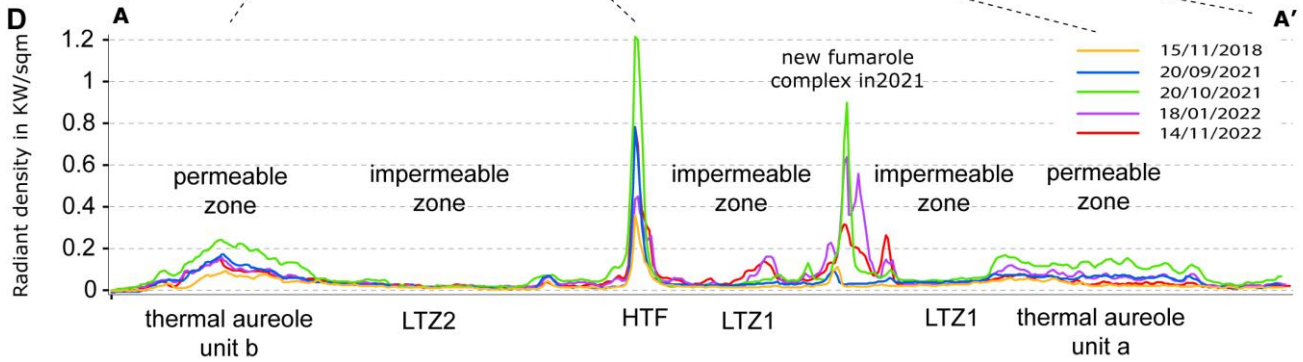
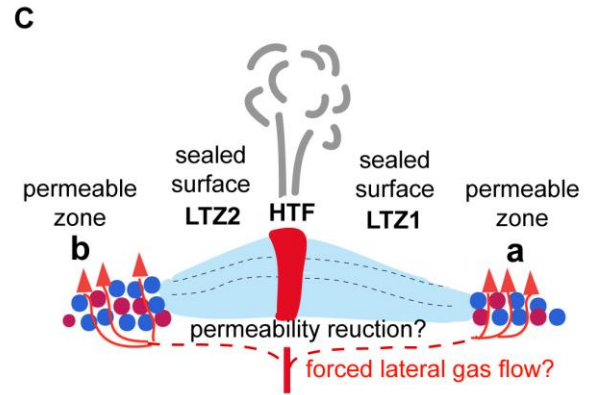
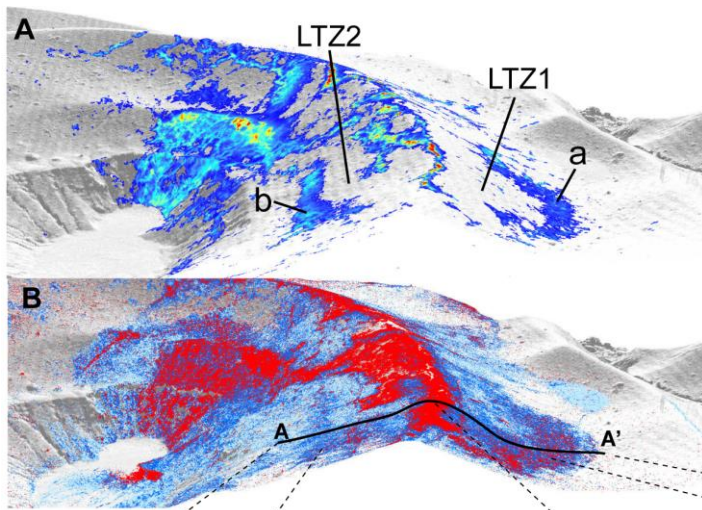


For  
bor  
bor  
For  
For

1806 Figure 10: Anatomy of the fumarole field. A) Simplified structure of the fumarole field highlighting surface types and  
1807 structural units of increased diffuse activity (a-g) or areas of apparent surface sealing (~~LTZ~~LTZ1-3 marked by white lines). B)  
1808 Contribution to the total thermal radiation in % ~~to the total radiation~~ for ~~anomalies~~HTF (high-temperature fumaroles), units a-  
1809 g, and LTZ1-3 (low-temperature zones) considering pixels with  $T > < 22^{\circ}\text{C}$  (blue) and for identified units based on a spatial  
1810 constraint, ~~also including and pixel~~ temperatures  $\Leftrightarrow 22^{\circ}\text{C}$ : (orange). C) Radiant exitance (RE) in  $\text{W}/\text{m}^2$  and cumulative  
1811 radiation (Rcum) in MW. Rcum is the cumulated background corrected radiant exitance (Equation 2 in the method section) of  
1812 all pixels associated with the respective active unit. Note that for ~~RC and contribution to the total thermal radiation~~Rcum only  
1813 ~~anomalies~~pixels with  $T > > 22^{\circ}\text{C}$  were used. We can clearly distinguish different thermal regimes that are also coincident with  
1814 surface types identified in the optical data.

1815

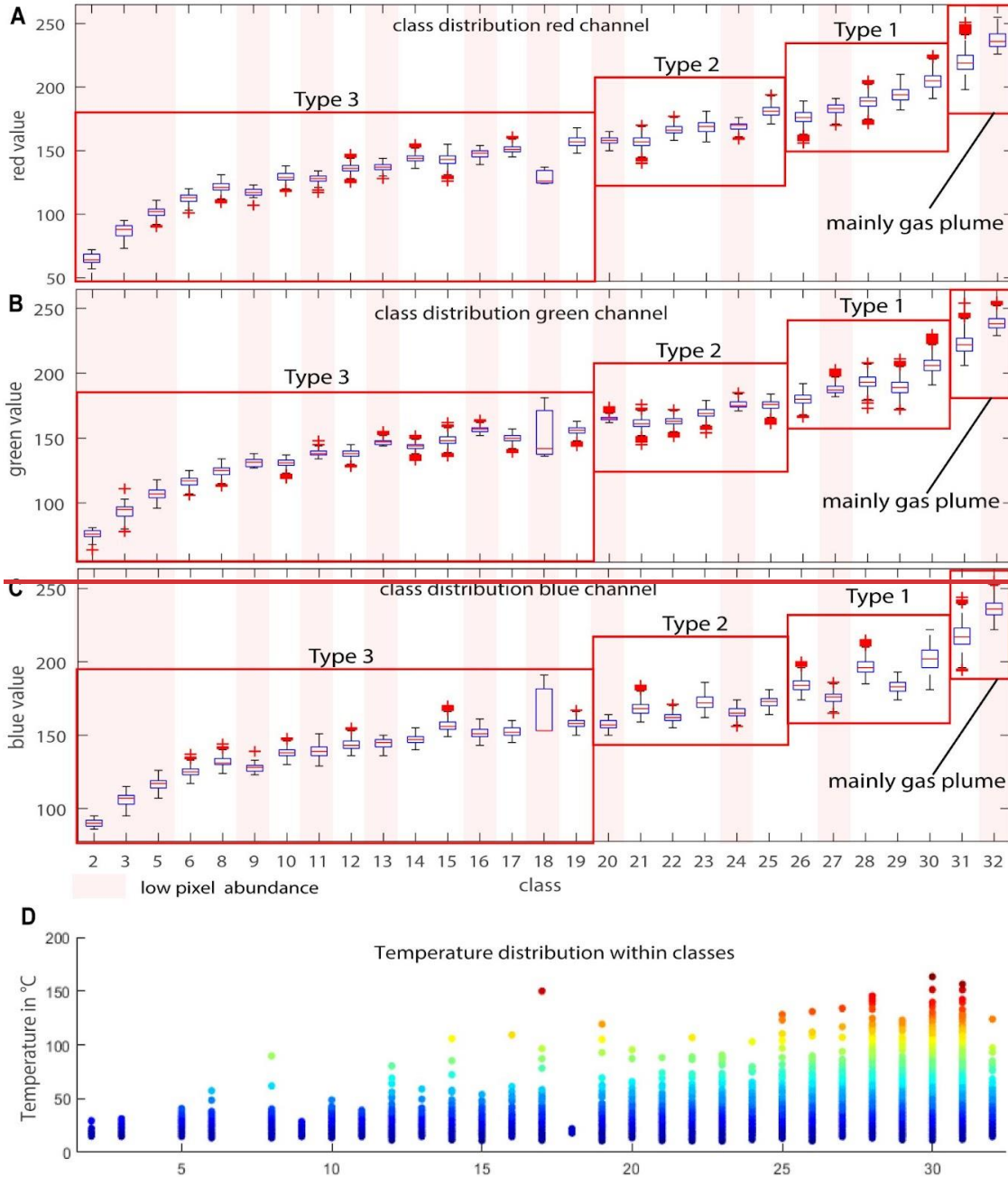
1816



For  
bor  
bor  
For  
For

1832 Figure 11: ~~Crossection~~Cross Section of the eastern fumarole field along Profile A-A' (Fig.10) highlighting the structural setup  
1833 from high-temperature fumaroles in the center to LTZ and diffuse aureoles at a distance. A) Thermal structure along the cross-  
1834 section. B) Alteration structure along the cross-section. C) Schematic sketch along cross-section A-A', highlighting the  
1835 central LTZ that might be controlled by surface sealing processes or deeper effects of permeability reduction in the vicinity to  
1836 the high-temperature fumaroles due to long-term gas-rock interaction and alteration processes. D) Evolution of thermal  
1837 radiation values during a volcanic crisis. While thermal radiation at fumaroles and aureoles increased, radiation values of LTZ  
1838 ~~remain~~remained unchanged, therefore highlighting the efficiency of surface sealing.

1839  
1840  
1841  
1842  
1843  
1844



For  
bor  
bor  
For  
For

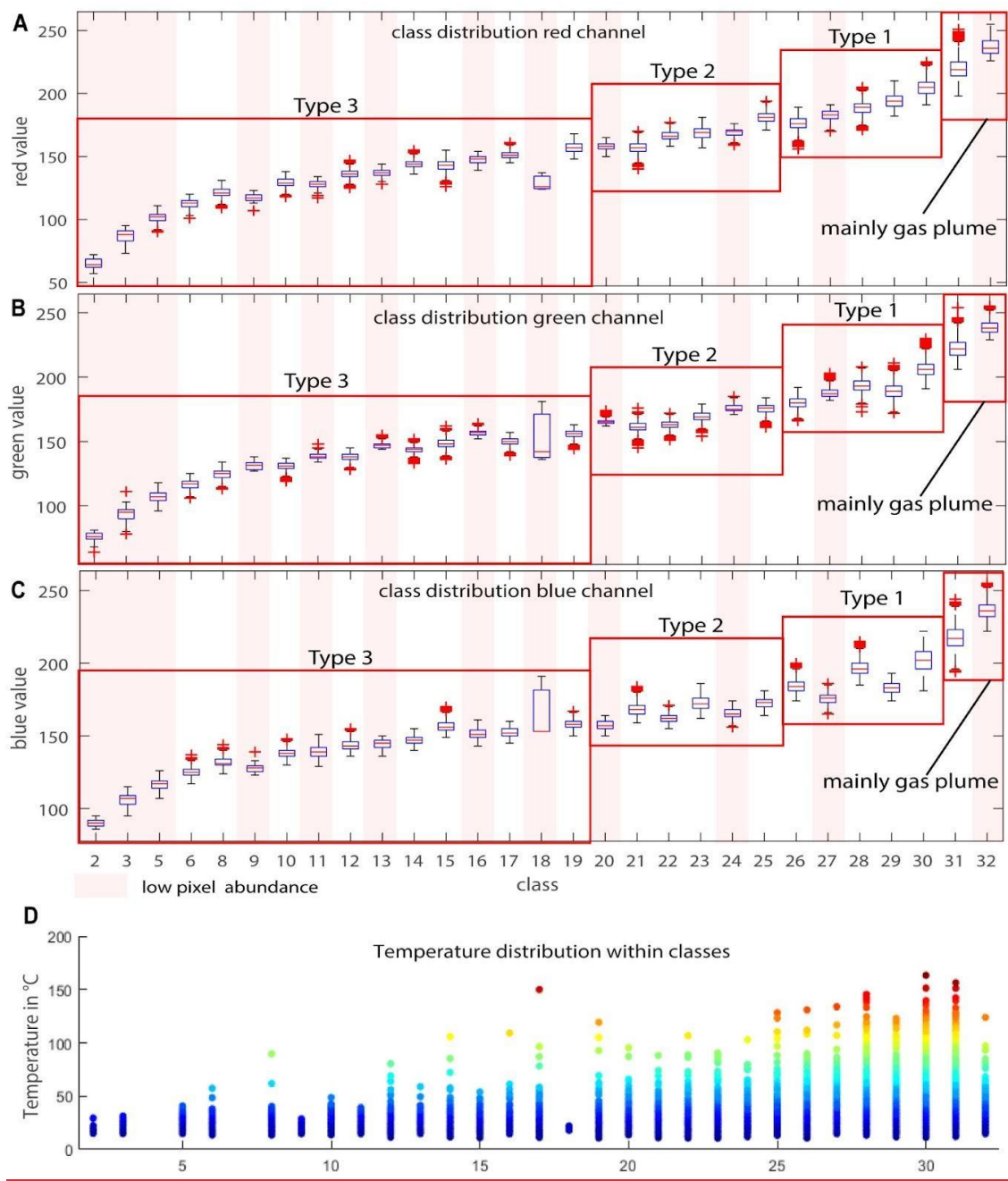


Figure A1: Boxplots of RGB value distribution for the defined surface Types 1-3. Classes (unsupervised classification 32 classes) marked with the transparent red bar only have minor pixel abundances. Red boxes depict the spectral range of Type 1-3 surfaces. Class 31 and 32 are mainly associated with the fumarole steam plume.

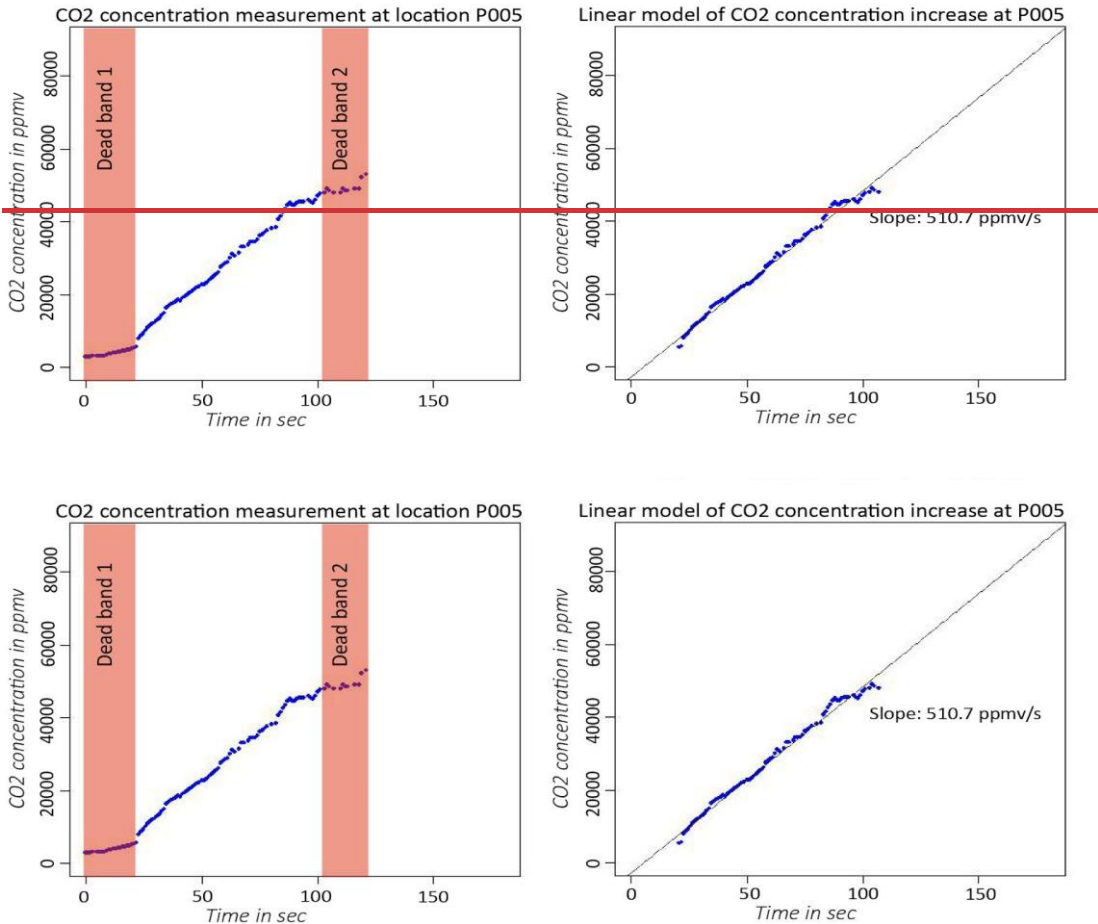
1857  
1858  
1859  
1860  
1861  
1862

For  
For  
Mul  
bor  
bor  
For  
For  
bor  
bor  
For

1877

1878

### Appendix B: Gas measurement procedure - simplified accumulation chamber approach



1879

1880

1881

1882

1883

1884

1885

Figure B1: CO<sub>2</sub> measurement at location P005, here shown representative for all measurement points. Dead bands at the beginning and end of the measurement were removed and the intensity of gas flux was characterized by linear regression through the constantly ascending part of the graph. The slopes of the linear model allow a relative comparison of single measurement points.

1886

1887

1888

1889

1890

To compare the observations from remote sensing to present-day surface degassing, measurement campaigns were performed in September 2021 and November 2022. The surface degassing was measured at 200 points within the northern part of the la fossa cone (Figure 6 in the main manuscript), in a simplified multi-gas accumulation chamber approach. The simplified accumulation chamber consists of the measurement unit, a Dräger Xam 8000, coupled to a 10.3 cm diameter and 16.5 cm long plastic chamber by a 116 cm long tube with an inner diameter of 0.5 cm, resembling a simplified

1933 accumulation chamber. The plastic chamber has a volume of 1374.8 cm<sup>3</sup>, and the tube has a volume of 91.1 cm<sup>3</sup> so that the  
1934 total system volume is 1465.934 cm<sup>3</sup>. The pumping rate is 0.351 per minute. The plastic chamber was equipped with an open  
1935 valve which was a necessity as the Dräger is an actively pumping system. Therefore, concentration increases in the chamber  
1936 can be considered as surface flow and as independent from pumping effects. The Measurement unit is protected by a preceding  
1937 2µm filter, preventing dust and vapor ~~to enter from entering~~ the unit. Note that we use Flux values in this study only for relative  
1938 comparison and detection of the spatial variability of certain gas species and flows. A precise flux estimate is beyond the scope  
1939 of this publication and can not be constrained as we did not measure gas temperatures and humidity at sampling locations. ▲  
1940 The measurement unit, a Dräger XAM 8000 handheld Multigas device was equipped with 6 sensors measuring CO<sub>2</sub>, CH<sub>4</sub>,  
1941 SO<sub>2</sub>, H<sub>2</sub>S, H<sub>2</sub>, and O<sub>2</sub> simultaneously. The relevant species for this work are CO<sub>2</sub>, SO<sub>2</sub>, and H<sub>2</sub>S, therefore only these will be  
1942 considered in detail. The CO<sub>2</sub> sensor is a Non-Dispersive Infrared (NDIR) sensor. NDIR sensors use the absorption  
1943 characteristics of CO<sub>2</sub> at ~ 4 µm, which leads to a concentration-dependent amplitude loss of the internally emitted IR light.  
1944 The sensor has a detection threshold of 0.01 vol% CO<sub>2</sub> and is calibrated for measuring CO<sub>2</sub> in a range of 0-5 vol % at a  
1945 resolution of 50 ppm under normal ( -20-50 °C, 10-95 % RH, and 700-1300 hPa) atmospheric conditions. The response rate is  
1946 < 10 sec for reaching T50- and < 15 sec for reaching T90 concentrations. The H<sub>2</sub>S sensor is an electrochemical sensor with a  
1947 detection limit of 0.4 ppm and a resolution of 0.1 ppm, measuring in a range of 0-100 ppm H<sub>2</sub>S under normal atmospheric  
1948 conditions. The response time for T90 values is >15 seconds and the accuracy of the measurement is +-5 % of the measured  
1949 value. The SO<sub>2</sub> sensor is an electrochemical sensor with a detection limit of 0.1 ppm and a resolution of 0.1 ppm, measuring  
1950 as well in a range of 0-100 ppm under atmospheric conditions. The response time for T90 values is < 15 seconds and the  
1951 accuracy of the measurement is 2 % of the measured value. The NDIR CO<sub>2</sub> sensor is robust against cross-sensitivities.  
1952 However, electrochemical sensors can be vulnerable to cross sensitivities (SO<sub>2</sub>, H<sub>2</sub>S, Cl<sub>2</sub> ), resulting in uncertainties of the  
1953 measurement of a few percent of the measurement value. ▲  
1954 The approach of combining the Dräger multigas with an accumulation chamber was developed and adapted as a consequence  
1955 of uncertainties encountered in previous campaigns. The different sensors have slightly different reaction times for ascending  
1956 gas concentrations and significantly different reaction times for descending gas concentrations. Comparing sensor readings  
1957 directly therefore might lead to odd gas ratios. For that reason instead of the direct gas readings, we use the slope of the  
1958 ascending gas concentration within the accumulation chamber to produce more reliable estimates of the surface flow.  
1959 For a relative comparison of degassing rates of the single measurement points, the gas data was plotted and the representative  
1960 part of the graph, resembling a constantly ascending slope, was used to calculate the concentration increase by linear regression.  
1961 Data points of the “Dead Bands” at the beginning and end of each graph were removed. In this way, we achieve a relative gas  
1962 flux from soil that allows us to analyze spatial variations of gas flux throughout the study area. An overview of all gas  
1963 measurement points will be given in Figure 6. The aim of the gas measurements was not to provide accurate flux estimates but  
1964 to highlight and quantify the spatial variability of the surface flux of certain gas species. ▲  
1965 Each measurement was performed under similar conditions. Locations were selected in a way that they represent similar  
1966 surface conditions, considering a spatial distance to fumarolic vents and an unsealed surface, for instance. Measurement  
1967 locations typically were small areas with a naturally “open surface”, often embedded in broader areas of the sealed surface.  
1968 Such spots typically can be identified by loose gravel on the surface and in case slightly different coloration. For the  
1969 measurement, the surface was cleaned and gravel was removed to provide a flat contact surface. Then the measurement was  
1970 started, and the plastic chamber was placed on the ground and sealed on the bottom with fine-grained material. The average  
1971 measurement duration was 2 min. In case of very rapidly ascending SO<sub>2</sub> or H<sub>2</sub>S gas concentrations, the chamber was removed  
1972 from the ground before and the system was flooded with fresh air, to protect the sensors from critically high acid  
1973 concentrations. This procedure was chosen to ensure a fresh air flooded chamber at the beginning of each measurement and to  
1974 record the initial atmospheric gas concentration. Further, it allows better identification of the measurement start- and end-

1981 points within the respective data sets, as each data series has two dead bands, one at the beginning and one at the end. Figure  
1982 B1 shows a typical graph of a CO<sub>2</sub> measurement, with the Dead-Band at the beginning and end of each measurement and the  
1983 constant ascending graph, representing the gas concentration increase within the chamber. The “Dead Bands” represent parts  
1984 of the measurement where the accumulation chamber was placed on the ground but not sealed yet, or removed from the soil  
1985 at the end of the measurements. Dead Bands at the beginning of the measurement were typically on the order of 20- 30 s.

1986

For

For

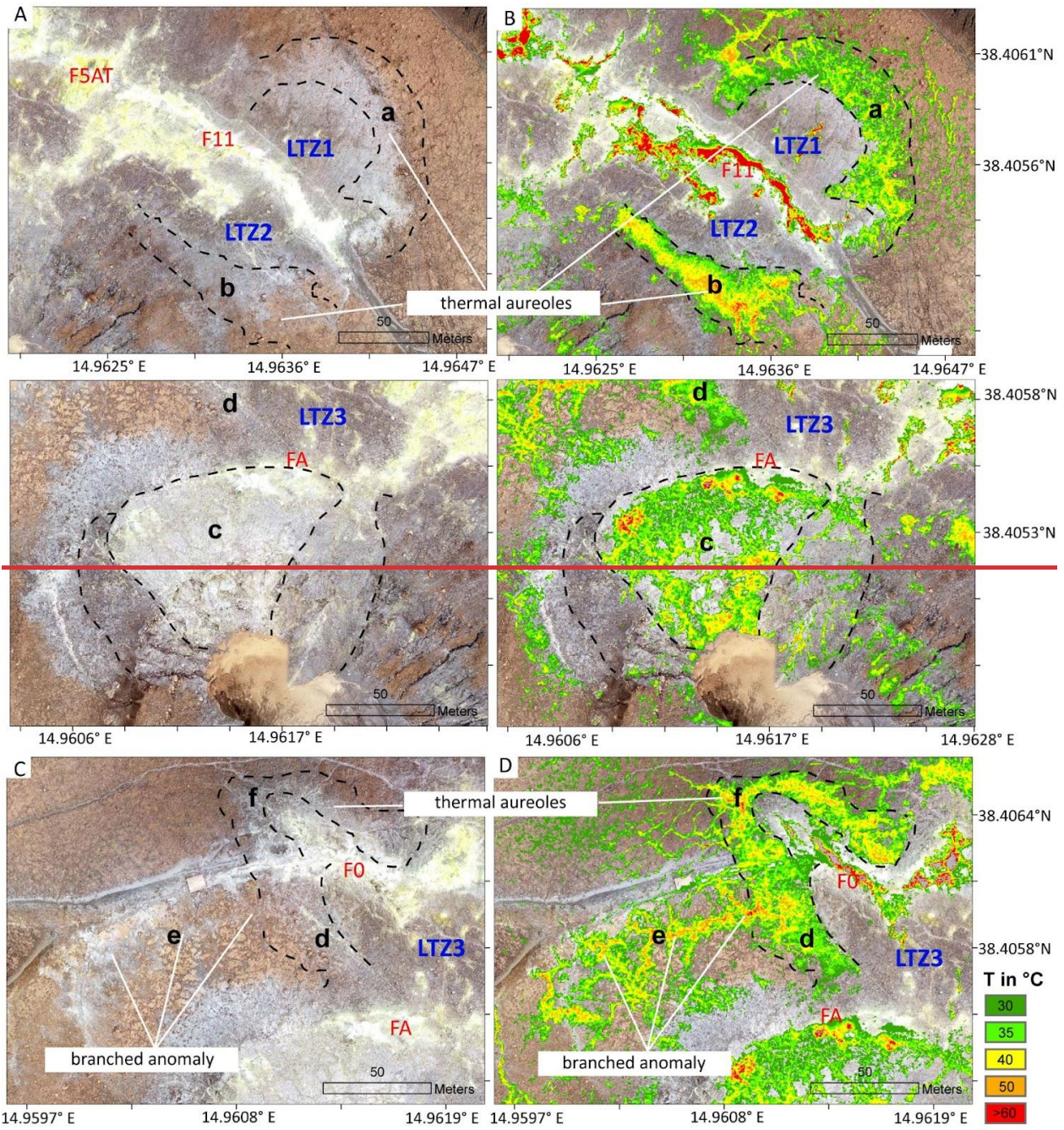
For

bor

bor

For

Appendix C: Detail views on identified units



For  
bor  
bor  
For  
For

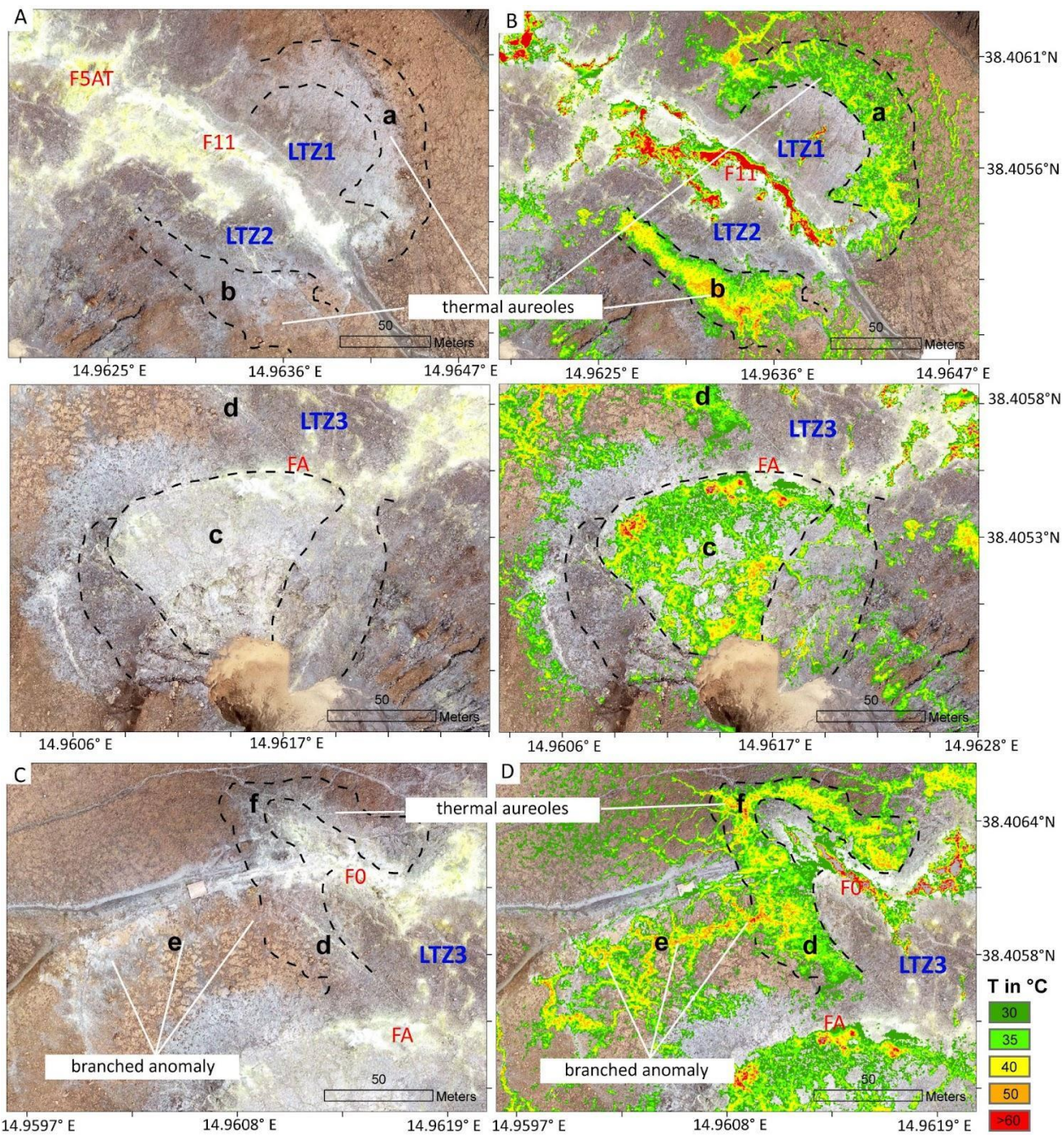


Figure C1: Detail views of distinct units a-f and LTZ1-3 in a true color representation as seen from our 2019 orthomosaic data and an overlay by the thermal data with  $T \geq 30^{\circ}\text{C}$ . A/B) Shown are units 1 and b and respective LTZ1 and 2. Note the outward spatial offset of both thermal units with respect to the surface coloration. C/D) Unit c is characterized by a network of thermal anomalies embedded in the colder surroundings. E/F) Thermal aureole d and f branched anomaly e.

Also here an outward shift of the thermal feature with respect to the surface coloration ~~osis~~ observed, ~~that~~which could indicate gradual sealing processes with proximity to the main vents.

#### Appendix D: Spearman correlation test for non-normal distributed variables

The test for correlation between optical and thermal anomalies was performed using the ggpubr package (Kassambara, 2019) in the statistical software environment R. The method used was Spearman's rank correlation which is suggested to be used for non-normal distributed data. The correlation test is based on the vectorized classification raster data set (classp\_fumclip) with 8,890,830 data points with the analyzed variables pixel class (0-32) and pixel temperature (20- 150°C). The results show a correlation factor of 0.3485299, which is considered a mean positive correlation, and a p-value of 2.2e-16 proves statistical significance.

Spearman's rank correlation rho

data: x and y

S = 7.6277e+19, p-value < 2.2e-16

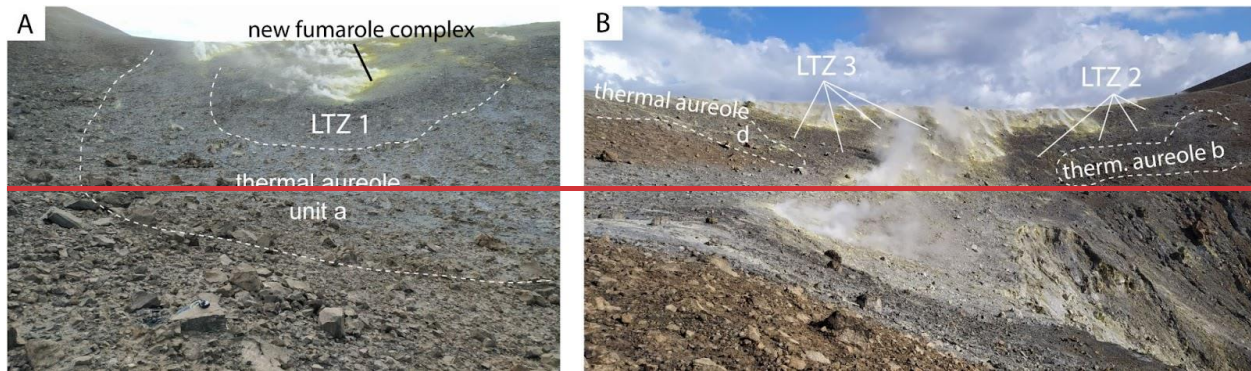
alternative hypothesis: true rho is not equal to 0

sample estimates:

rho

0.3485299

#### Appendix E: Thermal aureoles and LTZ indicated in field photographs



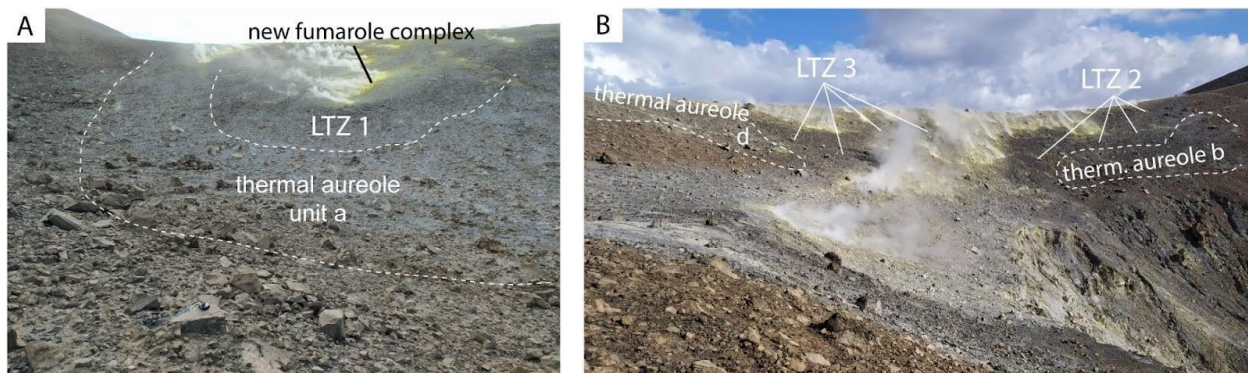


Figure E1: Thermal aureoles and low-temperature zones (LTZ) depicted on field photographs. A) Thermal aureole a and LTZ1. B) Thermal aureole b and d with LTZ2 and LTZ3.

### Appendix F:

Table F1: XRD results of samples taken along transect A and B

Sample ID	A1	A2	A3	A4	A5	A6	B1	B2	B3
Sanidine	86.7	85.7	87.4	61.5	72.2	60.3	68.2	49.2	0
Cristobalite	13.3	14.3	12.6	18.2	0	0	0	0	0
Coesite	0	0	0	0	0.7	0	0	0	0
Sulfur	0	0	0	20.3	25.1	39.7	31.8	50.8	100
amorphous	50	0	0	0	0	50	50	0	0

### Appendix G: XRF results of samples taken along transects A-C.

Table G1: XRF results of samples taken along transects A-C. Note that samples with  $s > S > 10\%$  were not analyzed by XRF.

S-ID	SiO <sub>2</sub> (%)	TiO <sub>2</sub> (%)	Al <sub>2</sub> O <sub>3</sub> (%)	Fe <sub>2</sub> O <sub>3</sub> (%)	MnO (%)	MgO (%)	CaO (%)	Na <sub>2</sub> O (%)	K <sub>2</sub> O (%)	P <sub>2</sub> O <sub>5</sub> (%)	LOI (%)	S Eltra (%)
A1	76.0	0.2	10.7	1.6	0.1	0.1	1.1	1.8	4.8	0.1	3.8	0.1



2121 performed XRD analysis, and supervised the writing. J.S. performed XRF analysis and supported the writing. A.K. performed  
2122 XRD analysis and supported the writing. E.D.P. collected data and samples, supported all field works and the writing of this  
2123 manuscript. A.F.P. supported fieldwork and on the ground logistics, acquired data, and supported the writing. M.Z. supported  
2124 the gas measurement campaign and supported the writing. B.D.J. supported the fieldwork and writing of this manuscript.  
2125

## 2126 12 Competing interests

2127 The authors declare that they have no conflict of interest.

## 2128 13 Acknowledgements

2129 We are grateful for the financial and material support provided to realize this study. This work is contributing to the focus  
2130 ~~site~~ Etna and was financially supported by GFZ Potsdam. Financial support to realize this study was also provided by  
2131 DAAD research grant Nr. 57556282. ~~We~~ and by ERC project 'ROTTnROCK\*', a research project funded by the European  
2132 Research Council under the European Union's Horizon Europe Programme / ERC synergy grant n. [ERC-2023-SyG  
2133 101118491]. We furthermore thank INGV Palermo for collaboration and ~~their~~ support, especially during the 2021 crisis,  
2134 without which parts of this study could not have been realized. ~~Further we want to acknowledge the Swedish Research~~  
2135 ~~Council.~~

## 2136 14 References

- 2137 Abdi, H., & Williams, L. J. (2010). Principal component analysis. Wiley interdisciplinary reviews: computational statistics,  
2138 2(4), 433-459. <https://doi.org/10.1002/wics.101>
- 2139
- 2140 Aiuppa, A., Federico, C., Giudice, G., & Gurrieri, S. (2005). Chemical mapping of a fumarolic field: La Fossa crater, Vulcano  
2141 Island (Aeolian Islands, Italy). *Geophysical Research Letters*, 32(13). <https://doi.org/10.1029/2005GL023207>
- 2142
- 2143 Alexandris, N., Gupta, S., & Koutsias, N. (2017). Remote sensing of burned areas via PCA, Part 1: centering, scaling and EVD  
2144 vs SVD. *Open geospatial data, software and standards*, 2, 1-11. <https://doi.org/10.1186/s40965-017-0028-1>
- 2145
- 2146 Azzarini, F. M., Pareschi, M. T., Sbrana, A., Favalli, M., & Fulignati, P. (2001). Surface hydrothermal alteration mapping at  
2147 Vulcano Island using MIVIS data. *International Journal of Remote Sensing*, 22(11), 2045-2070.  
2148 <https://doi.org/10.1080/01431160118291>
- 2149
- 2150 Ball, M. and Pinkerton, H., 2006. Factors affecting the accuracy of thermal imaging cameras in volcanology. *Journal of*  
2151 *Geophysical Research: Solid Earth*, 111(B11). <https://doi.org/10.1029/2005JB003829>
- 2152

- 2194 Barreca, G., Bruno, V., Cultrera, F., Mattia, M., Monaco, C., & Scarfi, L. (2014). New insights in the geodynamics of the  
2195 Lipari–Vulcano area (Aeolian Archipelago, southern Italy) from geological, geodetic and seismological data. *Journal of*  
2196 *Geodynamics*, 82, 150-167. <https://doi.org/10.1016/j.jog.2014.07.003>
- 2197  
2198 Berg, S. E., Troll, V. R., Harris, C., Deegan, F. M., Riisshuus, M. S., Burchardt, S., & Krumbholz, M. (2018). Exceptionally  
2199 high whole-rock  $\delta^{18}\text{O}$  values in intra-caldera rhyolites from Northeast Iceland. *Mineralogical Magazine*, 82(5), 1147-1168.  
2200 <https://doi.org/10.1180/mgm.2018.114>
- 2201  
2202 BILLI, Andrea, et al. Tectonics and seismicity of the Tindari Fault System, southern Italy: Crustal deformations at the transition  
2203 between ongoing contractional and extensional domains located above the edge of a subducting slab. *Tectonics*, 2006, 25. Jg.,  
2204 Nr. 2. <https://doi.org/10.1029/2004TC001763>
- 2205  
2206 Bolognesi, L., & D'Amore, F. (1993). Isotopic variation of the hydrothermal system on Vulcano Island, Italy. *Geochimica et*  
2207 *Cosmochimica Acta*, 57(9), 2069-2082.  
2208 [https://doi.org/10.1016/0016-7037\(93\)90094-D](https://doi.org/10.1016/0016-7037(93)90094-D)
- 2209  
2210 Boyce, A. J., Fulignati, P., Sbrana, A., & Fallick, A. E. (2007). Fluids in early stage hydrothermal alteration of high-sulfidation  
2211 epithermal systems: A view from the Vulcano active hydrothermal system (Aeolian Island, Italy). *Journal of Volcanology and*  
2212 *Geothermal Research*, 166(2), 76-90.  
2213 <https://doi.org/10.1016/j.jvolgeores.2007.07.005>
- 2214  
2215 Bukumirovic, T., Italiano, F., & Nuccio, P. M. (1997). The evolution of a dynamic geological system: the support of a GIS for  
2216 geochemical measurements at the fumarole field of Vulcano, Italy. *Journal of volcanology and geothermal research*, 79(3-4),  
2217 253-263. [https://doi.org/10.1016/S0377-0273\(97\)00032-2](https://doi.org/10.1016/S0377-0273(97)00032-2)
- 2218  
2219 Capasso, G., Favara, R., Inguaggiato, S., 1997. Chemical features and isotopic composition of gaseous manifestations on  
2220 Vulcano Island, Aeolian Islands, Italy: an interpretative model of fluid circulation. *Geochim. Cosmochim. Acta* 61, 3425–  
2221 3440 [https://doi.org/10.1016/S0016-7037\(97\)00163-4](https://doi.org/10.1016/S0016-7037(97)00163-4)
- 2222  
2223 Capasso, G., Favara, R., & Inguaggiato, S. (2000). Interaction between fumarolic gases and thermal groundwaters at Vulcano  
2224 Island (Italy): evidences from chemical composition of dissolved gases in waters. *Journal of volcanology and geothermal*  
2225 *research*, 102(3-4), 309-318.  
2226 [https://doi.org/10.1016/S0377-0273\(00\)00193-1](https://doi.org/10.1016/S0377-0273(00)00193-1)
- 2227  
2228 Capasso, G., Federico, C., Madonia, P., & Paonita, A. (2014). Response of the shallow aquifer of the volcano-hydrothermal  
2229 system during the recent crises at Vulcano Island (Aeolian Archipelago, Italy). *Journal of volcanology and geothermal*  
2230 *research*, 273, 70-80. <https://doi.org/10.1016/j.jvolgeores.2014.01.005>
- 2231  
2232 Carapezza, M. L., Barberi, F., Ranaldi, M., Ricci, T., Tarchini, L., Barrancos, J., ... & Gattuso, A. (2011). Diffuse CO<sub>2</sub> soil  
2233 degassing and CO<sub>2</sub> and H<sub>2</sub>S concentrations in air and related hazards at Vulcano Island (Aeolian arc, Italy). *Journal of*  
2234 *Volcanology and Geothermal Research*, 207(3-4), 130-144. <https://doi.org/10.1016/j.jvolgeores.2011.06.010>

- 2275 Carranza, E. J. M., & Hale, M. (2002). Mineral imaging with Landsat Thematic Mapper data for hydrothermal alteration  
2276 mapping in heavily vegetated terrane. *International journal of remote sensing*, 23(22), 4827-4852.  
2277 <https://doi.org/10.1080/01431160110115014>
- 2278
- 2279
- 2280 Chiodini, G., Cioni, R., & Marini, L. (1993). Reactions governing the chemistry of crater fumaroles from Vulcano Island,  
2281 Italy, and implications for volcanic surveillance. *Applied Geochemistry*, 8(4), 357-371. [https://doi.org/10.1016/0883-](https://doi.org/10.1016/0883-2927(93)90004-Z)  
2282 [2927\(93\)90004-Z](https://doi.org/10.1016/0883-2927(93)90004-Z)
- 2283
- 2284 [Chiodini G., Cioni R., Marini L. and Panichi C. \(1995\) Origin of fumarolic fluids of Vulcano Island, Italy and implications for](https://doi.org/10.1016/0883-2927(93)90004-Z)  
2285 [volcanic surveillance. Bull. Volcanol. 57, 99–110. http://dx.doi.org/10.1007/BF00301400](https://doi.org/10.1016/0883-2927(93)90004-Z)
- 2286
- 2287 Chiodini, G., Allard, P., Caliro, S., Parello, F., 2000. 18O exchange between steam and carbon dioxide in volcanic and  
2288 hydrothermal gases: Implications for the source of water. *Geochim. Cosmochim. Acta* 64, 2479–2488  
2289 [https://doi.org/10.1016/S0016-7037\(99\)00445-7](https://doi.org/10.1016/S0016-7037(99)00445-7)
- 2290
- 2291 Chiodini, G., Frondini, F., & Raco, B. (1996). Diffuse emission of CO<sub>2</sub> from the Fossa crater, Vulcano Island (Italy). *Bulletin*  
2292 *of Volcanology*, 58, 41-50.  
2293 <https://doi.org/10.1007/s004450050124>
- 2294
- 2295 Chiodini, G., Granieri, D., Avino, R., Caliro, S., Costa, A., & Werner, C. (2005). Carbon dioxide diffuse degassing and  
2296 estimation of heat release from volcanic and hydrothermal systems. *Journal of Geophysical Research: Solid Earth*, 110(B8).  
2297 <https://doi.org/10.1029/2004JB003542>
- 2298
- 2299 Clarke, A. B., Ongaro, T. E., & Belousov, A. (2015). Vulcanian eruptions. In *The encyclopedia of volcanoes* (pp. 505-518).  
2300 Academic Press. <https://doi.org/10.1016/B978-0-12-385938-9.00028-6>
- 2301
- 2302 Coppola, D., Laiolo, M., Campus, A., & Massimetti, F. (2022). Thermal unrest of a fumarolic field tracked using VIIRS  
2303 imaging bands: The case of La fossa crater (Vulcano Island, Italy). *Frontiers in Earth Science*, 10, 964372.  
2304 <https://doi.org/10.3389/feart.2022.964372>
- 2305
- 2306 Cultrera F., Barreca G., Ferranti L., Monaco C., Pepe F., Passaro S., Barberi G., Bruno V., Burrato P., Mattia M., Musumeci  
2307 C., Scarfì L.; Structural architecture and active deformation pattern in the northern sector of the Aeolian-Tindari-Letojanni  
2308 fault system (SE Tyrrhenian Sea-NE Sicily) from integrated analysis of field, marine geophysical, seismological and geodetic  
2309 data. *Italian Journal of Geosciences* 2017;; 136 (3): 399–417. <https://doi.org/10.3301/IJG.2016.17>
- 2310
- 2311 Darmawan, H., Troll, V. R., Walter, T. R., Deegan, F. M., Geiger, H., Heap, M. J., ... & Müller, D. (2022). Hidden mechanical  
2312 weaknesses within lava domes provided by buried high-porosity hydrothermal alteration zones. *Scientific Reports*, 12(1), 3202.  
2313 <https://doi.org/10.1038/s41598-022-06765-9>
- 2314

- 2355 De Astis, G., La Volpe, L., Peccerillo, A., & Civetta, L. (1997). Volcanological and petrological evolution of Vulcano island  
2356 (Aeolian Arc, southern Tyrrhenian Sea). *Journal of Geophysical Research: Solid Earth*, 102(B4), 8021-8050.  
2357 <https://doi.org/10.1029/96JB03735>
- 2358
- 2359 De Astis, G., Lucchi, F., Dellino, P., La Volpe, L., Tranne, C. A., Frezzotti, M. L., & Peccerillo, A. (2013). Chapter 11 Geology,  
2360 volcanic history and petrology of Vulcano (central Aeolian archipelago). *Geological Society, London, Memoirs*, 37(1), 281-  
2361 349. <https://doi.org/10.1144/M37.11>
- 2362
- 2363 Di Tommaso, I., & Rubinstein, N. (2007). Hydrothermal alteration mapping using ASTER data in the Infiernillo porphyry  
2364 deposit, Argentina. *Ore Geology Reviews*, 32(1-2), 275-290. <https://doi.org/10.1016/j.oregeorev.2006.05.004>
- 2365
- 2366 Diliberto, I. S. (2013). Time series analysis of high temperature fumaroles monitored on the island of Vulcano (Aeolian  
2367 Archipelago, Italy). *Journal of volcanology and geothermal research*, 264, 150-163.  
2368 <https://doi.org/10.1016/j.jvolgeores.2013.08.003>
- 2369
- 2370 Diliberto, I. S. (2017). Long-term monitoring on a closed-conduit volcano: A 25 year long time-series of temperatures recorded  
2371 at La Fossa cone (Vulcano Island, Italy), ranging from 250 C to 520 C. *Journal of Volcanology and Geothermal Research*,  
2372 346, 151-160.  
2373 <https://doi.org/10.1016/j.jvolgeores.2017.03.005>
- 2374
- 2375 Diliberto, I., Pedone, M., Jácome Paz, M., Inguaggiato, S., Mazot, A., Cangemi, M. and Pisciotta, A.F., 2021. Volcanic Gas  
2376 Hazard Assessment in the Baia di Levante Area (Vulcano Island, Italy) Inferred by Geochemical Investigation of Passive Fluid  
2377 Degassing. *Environmental Geosciences*, 11.  
2378 <https://doi.org/10.3390/geosciences11110478>
- 2379
- 2380 Donoghue, E., Troll, V. R., Harris, C., O'Halloran, A., Walter, T. R., & Torrado, F. J. P. (2008). Low-temperature hydrothermal  
2381 alteration of intra-caldera tuffs, Miocene Tejada caldera, Gran Canaria, Canary Islands. *Journal of Volcanology and  
2382 Geothermal Research*, 176(4), 551-564. <https://doi.org/10.1016/j.jvolgeores.2008.05.002>
- 2383
- 2384 Donoghue, E., Troll, V. R., & Harris, C. (2010). Fluid–rock interaction in the Miocene, Post-Caldera, Tejada intrusive  
2385 complex, Gran Canaria (Canary Islands): insights from mineralogy, and O-and H-isotope geochemistry. *Journal of Petrology*,  
2386 51(10), 2149-2176. <https://doi.org/10.1093/petrology/egq052>
- 2387
- 2388 Fauvel, M., Chanussot, J., & Benediktsson, J. A. (2009). Kernel principal component analysis for the classification of  
2389 hyperspectral remote sensing data over urban areas. *EURASIP Journal on Advances in Signal Processing*, 2009, 1-14.
- 2390
- 2391 Fischer, T. P., Ramírez, C., Mora-Amador, R. A., Hilton, D. R., Barnes, J. D., Sharp, Z. D., ... & Shaw, A. M. (2015). Temporal  
2392 variations in fumarole gas chemistry at Poás volcano, Costa Rica. *Journal of Volcanology and Geothermal Research*, 294, 56-  
2393 70. <https://doi.org/10.1016/j.jvolgeores.2015.02.002>
- 2394

- 2433 [Frolova, et al., \*Effects of hydrothermal alterations on physical and mechanical properties of rocks in the Kuril–Kamchatka\*](#)  
2434 [island arc. \*Engineering Geology\*, 2014, 183. Jg., S. 80-95.](#)  
2435 <https://doi.org/10.1016/j.enggeo.2014.10.011>
- 2436
- 2437 Fulignati, P., Gioncada, A., & Sbrana, A. (1998). Geologic model of the magmatic-hydrothermal system of vulcano (Aeolian  
2438 Islands, Italy). *Mineralogy and Petrology*, 62(3-4), 195.
- 2439
- 2440 Fulignati, P., Gioncada, A., & Sbrana, A. (1999). Rare-earth element (REE) behaviour in the alteration facies of the active  
2441 magmatic–hydrothermal system of Vulcano (Aeolian Islands, Italy). *Journal of Volcanology and geothermal research*, 88(4),  
2442 325-342.  
2443 [https://doi.org/10.1016/S0377-0273\(98\)00117-6](https://doi.org/10.1016/S0377-0273(98)00117-6)
- 2444
- 2445 Fulignati, P. (2020). Clay minerals in hydrothermal systems. *Minerals*, 10(10), 919. <https://doi.org/10.3390/min10100919>  
2446 <https://doi.org/10.3390/min10100919>
- 2447 Gertisser, R., Troll, V. R., Walter, T. R., Nandaka, I. G. M. A., & Ratdomopurbo, A. (Eds.). (2023). *Merapi Volcano: Geology,*  
2448 *Eruptive Activity, and Monitoring of a High-Risk Volcano.* Springer Nature.  
2449 <https://doi.org/10.1007/978-3-031-15040-1>
- 2450
- 2451 Giggenbach, W.F. (1996). Chemical Composition of Volcanic Gases. In: *Monitoring and Mitigation of Volcano Hazards.*  
2452 Springer, Berlin, Heidelberg.  
2453 [https://doi.org/10.1007/978-3-642-80087-0\\_7](https://doi.org/10.1007/978-3-642-80087-0_7)
- 2454
- 2455 Halldórsson, S. A., Hilton, D. R., Troll, V. R., & Fischer, T. P. (2013). Resolving volatile sources along the western Sunda  
2456 arc, Indonesia. *Chemical Geology*, 339, 263-282.  
2457 <https://doi.org/10.1016/j.chemgeo.2012.09.042>
- 2458
- 2459 Harris, A. J., Lodato, L., Dehn, J., & Spampinato, L. (2009). Thermal characterization of the Vulcano fumarole field. *Bulletin*  
2460 *of Volcanology*, 71, 441-458.  
2461 <https://doi.org/10.1007/s00445-008-0236-8>
- 2462
- 2463 Harris, A., Alparone, S., Bonforte, A., Dehn, J., Gambino, S., Lodato, L., & Spampinato, L. (2012). Vent temperature trends  
2464 at the Vulcano Fossa fumarole field: the role of permeability. *Bulletin of volcanology*, 74, 1293-1311.  
2465 <https://doi.org/10.1007/s00445-012-0593-1>
- 2466
- 2467 Heap, M.J., Troll, V.R., Kushnir, A.R.L., Gilg, H.A., Collinson, A.S.D., Deegan, F.M., Darmawan, H., Seraphine, N., Neuberger,  
2468 J. and Walter, T.R., 2019. Hydrothermal alteration of andesitic lava domes can lead to explosive volcanic behaviour. *Nature*  
2469 *Communications*, 10(1): 5063. <https://doi.org/10.1038/s41467-019-13102-8>
- 2470

- 2513 Heap, M. J., & Violay, M. E. (2021). The mechanical behaviour and failure modes of volcanic rocks: a review. *Bulletin of*  
2514 *Volcanology*, 83(5), 33.  
2515 <https://doi.org/10.1007/s00445-021-01447-2>
- 2517 [Heap, M. J., Baumann, T. S., Rosas-Carbajal, M., Komorowski, J. C., Gilg, H. A., Villeneuve, M., ... & Reuschlé, T. \(2021\).  
2518 \*Alteration-Induced Volcano Instability at La Soufrière de Guadeloupe \(Eastern Caribbean\). Journal of Geophysical Research:  
2519 Solid Earth\*, 126\(8\), e2021JB022514. <https://doi.org/10.1029/2021JB022514>](#)
- 2521 [Heap, M. J., Baumann, T., Gilg, H. A., Kolzenburg, S., Ryan, A. G., Villeneuve, M., ... & Clyne, M. A. \(2021\). Hydrothermal  
2522 alteration can result in pore pressurization and volcano instability. \*Geology\*, 49\(11\), 1348-1352.  
2523 <https://doi.org/10.1130/G49063.1>](#)
- 2525 Henley, R. W., & McNabb, A. (1978). Magmatic vapor plumes and ground-water interaction in porphyry copper emplacement.  
2526 *Economic Geology*, 73(1), 1-20. <https://doi.org/10.2113/gsecongeo.73.1.1>
- 2528 Inguaggiato, S., Vita, F., Diliberto, I. S., Inguaggiato, C., Mazot, A., Cangemi, M., & Corrao, M. (2022). The volcanic activity  
2529 changes occurred in the 2021–2022 at Vulcano island (Italy), inferred by the abrupt variations of soil CO<sub>2</sub> output. *Scientific*  
2530 *Reports*, 12(1), 21166. <https://doi.org/10.3390/rs14051283>
- 2531 ~~Julia, F., Vladimir, L., Sergey, R., & David, Z. (2014). *Effects of hydrothermal alterations on physical and mechanical*  
2532 *properties of rocks in the Kuril Kamchatka island arc. Engineering Geology*, 183, 80-95.  
2533 <https://doi.org/10.1016/j.enggeo.2014.10.011>~~
- 2535 Kassambara, A. (2020). ggpubr: 'ggplot2' based publication ready plots. R package version 0.4. 0.
- 2537 Kereszturi, G., Schaefer, L. N., Miller, C., & Mead, S. (2020). Hydrothermal alteration on composite volcanoes: mineralogy,  
2538 hyperspectral imaging, and aeromagnetic study of Mt Ruapehu, New Zealand. *Geochemistry, Geophysics, Geosystems*, 21(9),  
2539 e2020GC009270. <https://doi.org/10.1029/2020GC009270>  
2540 ~~<https://doi.org/10.1029/2020GC009270>~~
- 2541 Liuzzo, M., Di Muro, A., Giudice, G., Michon, L., Ferrazzini, V., & Gurrieri, S. (2015). New evidence of CO<sub>2</sub> soil degassing  
2542 anomalies on P iton de la F ournaise volcano and the link with volcano tectonic structures. *Geochemistry, Geophysics,  
2543 Geosystems*, 16(12), 4388-4404. <https://doi.org/10.1002/2015GC006032>
- 2545 [Loughlin, W. P. \(1991\). \*Principal component analysis for alteration mapping. Photogrammetric Engineering and Remote  
2546 Sensing\*, 57\(9\), 1163-1169.](#)
- 2548 Lynch, D.K., Hudnut, K.W. and Adams, P.M., 2013. Development and growth of recently-exposed fumarole fields near Mullet  
2549 Island, Imperial County, California. *Geomorphology*, 195: 27-44. <https://doi.org/10.1016/j.geomorph.2013.04.022>
- 2551 Madonia, P., Cusano, P., Diliberto, I. S., & Cangemi, M. (2013). Thermal anomalies in fumaroles at Vulcano island (Italy)  
2552 and their relationship with seismic activity. *Physics and Chemistry of the Earth, Parts A/B/C*, 63, 160-169.  
2553 <https://doi.org/10.1016/j.pce.2013.06.001>

- 2595 Madonia, P., Cangemi, M., Costa, M., & Madonia, I. (2016). Mapping fumarolic fields in volcanic areas: A methodological  
2596 approach based on the case study of La Fossa cone, Vulcano island (Italy). *Journal of volcanology and geothermal research*,  
2597 324, 1-7.  
2598 <https://doi.org/10.1016/j.jvolgeores.2016.05.014>
- 2600 Mannini, S., Harris, A. J., Jessop, D. E., Chevrel, M. O., & Ramsey, M. S. (2019). Combining ground-and ASTER-based  
2601 thermal Measurements to Constrain fumarole field heat budgets: The case of Vulcano Fossa 2000–2019. *Geophysical Research*  
2602 *Letters*, 46(21), 11868-11877. <https://doi.org/10.1029/2019GL084013>  
2603 <https://doi.org/10.1029/2019GL084013>
- 2604 Mia, B., & Fujimitsu, Y. (2012). Mapping hydrothermal altered mineral deposits using Landsat 7 ETM+ image in and around  
2605 Kuju volcano, Kyushu, Japan. *Journal of Earth System Science*, 121, 1049-1057. <https://doi.org/10.1007/s12040-012-0211-9>
- 2606  
2607 Middlemost, E. A. (1994). Naming materials in the magma/igneous rock system. *Earth-science reviews*, 37(3-4), 215-224.  
2608 [https://doi.org/10.1016/0012-8252\(94\)90029-9](https://doi.org/10.1016/0012-8252(94)90029-9)
- 2609  
2610 Minissale, A., Donato, A., Procesi, M., Pizzino, L. and Giammanco, S., 2019. Systematic review of geochemical data from  
2611 thermal springs, gas vents and fumaroles of Southern Italy for geothermal favourability mapping. *Earth-Sci Rev*, 188: 514-  
2612 535. <https://doi.org/10.1016/j.earscirev.2018.09.008>
- 2613  
2614 Müller, D., Bredemeyer, S., Zorn, E., De Paolo, E., & Walter, T. R. (2021). Surveying fumarole sites and hydrothermal  
2615 alteration by unoccupied aircraft systems (UAS) at the La Fossa cone, Vulcano Island (Italy). *Journal of Volcanology and*  
2616 *Geothermal Research*, 413, 107208.  
2617 <https://doi.org/10.1016/j.jvolgeores.2021.107208>
- 2618  
2619 Nuccio, P. M., & Paonita, A. (2001). Magmatic degassing of multicomponent vapors and assessment of magma depth:  
2620 application to Vulcano Island (Italy). *Earth and Planetary Science Letters*, 193(3-4), 467-481. [https://doi.org/10.1016/S0012-821X\(01\)00512-X](https://doi.org/10.1016/S0012-821X(01)00512-X)
- 2621  
2622  
2623 Paonita, A., Federico, C., Bonfanti, P., Capasso, G., Inguaggiato, S., Italiano, F., ... & Sortino, F. (2013). The episodic and  
2624 abrupt geochemical changes at La Fossa fumaroles (Vulcano Island, Italy) and related constraints on the dynamics, structure,  
2625 and compositions of the magmatic system. *Geochimica et ~~cosmochimica acta~~ Cosmochimica Acta*, 120, 158-178.  
2626 <https://doi.org/10.1016/j.gca.2013.06.015>
- 2627  
2628 [Pearson, K. F.R.S. \(1901\). LIII. On lines and planes of closest fit to systems of points in space. The London, Edinburgh, and](https://doi.org/10.1016/j.gca.2013.06.015)  
2629 [Dublin Philosophical Magazine and Journal of Science](https://doi.org/10.1080/14786440109462720), 2(11), 559–572. <https://doi.org/10.1080/14786440109462720>
- 2630  
2631 Pirajno, F. (2009). Hydrothermal Processes and Wall Rock Alteration. In: *Hydrothermal Processes and Mineral Systems*.  
2632 Springer, Dordrecht.  
2633 [https://doi.org/10.1007/978-1-4020-8613-7\\_2](https://doi.org/10.1007/978-1-4020-8613-7_2)
- 2634

2668 Reid, M. E., Sisson, T. W., & Brien, D. L. (2001). Volcano collapse promoted by hydrothermal alteration and edifice shape,  
 2669 Mount Rainier, Washington. *Geology*, 29(9), 779-782.  
 2670 [https://doi.org/10.1130/0091-](https://doi.org/10.1130/0091-7613(2001)029%3C0779:VCPBHA%3E2.0.CO;2)  
 2671 [7613\(2001\)029%3C0779:VCPBHA%3E2.0.CO;2](https://doi.org/10.1130/0091-7613(2001)029%3C0779:VCPBHA%3E2.0.CO;2)  
 2672  
 2673 Rowan, L. C., Wetlaufer, P. H., & Stewart, J. H. (1976). Discrimination of rock Types and detection of hydrothermally altered  
 2674 areas in south-central Nevada by the use of computer-enhanced ERTS images.  
 2675  
 2676 [Silvestri, M., Rabuffi, F., Pisciotta, A., Musacchio, M., Diliberto, I. S., Spinetti, C., ... & Buongiorno, M. F. \(2019\). Analysis](#)  
 2677 [of thermal anomalies in volcanic areas using multiscale and multitemporal monitoring: Vulcano island test case. Remote](#)  
 2678 [Sensing, 11\(2\), 134. https://doi.org/10.3390/rs11020134](#)  
 2679  
 2680 Stevenson, J.A. and Varley, N., 2008. Fumarole monitoring with a handheld infrared camera: Volcán de Colima, Mexico,  
 2681 2006–2007. *Journal of Volcanology and Geothermal Research*, 177(4), pp.911-924.  
 2682 <https://doi.org/10.1016/j.jvolgeores.2008.07.003>  
 2683  
 2684 Tayebi, M.H., Tangestani, M.H. & Vincent, R.K. Sub-pixel mapping of iron-bearing minerals using ALI data and MTMF  
 2685 algorithm, Masahim volcano, SE Iran. *Arab J Geosci* 8, 3799–3810 (2015). <https://doi.org/10.1007/s12517-014-1400-4>  
 2686  
 2687 Troll, V. R., Hilton, D. R., Jolis, E. M., Chadwick, J. P., Blythe, L. S., Deegan, F. M., ... & Zimmer, M. (2012). Crustal CO2  
 2688 liberation during the 2006 eruption and earthquake events at Merapi volcano, Indonesia. *Geophysical Research Letters*,  
 2689 39(11).  
 2690 <https://doi.org/10.1029/2012GL051307>  
 2691  
 2692 Toutain, J.-P., Sortino, F., Baubron, J.-C., Richon, P., Surono, Sumarti, S. and Nonell, A., 2009. Structure and CO2 budget of  
 2693 Merapi volcano during inter-eruptive periods. *B Volcanol*, 71(7): 815-826. <https://doi.org/10.1007/s00445-009-0266-x>  
 2694  
 2695 Van der Meer, F. D., Van der Werff, H. M., Van Ruitenbeek, F. J., Hecker, C. A., Bakker, W. H., Noomen, M. F., ... & Woldai,  
 2696 T. (2012). Multi- and hyperspectral geologic remote sensing: A review. *International Journal of Applied Earth Observation and*  
 2697 *Geoinformation*, 14(1), 112-128. <https://doi.org/10.1016/j.jag.2011.08.002>  
 2698  
 2699  
 2700